Investigation of variation in oil sand properties via analysis of seismic and on-board truck data

by

Marjan Kakan

A thesis submitted in partial fulfillment of the requirements for the degree of

Master of Science

in

Mining Engineering

Department of Civil and Environmental Engineering
University of Alberta

Abstract

The ever increasing size of mining equipment has caused many instability concerns both on board and in the ground underneath. This highlights the need for more in-depth knowledge of variation in the properties of the ground as it has direct influence on the durability and life span of mining equipment. Since laboratory scale tests on the ground material samples provide limited information, gaining field information from on-site underfoot material provides greater detail. The purpose of this research is to analyse the results obtained from two sets of on-site measurements to predict the variation of ground stiffness as a haul truck travels over it. The first data set are the results of seismic measurements using an array of 72 geophones placed along a mining haul road. As the truck travels along this array, the geophones collect the signals due to the motion of truck. Upon application of appropriate frequency filters to remove noise signals from the original seismic data, the shear modulus and load stiffness of the oil sand close to each geophone can be determined via surface wave methods.

The second set of data was obtained from the on-board truck system also known as VIMS (Vital Information Management System). Of the numerous parameters in a VIMS data, we used strut pressures and truck speed in our analysis. Before performing any comparison between VIMS and seismic, the drift in the time frame the two data sets was calculated and corrected. The output signal of a geophone can be considered a direct measurement of a particle velocity. These values were used to obtain the deformation of the ground by integrating the area underneath the seismic peak. The analysis of VIMS data resulted in a stiffness value in the range of 2-10 MN/m. The seismic analysis resulted in a stiffness range of 5-70 MN/m. The two methods also predicted similar shape trends in variation of ground stiffness along the geophone arrays. The predicted stiffness values are relatively in agreement with the reported values of 10 MN/m for a softened oil sand.

Dedication

This work is dedicated to my mother, father and brother and my husband, Beniamin.

Acknowledgment

Foremost, I would like to express my sincere gratitude to my advisor Dr. Tim Joseph for the continuous support of my M.Sc. study and research, his patience, motivation, enthusiasm, and immense knowledge. His guidance helped me during the time of research and writing of this thesis. I could not have imagined having a better advisor and mentor for my M.Sc. study.

I would also like to express my thanks to Dr. Deng with whom I spent hours on discussion research advice that helped me through my M.Sc. thesis. I am grateful to Dr. Schmidt for his advice and time to answer my questions. I would also like to thank Dr. Sacchi's research group in the geophysics department for providing useful information regarding my research project. My special thanks to Mr. Kazemi Nojadeh from Dr. Sacchi's group for the instructive discussions, useful information and coding advice he provided.

I thank my fellow group mates in Dr. Joseph research team: Niousha, Magreth, Enjia, Sujith, Lin, Enzu, and Chaoshi, for the stimulating discussions, for the sleepless nights we were working together before deadlines, and for all the fun we have had in the last two years. I also thank to all my other friends for their unequivocal supports.

I would like to thank my mother, my father and my brother for their endless and understanding love through all years of my studies.

At the end and most importantly, I would like to express my special thanks to my beloved husband, Beniamin. Words cannot express how grateful I am to him for his patience, love, continuous encouragement and support throughout my studies.

Table of Content

List of Figures

List of Tables

Chapter 1

1. Introduction

The main goal of most mining operations is to achieve increased production. Such a goal has resulted in a trend of designing and manufacturing larger equipment. The advent of very large haul trucks known as ultra-class haul trucks is also a direct result of this transition. An important aspect of moving towards larger equipment is the effect of unplanned failure and unscheduled maintenance of these giant machines on total production. The high magnitude of loads carried by these vehicles along with their own weight increases the probability of unplanned and premature failures. These failures can occur to different parts of equipment. In an ultra-class haul truck, for instance, tires, rims, the suspension systems, and the frame are parts that experience high level of cycles loads and hence, the failure. The failure rate further increases when the ground conditions are not stable. This can occur due to softening of the ground (oil sands for instance) caused by weather and the cyclic nature of loads exerted on ground by equipment. These ground stability issues have direct influence on the instability of equipment parts. Hence, it is necessary to develop in-depth understanding of equipment-ground interactions to enhance the control over the above-mentioned issues.

The issues regarding the stability of large mining equipment can be categorized into two main groups related to ground stability and equipment stability. Since these two groups are closely related to each other, it is inevitable to that study of one necessitates considering the effects of the other. Studies of ground stability are focused on the properties and behavior of ground material under various conditions. Such studies can be done through conventional laboratory testing (such as tri-axial compression test) and by performing innovative and modified on-site tests and comparison of the results. Moreover, the interaction between the ground and equipment during mining operations transfers all the ground instabilities to the equipment. Hence, it is necessary to investigate the influence of the variation of the ground properties on the equipment.

Trucks can be considered as one of the most abused pieces of equipment in the mining industry [1]. Most of the time, operators drive these vehicles as fast as they can in harsh conditions to increase productivity. The cost for operating a typical fleet of haul trucks can account for 30 to 55% of the total expenses of an open-pit mine [2]. This highlights the

importance of better maintenance strategies and finding the root cause of truck failures. Around 20-25% of hauling costs correspond to expenses related to tires [3]. Tires are the link between the vehicle and ground. Considering the limited number of manufacturers and low inventory of haul truck tires, the design and maintenance of tires plays a key role [4]. Rims are other parts which require further development and design as haulers are faced to high impact loads due to unstable road conditions and increased payload capacity [5, 6]. As the heaviest single component of a haul truck, the truck frame also suffers from significant fatigue and cracking failures which are caused by the twist or racking motion in the frame of the vehicle [7, 8]. A component which plays an important role in controlling cyclic impacts and fatigue failure of the frame is the suspension system. Modifying the current structure of suspension systems in haul trucks is a possible solution [9]. Poor suspension systems also introduce vibrations which can cause safety issues impacting operators' back problems [10] .

The most important step towards investigation of the influence of ground condition on equipment parts is to evaluate the properties of the ground as the vehicle travels above it. The variation of ground properties due to motion of a vehicle can be a key indicator to prevent most of damages to different parts. While performing laboratory scale tests such as tri-axial compression to predict the behavior of the ground is beneficial, to examine the on-site ground properties using available data collection systems on a vehicle could also provide useful information about ground behavior. The main focus of this thesis is on evaluating the data acquired by the truck to predict the variation of the ground. These are done by combining the results of two on-site sets of data collected by two different instruments (vital information management system (VIMS) and seismic) and correlate their outcomes to predict the ground behavior. In the following sections, a background knowledge on the characteristics of oil sand as a ground material in our study is provided. Also, some background information about the interaction of oil sand and haul trucks reported in the literature will be presented. In the last section of this chapter, a brief introduction of the concept of seismic analysis is provided. Seismic analysis comprises a major portion of this thesis as it provides in-depth information about the behavior of the ground.

1.1. Oil sand properties

As mentioned previously, the stability of any type of mining equipment depends significantly on the stability of the underfoot ground. It is very difficult to analyse the stability aspects of equipment without considering the material underneath. The Northern part of Alberta contains the largest oil sand deposit reserve in the world. Besides heavy oil, another type of crude oil is bitumen. Bitumen is the primary hydrocarbon component of oil sands. About 20% of Alberta's oil sands bitumen reserves are close to the surface making extraction through surface mining feasible. Surface mining initially used draglines for surface excavation. However, truck and shovel operations started to replace draglines and long conveyor belts in the 1980's. Oil sand shows some unstable characteristics which is most likely due to its complex structure. As shown in Figure 1.1, it is a mixture of sand, water and crude bitumen. Therefore, dissimilarities in the behavior of oil sand are expected with any type of variation in the content of each component.

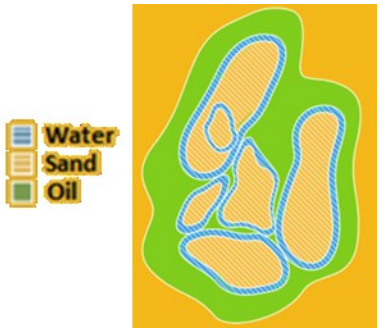

Figure 1.1. Schematic of the structure of oil sand [11] .

The bitumen content of Alberta's oil sand varies between 1 to 18%. Bitumen percentages above 12% are considered rich while anything above 6% is economically feasible to be mined. The mechanical behaviour of oil sand has been found to be dependent on the grade (bitumen, water and sand content), geologic deposition and temperature (influence on the viscosity of oil sand)[12] . It has also been found that the stability of equipment is directly affected by the stiffness of oil sand. The weather condition changes in Northern Alberta have direct influence on the stiffness of oil sand. The temperature variation from 30 to -30℃ causes the oil sand to behave similar to sandstone in winter and to weak soft clay in summer. This is illustrated in Figure 1.2. As can be seen in this graph, oil sand shows soft characteristics in summer.

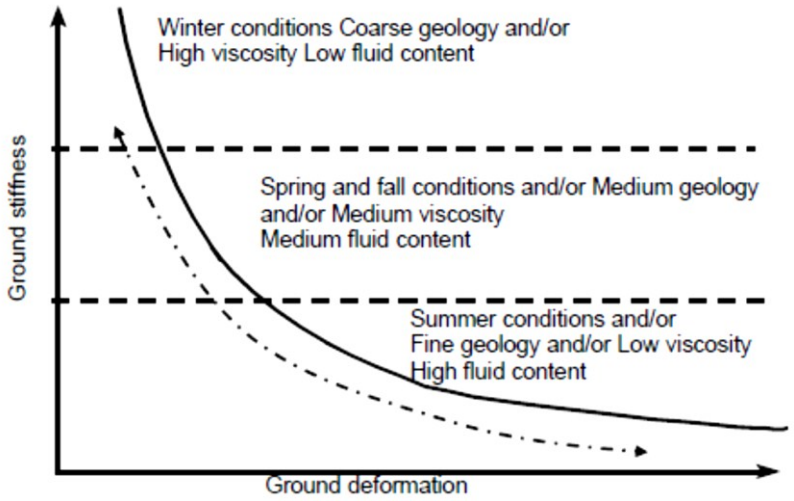

Figure 1.2. Oil sand stiffness at different seasons [13].

This causes very poor rolling resistance conditions which in turn, requires trucks to be loaded with less than their nominal payload. Furthermore, it has been shown that regardless of grade, geologic deposition and temperature, oil sand stiffness is a function of deformation. This is shown in Figure 1.3 which is plotted based on historical and measured strength-deformation data [12].

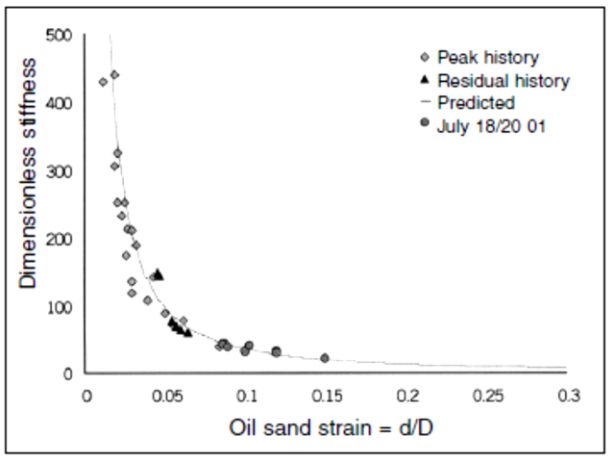

Figure 1.3. Oil sand stiffness-deformation relationship[12].

Another important behavior of oil sand is found when cyclic loads were applied. It has been shown that oil sand softens during cyclic loading and its modulus decreases with the number of cycles. This is illustrated in Figure 1.4.

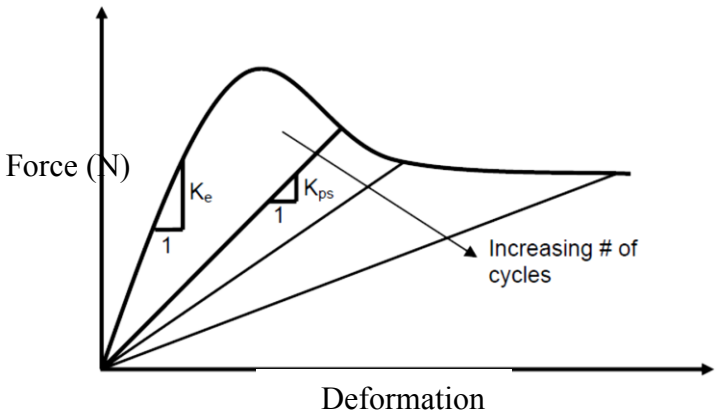

Figure 1.4. Oil sand stiffness-deformation relationship [14] .

Figure 1.4 mimics the actual mine field conditions where trucks travel along haul roads and produce cyclic loads on ground. On the other hand, during cold seasons the surface is very stiff while the sub-surface layers are still soft. Upon a few loading cycles, the oil sand in the sub-surface layer softens and causes undulations of the ground. In such conditions, while rolling resistance is not high the surface undulations can cause severe cyclic impacts on the structure of truck. Using this knowledge about the behavior of oil sand, finding a solution to reach a balance between these two extreme cases has been the purpose of many academic and industry researchers. In the following paragraphs, the results from some recent studies on the stability of oil sand are presented.

As mentioned, oil sand stiffness is a function of deformation. A typical surface mining operation consists of digging using shovels and moving the material with large trucks. Joseph[12] suggested an empirical relationship between oil sand stiffness and strain in the form of following equation:

$$\left(\frac{kD}{F}\right)\left(\frac{1-\nu}{\nu}\right)=C\left(\frac{d}{D}\right)^{-B} \quad (1)$$

Where k is the load stiffness of oil sand, F is the load exerted by equipment with the depth of influence D and v is the Poisson's ratio (0.29-0.33). Here d is the deformation and B and C are empirical constants for oil sand behavior. The depth of influence in this equation is dictated by the footprint area of equipment, A, and is independent of seasonal change. Based on the extended knowledge of geotechnical practices in oil sand mining industry, the depth of influence can be expressed as follows:

$$D = 3\sqrt{A} \quad (2)$$

The mechanical properties of oil sand are also of importance when performing investigations of oil sand stability. Due to its complex structure, oil sand properties are also affected by the method of sample preparation and testing. Triaxial tests of drained and undrained samples are mostly used for this purpose. Plewes[15] emphasized the fact that to mine field conditions where equipment loading occurs on the surface, undrained testing condition prevails. The bulk density of uniformly graded rich oil sand ranges from 2.05 to 2.18 Mg/m^3 with a porosity percentage of 28 to 36[15]. He also reported the modulus of deformation (E) at different confining pressures (σ_3) for drained oil sand which is shown in Figure 1.5.

The strength of Athabasca oil sand decreases with increasing temperature [16].

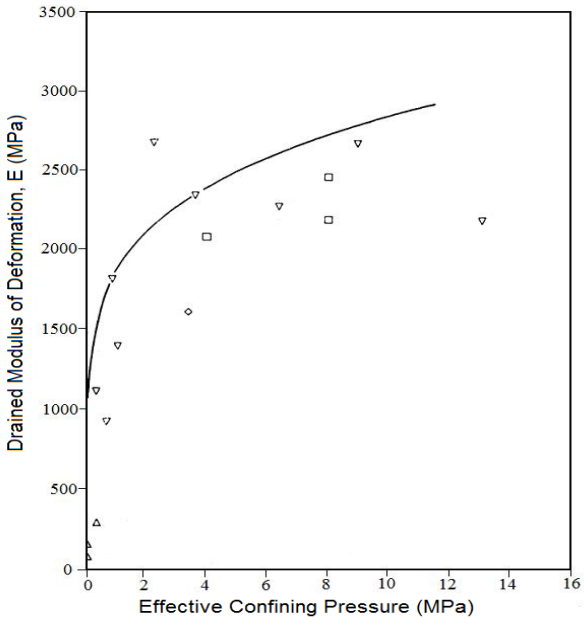

Figure 1.5. Modulus of deformation of oil sand for drained triaxial compression test[15]

As mentioned, the oil sand stiffness decreases during cyclic loading. The extent of such softening can be affected by parameters such as load level, rate of loading, number of cycles and temperature. In the case of a truck at a given frequency of ground cyclic loading, for a given load the ground performance depends not only on the speed of truck, but also on the number of trucks assigned. Sharif-Abadi [13] conducted research on oil sand samples of 8 and 11% bitumen content through conventional triaxial and plate loading tests under static and cyclic loading

conditions. Figure 1.6 shows the results of static triaxial tests on two samples at different confining pressures. As can be seen in Figure 1.6.(a), the peak strain for 8% bitumen content is fairly consistent at around 0.12-0.15, due to the low range of the confining pressures applied and a linear relationship between σ_1 and σ_3 can be established. The peak strain for samples with 11% bitumen is consistent at around 0.04-0.07. The peak strain for the 8% oil sand is around 2.5-3 times greater than that for the 11% oil sand, due to the finer grain of richer oil sand and a tendency towards a better arrangement of the particles during compaction. From these simple tests, it can be concluded that oil sand behaviour is highly variable depending on the grade and degree of disturbance.

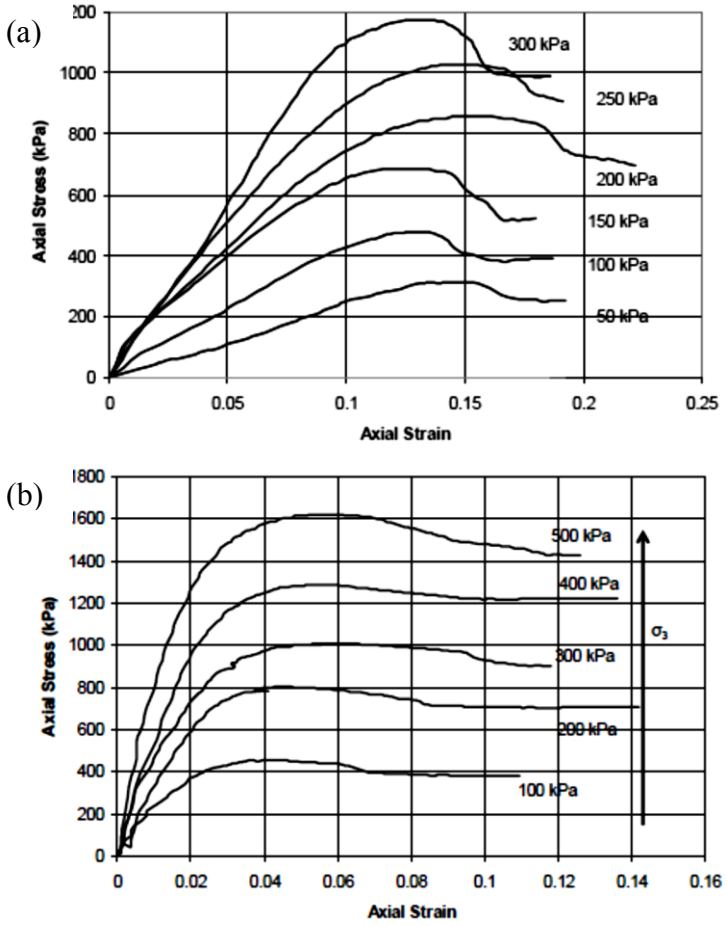

Figure 1.6. Stress-strain curve for samples with (a) 8% and (b) 11% bitumen under static loading [14].

Using a larger-scale laboratory method, Sharif-Abadi [17] conducted research on oil sand of 11% bitumen content and showed that after cyclic loading for several hundred cycles, the oil

sand pressure stiffness converges to a reduced value of 8kPa/mm. This value has been subsequently used for the prediction of ultimate oil sand deformation for different cycled load levels. Being a viscous material, oil sand deformation was not only found to be a function of time but also a function of load level and number of cycles.

From the results discussed above, it can be realized that a relatively comprehensive knowledge of oil sand behavior exists. From these known facts, methods and empirical equations, some prediction on the behavior of oil sand under dynamic conditions in a mine can be made. Furthermore, the results obtained from the on-site data collection tests can also be confirmed against literature reported values.

1.2. Haul truck-ground interactions

1.2.1. Tire-ground interactions

Comprehensive work has been done to study the interaction of tires with different types of ground materials. While most of this work has been done for highway and agricultural vehicles, it is still beneficial to review, since the principles of interaction are similar to some extent.

In a thorough study, Krick [18] investigated the behavior of tires on soft ground. On firm ground rolling resistance and slip can, for the most part, be neglected when under driving and braking forces, whereas for yielding ground they are of considerable importance. He investigated the force system on driven wheels, and used an improved six-component test frame used by previous workers, with all measurements were made in sandy loam in a soil bin. His main conclusions were that (a) lateral forces had an approximately linear relationship with slip angle up to 30° and (b) at a constant slip angle, lateral forces decreased as traction forces increased. From the experimental data, Krick developed relations between tractive and side forces as a function of side slip angle and wheel slip (an example plot is shown in Figure 1.7).

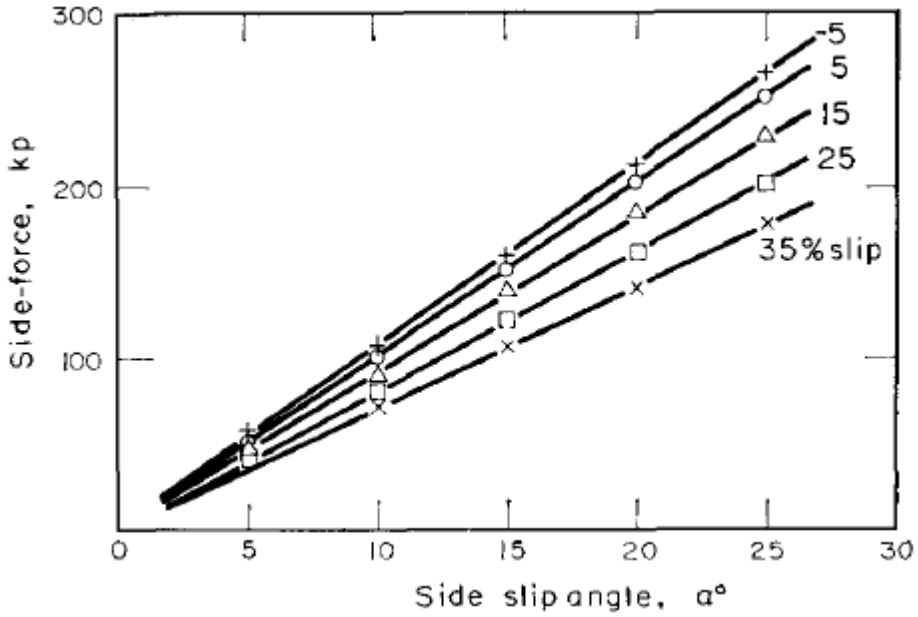

Figure 1.7. Relationship between side force and side slip angle at different slips [18].

However, his measurements were on fairly small tires with moderate tire loads. In other work, Wong [19] presented a different method for studying tire-ground interactions. He used a photographic method to investigate the soil flow underneath driven and towed tires, measuring the response of the terrain to the repetitive loading and the slip-sinkage characteristics of the terrain. He showed that soil does not flow in a manner akin to that beneath a plate, concluding that the soil flows in a composite manner, partly sideways and partly longitudinally. The proportions of each part dependant on the wheel width. So when the wheel is very wide, only longitudinal flow occurs. But even beneath a rather narrow wheel, soil exhibits longitudinal flow phenomena. Using his photography method he was able to show that the characteristics of the flow patterns and the trajectories of the particles show that the behaviour of soil beneath a moving wheel conforms to the basic principles of soil mechanics. The flow zones in sand are bounded by a logarithmic spiral and a straight line. In clay, they are bounded by sections of circles and a straight line. Wong [20, 21] reviewed the existing knowledge of soil-tire interactions and introduced important methods and models to better understanding these interactions.

As mentioned, there is an extensive knowledge in the literature on the performance of agricultural and military tires on different types of soil. However, extending this knowledge to

the large tires used on mining haul trucks requires further understanding and test work. Investigating the causes of tire failure on haul trucks has been an active research field in the past few years. The most common failures attributed to tires are: tread cuts, heat and mechanical separation, and sidewall cuts. Tread wear outs occur only when the tread of the tire is physically worn down due to the abrasive nature of the ground, something that is rarely seen in oil sand as other failure mechanisms predominate. Tread cuts occur when a truck runs over a sharp piece of material and it pierces through the tread material. A rolling tire generates heat as it rolls and flexes, so, heat and mechanical separations occur when heat is generated faster than it can be dissipated causing the tire temperature to reach a critical level where the rubber begins to separate from the steel belting. As the operating temperature of the tires increases they become more susceptible to failures from increased mechanical loading, impact and fatigue. Sidewall cuts occur when the sidewall of the tire folds onto the ground surface during high-g loading events and comes into contact with sharp material. This generally occurs when a truck turns a corner.

Due to the strong motivation to study and detect the operational damage to haul truck tires, several approaches have been developed to detect these faults before they occur. The general theme for such detection is to compare a set of features measured from the current situation to a reference set for a no-damage case. Thompson et al. [22] have investigated the behavior of tires by monitoring systems that rely on measured features such as suspension vibrations or strut pressure, which can also be used to characterize mine haul-road quality. Another approach is to track the temperature and pressure inside the tire using wireless sensors and identify the faults occurring during operation [23]. As a powerful method, modeling the tire and its interaction with ground and the suspension system can lead to a good understanding of tire behavior. Several methods of modeling tires on rough surfaces were summarized by Meige[24] . These are including: single-point contact model (parallel spring and damper), roller contact model (spring and damper with a single contact point), fixed footprint model (distributed springs and dampers at the contact area), radial spring model (springs distributed in circumference of the tire), and flexible ring model (thin ring connected to springs around the tire) and finite-element models. A schematic representing these methods is shown in Figure 1.8.

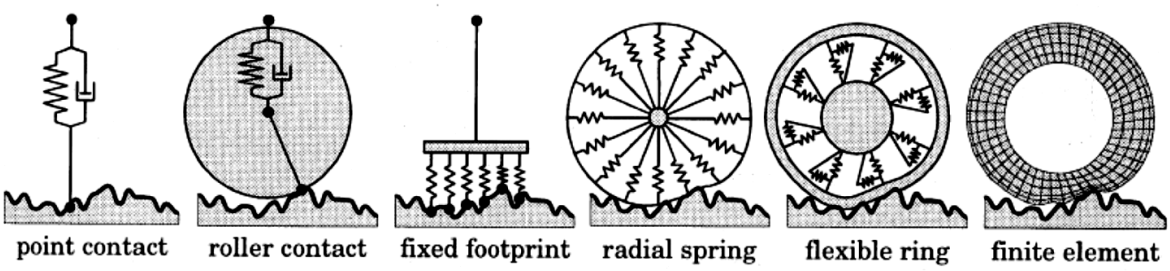

Figure 1.8. Different types of models for tire on rough roads[24].

In a recent study, Anzabi et al.[3] simulated the motion of tires using a simple dynamic model and showed that the differences between the motions of tires can be used as an indicator for monitoring the faults in a tire.

Digital image correlation (DIC) is a three-dimensional (3D) full-field optical technique that measures the deformation of an object using images of the surface provided by cameras which collect data during deformation. It is predicted that the strain exhibited at the tire surface will change as it undergoes wear, fatigue, separation and other forms of damage. The main idea of the method is based on tracking the motion of points in a small region when the object is undergoing mechanical or thermal stress. Studies show that DIC methods are ideal for tire surface strain measurement, as a non-contact technique, because it does not require any instrumentation on the tire itself [25]. Kotchan et al. [26] were able to use this method measure the deformation of tires in a laboratory scale test and calculate the tire strain under different loads and pressures. Vertical and horizontal cuts were made on the sidewall of a 18" tire and the images before and after these cuts were analysed using commercial software. Figure 1.9 shows the displacement difference on the tire side wall due to the presence of a horizontal cut. This method shows promising results that can be further extended to fault detection of on-site haul truck tires.

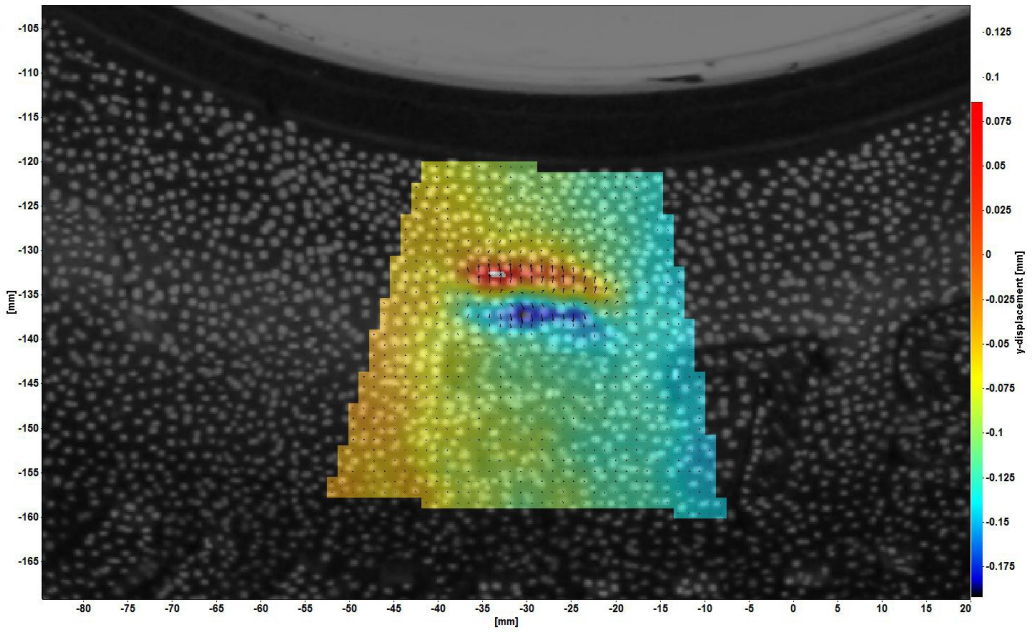

Figure 1.9. The vertical deformation caused by the presence of a horizontal cut in tire side wall [26].

Apart from fault detection, tire maintenance is another research field that aims to prevent tire failures through proper maintenance. This involves the application of engineering statistics to find the best maintenance technique. In a case study, Zhou et al. [27] investigated the effect of tire rotation practices including the rotation sequence and frequency on the life of tire. They established relationships between tire life, wear and the frequency of tire rotation and also suggested the optimum rotation sequence for a typical truck. In a similar study [28] , the effects of monitoring tire air pressure as an effective method for better maintaining haul truck tires has been reported. Their research on a typical mine truck brought the following conclusions: high tire installation air pressure does influence tire life and tire tread wear rate and rear inside and left front positions experienced the most air pressure spikes.

Another important factor in studies of tire-ground interactions is rolling resistance. Rolling resistance is the opposing force to rolling motion and prevents vehicle tires from moving. One of the main concerns in the mining industry is to reduce rolling resistance to an acceptable level suitable for heavy equipment where a considerable amount of energy can be saved with appropriate maintenance of roads. Selection of road materials with lower rolling resistance is a key solution. Numerous works have been dedicated to develop suitable definitions and

measurement techniques for rolling resistance of tires. For the sake of brevity, only few are presented in this report.

Komandi [29] evaluated the rolling resistance force by defining rolling resistance as a moment, but an active force is needed to move the wheel. Such a force acts at the axle of the towed wheel and at the perimeter of the driving wheel. He went on to describe the peripheral force based on the Coulomb's equation acting on running gear. Due to inadequacy of detailed analysis this was furthered via Janosi's equation which describes the peripheral force as a function of contact area, load, friction in the contact patch and the tangent modulus of shear stress [29]. Deriving from various observations, the equations were simplified to develop a model for the moments at the driving and driven wheel separately. These were based on the forces acting at the axle and on the peripheral forces on a wheel. Although these models were consistent with all previous models developed, they did not represent the influence of various factors that affect the rolling resistance of tires. From his observations, Komandi drew the following conclusion: mechanical characteristics of towed and driving wheels under static conditions are similar and analyses can be transferred from one case to the other; where the normal force due to deformation of tire or ground or both have horizontal and vertical components and moments exerted by these about the center of wheel are equal [29].

In an extensive study, Miege [24] employed a series of available models for tire-ground interaction to predict the rolling resistance of tires under dynamic vertical load. His basic assumption on defining the rolling resistance is shown in Figure 1.10.

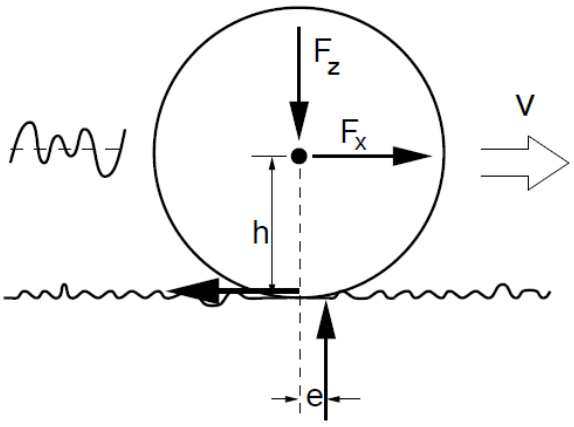

Figure 1.10. Tire rolling resistance model[24].

Balancing the moment based on the above model yield the following relationship:

$$\frac{F_x}{F_z} = \frac{e}{h} = Rolling\ Resistance \quad (3)$$

Where *h* is the loaded radius of the tire and the ratio *e/h* represents the rolling resistance. By comparing the experimental results and the predicted data form three different models he showed the validity of these models for dynamic vertical load frequencies up to 10 Hz. The limited amount of experimental data made it difficult to validate the rolling resistance for higher frequency loads.

Another approach of analysing rolling resistance was employed by Anand [30] . Using a simple and innovative laboratory scale setup, he was able to correlate the force required for pulling a scaled truck to the rolling resistance. The truck was built with dimensions proportionate to an ultra-class haul truck. This truck was designed to run on a test bed filled with different materials in the same manner as an ultra-class truck runs on a haul road. The bed also needed to be scaled appropriately. The change in the ramp angle represented a change in the rolling resistance in these tests. In order to establish a baseline relationship between the pulling force and ramp angle (RR), initial tests were performed on a rigid test bed. Figure 1.11 shows the relation between the pull force and the ramp angle [30].

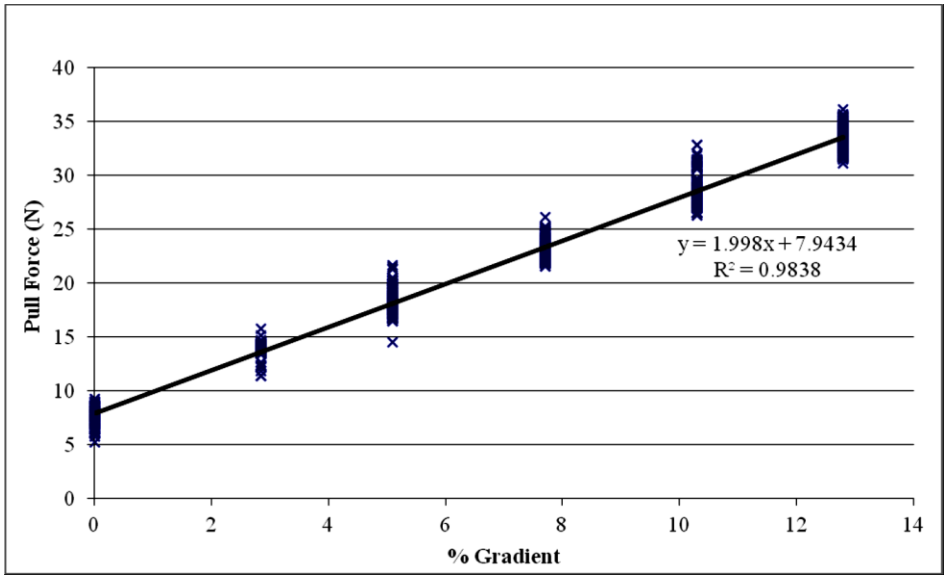

Figure 1.11. Pull force vs. % ramp on flat surface [30].

Further tests were also performed on oil sand capped by different materials including limestone, pit run and sand. The effect of capping the materials on rolling resistance of oil sand

ground over consecutive cycles was shown. When a thin layer of limestone is added on top of oil sand, the composite starts with a lower value of RR and shows an improved level of stability over extended cycling. His finding showed the important role of using capping materials in stabilizing the behaviour of oil sand [30].

From the review presented above, it can be realized that the knowledge of the interaction of tires and ground is quite well-understood. However, further design and simpler measurements techniques would be beneficial to allow for adding the existing knowledge to the mine fields. The following section reviews the influence of ground stability on suspension systems and frame of haul trucks.

1.2.2. Suspension systems and truck body considerations

Traditionally, suspension systems perform multiple tasks such as maintaining contact between vehicle tires and the road, addressing the stability of the vehicle, and isolating the frame of the vehicle from road-induced vibration and shocks. In general, ride comfort, road handling, and stability are the most important factors in evaluating suspension performance. Ride comfort is proportional to the absolute acceleration of the vehicle body, while road handling is linked to the relative displacement between vehicle body and the tires. However, stability of vehicles is related to the tire-ground contact. The main concern in suspension design and control is the fact that currently, achieving improvement in these three objectives poses a challenge because these objectives will likely conflict with each other in the vehicle operating domain.

According to Santos et al.[9] , the current status of most suspension systems in mining haul truck is based on a simple design used for haulers for 40 years. Such systems mainly rely on a fixed orifice which controls the dampening force. Santos suggested a modification of this system by varying the size of orifice and proposed a semi-active suspension. The main objective of this study was the observation of many “topping” up events where metal-metal contact occurs due to the excessive forces during a high g level event. Through application of thermodynamics and fluid dynamic considerations, Santos was able to model the effect of variable orifice on the damping force of suspension system. By comparing results with those from OEM shock absorbers, he showed that the modified shock absorber generates a greater damping force which prevents the topping up event.

Several studies have been done on the performance of suspension systems of haul trucks. It has been shown that the design of suspension systems has an important effect on several factors

including ride comfort, frame damage, suspension operation, energy consumption [9, 31] . The fundamental issues of current suspension systems were reviewed by Cole [31, 32] and the performance of these systems were analyzed through extensive modeling. Suspension design of road vehicles necessities a complex compromise among different performance measures related to ride and handling qualities. Moreover, control of suspension travel that influences both the ride and handling qualities of vehicles is another important design task. The minimization of suspension travel could also improve the productivity of heavy vehicles, considering regulations on heavy vehicle dimensions. Cole also provides a numerical investigation of the roll control of heavy vehicles using five different suspension configurations. The study involves an analysis of different passive and active suspensions, and it concludes that an increase in the stiffness of an anti-roll bar can improve the vehicle roll stability at the cost of ride comfort. Cole points out that optimal suspension tunings achieved under certain driving speeds may not work well for other speeds. This is particularly important in light of the fact that most road vehicles operate in a wide range of speeds, apart from road roughness conditions [32].

Another study was performed by Eslaminasab [33] on the design and development of a semi-active intelligent suspension system for haul truck. Several conclusions drawn from his works are as follows: the gas-spring suspension systems was successfully mathematically modeled and proven to be able to predict behavior. Utilizing a neural network was proposed to model and map the performance of semi-active damper, a new internal solenoid semi-active damper was designed and tested against two commercial dampers as benchmarks. Analysis of the response times for three different dampers were performed and a new semi-active strategy to control the suspension system was proposed.

As a truck travels along a soft ground haul road, it experiences many high g level loads as previously mentioned. This is due to the unstable nature of soft ground, oil sand for instance, under cyclic loading conditions. The ground undulation is a direct consequence of such instability. This causes the truck to experience cyclic loading as a reaction to ground underneath. Apart from tire and suspension systems, truck frames and bodies also suffer from the appearance of these loads. In order to realize the severity of such loads on the truck structure, Joseph [7] introduced the concept of rack motion which is defined as the difference of the sum of diagonally opposite strut pairs. Assuming L_F, R_F, L_R and R_R denoted left front, right front, left rear and right rear strut loads respectively, rack can written as:

$$Rack = [(L_F + R_R) - (R_F + L_R)] \quad (4)$$

From this equation, it can be realized that the proper determination of the load exerted on each strut is an important factor. Joseph [7] also suggested the use of a simpler and more intuitive descriptor for the amount of rack. Previous works have used the unit of pressure to express the amount of rack however, expressing the rack in the form of acceleration, i.e. the number of g (9.81 m/s^2) can be recognized be a broader range of people. By performing conventional Newtonian calculations, he was able to define the level of any dynamic load exerted on each strut in the following format:

$$F_{dynamic} = \sum_{i=1}^{4} M_i(g + a_i) \quad (5)$$

Where M_i is the mass applied on each strut and a_i is the dynamic contribution on each strut. Hence, the a_i can be used to define the rack, roll and pitch parameters:

$$Rack = 1/g[(a_1+a_4)-(a_2+a_3)] \quad (6)$$

$$Roll = 1/g[(a_1+a_2)-(a_3+a_4)] \quad (7)$$

$$Pitch = 1/g[(a_1+a_3)-(a_2+a_4)] \quad (8)$$

From the equation (6), Jopesh [7] was able to calculate the magnitude of rack force in terms of number of g's in a typical mining haul truck in a defined period. The results of his observation are shown in Figure 1.12.

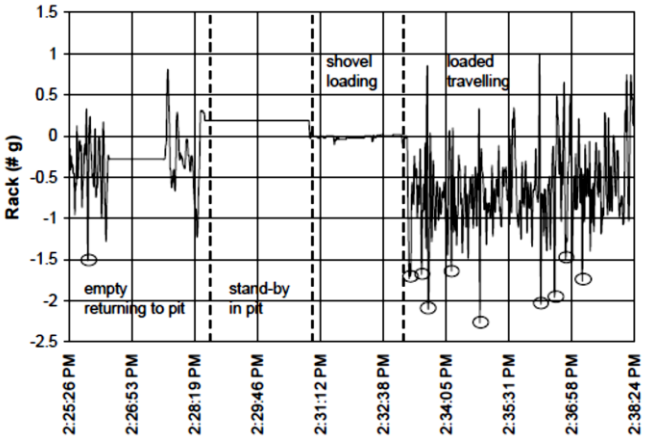

Figure 1.12. Rack experienced by truck in terms of number of g [7].

From the number of events where trucks experience g levels greater than 1.5, he estimated the life of frame based on cyclic fatigue theory. The analyses of data revealed that the effect of rack

is dominant when truck is loaded and in motion. By assuming the realistic number of 80% for utilization in 350 day operation year, the estimated life of a frame was seen as 6.2 years. This is significantly lower than the expected life time from the manufacturer point of view which is 10 years. Based on this example case study, it can be realized the influence of ground instability which in turn caused the advent of numerous high g level loadings on the structure of a truck can have tremendous damaging impacts on the truck frame [7].

In another study, Whalen et al. [8] employed finite element modeling to predict the standard effect of rack motion on the body of a truck. The appearance of cracking in the intersection of bolster-stringers was found to be the root cause of deflection in the frame. They proposed some alternative designs to improve this phenomenon which is a major issue for oil sand operations. Their suggestions included improving the welding of the joints at the intersections, changing the geometry of the floor stiffeners and replacing the bolster-stringer intersections with a cast component of similar geometry [8].

Another example of changing the design was proposed by Poh et al. [34]. They suggested the use of a curved steel membrane floor for the bodies of haul trucks and compared performance against the flat-plate type floor. Their comparison was based on the response of floors when struck by a standard impactor. Their optimal membrane design reduced the empty mass of a 172 ton truck by 8 ton. Apart from this, the membrane eliminated the use of additional wear plates and also reduced the fatigue problems associated with welded joints. Another advantage of such a membrane was the rapid replacement ability since it is only attached to the body by its edges. They also built a prototype of their best design and reported 20000 working hours without the need for replacement of this prototype [34].

1.3. Seismic analysis

The basic and principle component of seismic analysis is the seismic wave. The behavior of seismic waves in any material depends on the physical properties of that material. In other words, the generation, propagation, and attenuation of the wave will be governed by the physical characteristics of a material. Hence, understanding the basic principles behind the physical properties of materials helps better predict the seismic behavior in that material. Seismic waves can be considered as elastic waves as they only cause reversible deformation in the medium they are traveling through [35]. This means that as waves travel through the material, there are

simultaneous compression and tension motions in the particles along the wave pathway. Before explaining different types of seismic waves and their characteristics and applications, it is advantageous to provide a summary of elastic properties of solids.

1.3.1. Mechanical properties of solids

1.3.1.1. Strain

Strain is defined as the change in the dimension of a solid relative to its original dimensions and usually expressed as a percentage. Generally, two types of strain are considered for any material being normal or dilatational strain and shear strain [36]. Normal strain is defined as the variation of a material along the axis through which a force is being exerted to the material. Figure 1.13 describes the one dimensional deformation in a material. As can be seen in this schematic, a tension force has caused points A and B to shift to the points A' and B'. The normal or dilatational strain is defined as the ratio of the separation between the two point to the original separation and can be written as follows:

$$\varepsilon_x = \frac{u+du-u}{dx} = \frac{du}{dx} \quad (9)$$

Here ε_x is the normal strain. We can also dv and dwas the elongation along the y and z direction, respectively and similarly define

$$\varepsilon_y = \frac{dv}{dy} \text{ and } \varepsilon_z = \frac{dw}{dz} \quad (10)$$

It is also worth mentioning that the strain values due to seismic waves are in the order of 10^{-6} and require highly sensitive devices to be detected.

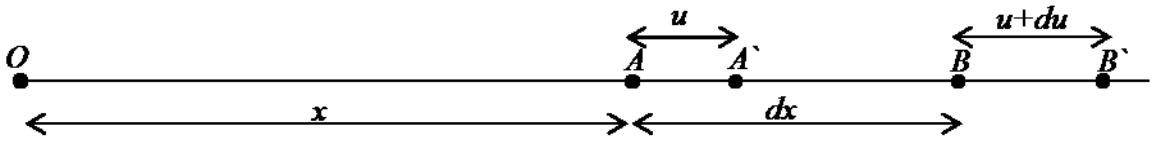

Figure 1.13. Schematic of normal strain definition

There is also another type of strain called shear strain. A simple explanation of shear strain can be given based on the two schematics in Figure 1.14. In the first case (left diagram), we can assume that a block in x-y plane is fixed at its bottom face and a pulling force is exerted on the top right corner of the block. It can be seen that the block will be distorted and the initially

perpendicular faces are inclined. In this case the shear strain would be the angle of inclination shown as α. A more complicated and realistic case is when the whole block body is freely moving except the left bottom corner where it is still constrained. In this case beside the shear strain α, we also have a diagonal rotation shown as ϕ.

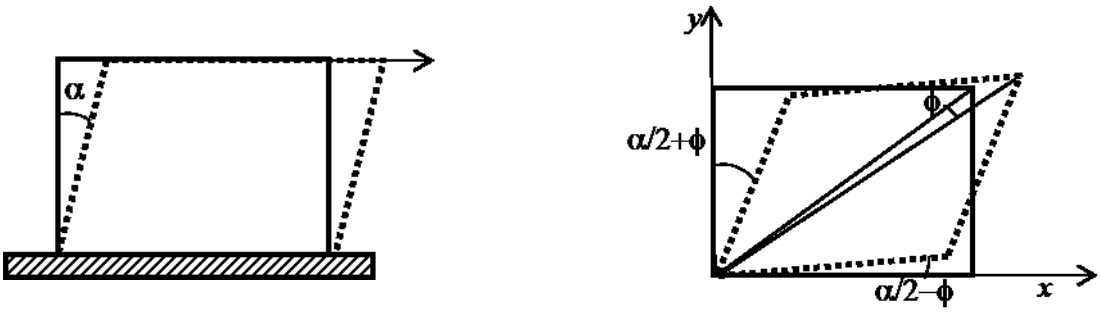

Figure 1.14. Schematic of shear strain definition

$$\frac{\alpha}{2} + \phi = \frac{du}{dy} \text{ and } \frac{\alpha}{2} - \phi = \frac{dv}{dx} \quad (11)$$

$$\text{hence } \alpha = \frac{du}{dy} + \frac{dv}{dx} \text{ and } \phi = 1/2(\frac{du}{dy} - \frac{dv}{dx}) \quad (12)$$

1.3.1.2. Stress

The next important concept within the context of solid materials properties involves the concept of stress. For a material under an applied force, the stress is defined as the ratio of the force to the area over which the force is being exerted. Hence, we can define stress σ, as the following equation:

$$\sigma = \frac{dF}{dA} \quad (13)$$

Similar to the case of strain, stress can also be normal or tangential to the surface of the material. If the force has an angle of ϕ to the surface, we can divide the force into two components of normal and tangential. In the latter case, the stress obtained from the ratio of tangential force to area is called shear stress.

1.3.1.3. Relationship between stress and strain

For a solid substance, there is a linear relationship between the stress and strain due to that stress according to Hook's law [36]. Assuming that a solid is under a tension or compression one dimensional stress, the strain is proportional to the stress according the following:

$$\sigma_x = E\frac{du}{dx} \quad (14)$$

Where E is the proportionality constant known as elastic or Young's modulus. Figure 1.15 demonstrates this relationship for a typical elastic-plastic material. As can be seen in this plot, the solid can undergo certain amount of stress without deformation. For almost any solid substance, there is a limit below which the applied strain is reversible after the load is taken off. This limit is called the yield strength of that material. Beyond this point, the solid suffers some permanent or plastic deformation which is not reversible. However, even for a plastically deformed material some small portion of the deformation is recovered after the removal of the load. The slope at which the deformation is recovered is still equal to its elastic modulus as shown on the diagram.

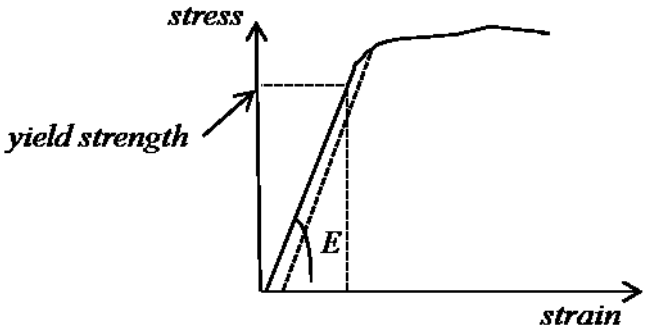

Figure 1.15. Schematic of stress-strain relationship

In the case of three dimensional forces where the stress has some x, y and z component, the stress-strain relationship becomes more complicated. A tension stress applied along the x-axis would permit the solid to elongate along the x direction while it causes contraction in the y and z directions. In this case, there is a proportionality between the deformation in the x direction *du*, and the deformations in y, *dv* and z, *dw* directions. Such a proportionality factor is called Poisson's ratio, υ which is a characteristic parameter, written as:

$$\varepsilon_y = -\upsilon\frac{d\sigma_x}{E} \text{ and } \varepsilon_z = -\upsilon\frac{d\sigma_x}{E} \quad (15)$$

The negative sign is due to the contraction in y and z directions. For most rocks and crystallite materials, υ varies between 0.2 and 0.3. For a case in which the solid is under tensile stress in all three directions, we can write the three components of stress via the following equations:

$$\varepsilon_x = E\frac{du}{dx} = \sigma_x - \upsilon\sigma_y - \upsilon\sigma_z \quad (16)$$

$$\varepsilon_y = E\frac{dv}{dy} = -\upsilon\sigma_x + \sigma_y - \upsilon\sigma_z \quad (17)$$

$$\varepsilon_z = E\frac{dw}{dz} = -\upsilon\sigma_x - \upsilon\sigma_y + \sigma_z \quad (18)$$

Similar to a normal stress-normal strain relationship, there is also proportionality between the shear stress and shear strain. During the propagation of seismic waves in a solid, the distortion in the material will cause some shear strain which is proportional to the shear stress with the proportionality constant G known as the rigidity or shear modulus. There is a relationship between G and E which will be discussed in following chapters where we use that relationship to define an elastic modulus from the shear modulus.

1.3.2. Propagation of seismic waves in solids

We can now use the elastic characteristics of materials defined in the previous section to describe the propagation of seismic waves in solids. To describe the behavior of waves in solid materials, we can use Hook's law to obtain the wave equation for solids. In the most general case, waves are traveling in all three dimensions. However, it is beneficial to assume the simple case of one dimension motion to derive the wave equation using the relationships introduced in the previous section. This could be done by assuming an applied stress and strain along the length of a rod as shown in Figure 1.16 [37].

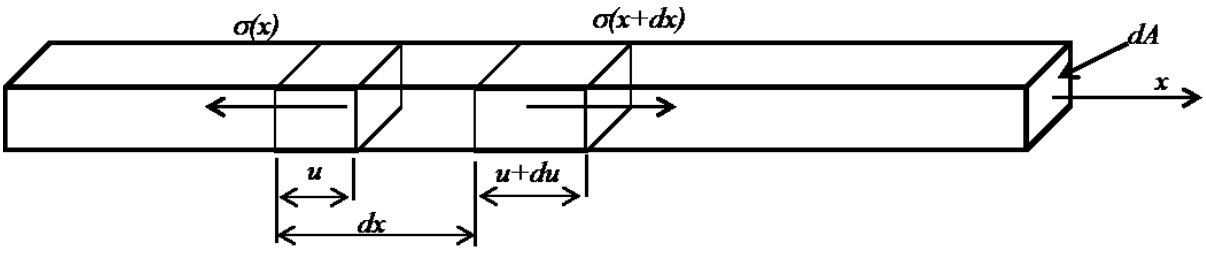

Figure 1.16. Deformation of one dimensional rod caused by longitudinal stress wave [37]

We assume that a rod has cross-sectional area of *dA*, density of ρ and elastic modulus of E. As we can see, an element at position *x* has been moved to the position *x+dx*. It has also been elongated along x-axis by *du*. The net force being applied on this element is the difference between the initial and final force on the element. In this case, force can be described by stress times area, i.e. *σ(x) dA*. The stress at the position *x+dx* is also *σ(x+dx) dA*. The net force over the element can also be described by Newton's motion law where the force is equal to mass of the element *ρdxdA* times the acceleration of particles in the element in the form of d^2u/dt^2. The relationship between the two definitions of net forces is as follows:

$$[\sigma_{(x+dx)} - \sigma_{(x)}]dA = \rho \frac{d^2u}{dt^2} dxdA \quad (19)$$

We can write $\sigma_{(x+dx)} - \sigma_{(x)} = \left(d\sigma/_{dx}\right)dx$ and replacing the stress with elongation based on Eq. 14, $\sigma = E\, du/_{dx}$ we arrive to the following equation:

$$E \frac{d^2u}{dx^2} dx\, dA = \rho \frac{d^2u}{dt^2} dx\, dA \quad (20)$$

Adding the classical form of a dimensional wave equation is:

$$\frac{d^2q}{dx^2} = \frac{1}{V^2} \frac{d^2q}{dt^2} \quad (21)$$

Where the simplest answer for the above differential equation is:

$$q = A \sin k(Vt - x) \quad (22)$$

Comparing Eq. 22 with Eq. 20 results in obtaining the definition for the wave velocity based on density and elastic modulus:

$$V = \sqrt{\frac{E}{\rho}} \quad (23)$$

The three dimensional equation for waves can also be derived a similar manner. In brief, the velocity of compressional (P) and shear (S) waves based on the materials elastic properties can be obtained from the following equations:

$$V_P = \sqrt{\frac{\lambda + 2G}{\rho}} \quad (24)$$

and

$$V_S = \sqrt{\frac{G}{\rho}} \quad (25)$$

Where λ is another characteristic feature of solid materials also known as Lamè's coefficient with the following definition:

$$\lambda = \frac{E\nu}{(1+\nu)(1-2\upsilon)} \quad (26)$$

1.3.3. Types of seismic waves

In the previous sections we described the general characteristics of elastic materials and the relationships between seismic wave behavior and elastic features. Especially, the relationship between the velocity of two types of seismic waves, compressional and shear waves and the elastic features were described. These waves are also known as body waves in seismology. Apart from these two, there are also two other types of wave propagating at the surface known as Rayleigh and Love waves. A short description of each type will be presented in this section.

1.3.3.1. Compressional waves

To describe the type of seismic wave, it is helpful to visualize the motion of particles according to the propagation of compressional wave. A compressional wave causes the particles to move in alternating condensation and rarefaction manner where the solid particles move closer together during the former and further apart during the latter. In fact, in three dimensional space the waves propagate in the form of spheres. As a compression pules is applied to an elastic solid, the zones of compression start expanding outward form the center of the pules in the form of spherical shells. The radius of spheres increases according to the wave velocity V_P as described by Eq. 24. Following the first condensation wave, there is another shell of rarefaction zone expanding with the same speed [38]. Figure 1.17 shows the propagation of these spherical shells according to the propagation of compressional wave.

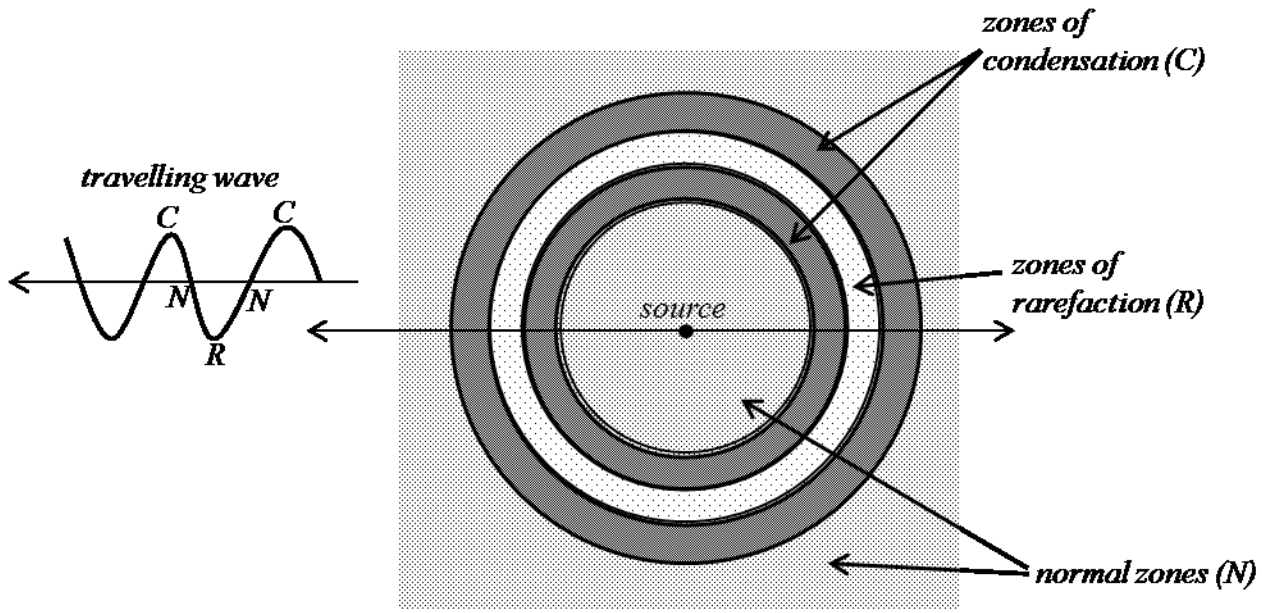

Figure 1.17. Expansion of spherical shells caused by compressional impulse (adapted from [38])

Another form of the equation describing the compressional wave velocity can be obtained by combining Equations 24 and 26:

$$V_P = \sqrt{\frac{E}{\rho}\frac{1-\upsilon}{(1+\nu)(1-2\upsilon)}} \quad (27)$$

1.3.3.2. Shear waves

The motion of particles due to the propagation of shear waves is perpendicular to the direction of wave motion. Similar to the previous case, combining Equations 25 and 26 results in a different description of shear wave velocity in elastic materials:

$$V_S = \sqrt{\frac{E}{\rho}\frac{1}{2(1+\nu)}} \quad (28)$$

And by comparison of Equations 27 and 28:

$$\frac{V_P}{V_S} = \sqrt{\frac{1-\upsilon}{0.5-\upsilon}} \quad (29)$$

This equation suggests that the velocity of compressional waves is always greater than that of shear waves. This is concluded based on the simple fact that the Poisson ratio for an elastic solid cannot be greater than 0.5.

1.3.3.3. Rayleigh waves

Rayleigh waves travel along the surface of solid material. The motion of particles is in the vertical plane and in an elliptical direction as shown in Figure 1.18 [39].

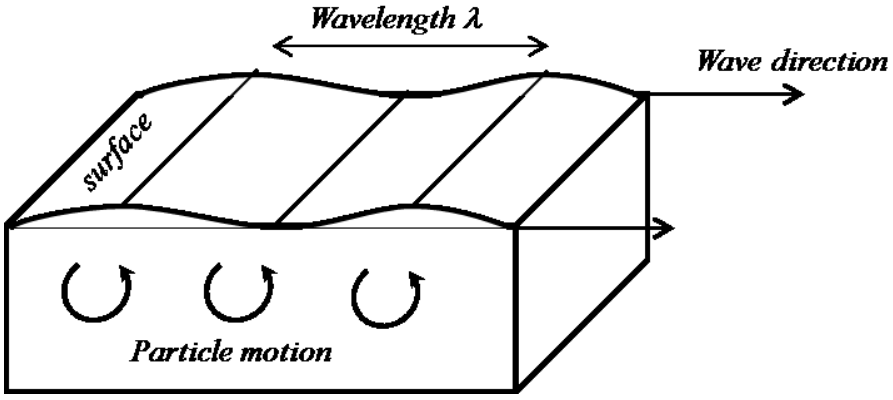

Figure 1.18. Motion of particles as Rayleigh wave propagates (adapted from [38])

The magnitude of the particle motion decreases exponentially with depth. The velocity of Rayleigh waves is smaller than that of shear waves at nine-tenths of shear wave velocity [40]. More on this subject will be presented in the surface wave method chapter. The velocity of Rayleigh waves vary with frequency or wavelength. If the surface layer contains loose material such that the wave speed is very low compared to the dense subsurface layers where the wave speed is potentially higher, the Rayleigh wave velocity is a function of frequency [41]. For very low wavelength compared to the surface layer thickness, the speed of waves is about nine-tenths the shear wave velocity in that layer. In this case, the wave most likely does penetrate the subsurface layers. Similarly, for low frequency or large wavelength waves the surface layer is most likely too thin to affect the wave and the wave penetrate the subsurface layers. The speed of the wave in the subsurface material is about nine-tenths of shear wave velocity in that layer. Such behavior of Rayleigh waves in which the wave velocity is a function of frequency or wavelength is called dispersion [42].

1.3.3.4. Love waves

This type of wave occurs when the surface layer is low-speed overlaying a high-speed subsurface layer [43, 44]. The motion of wave is both horizontal and transverse as shown in Figure 1.19.

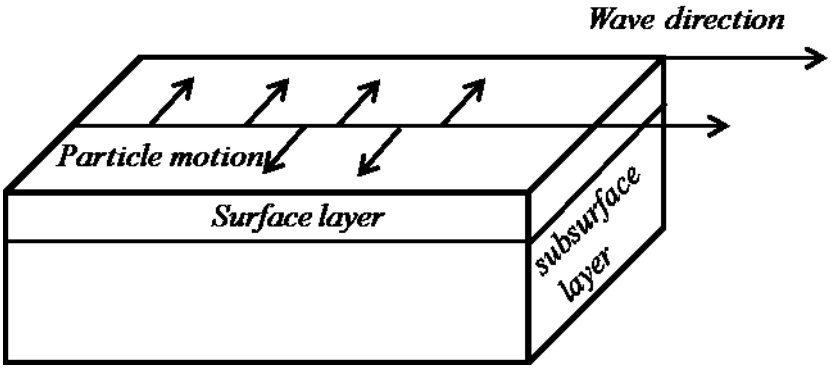

Figure 1.19. Motion of particles as Love wave propagates (adapted from [38])

Similar to Rayleigh waves, this type of wave has also dispersive behavior. The motion of particles is caused by the multiple reflections of waves between the top and bottom layers. For short wavelength, the Love wave velocity is equal to that of shear wave in the surface layer. For large wavelength, the speed of wave is equal to that of shear wave in the subsurface layer. The use of Love waves in seismic analysis is limited as most seismic sensors detect the vertical motion of ground particles and not the horizontal motions.

Different types of seismic waves and their relationship with the elastic properties of materials have been introduced. The next step towards analysis of these waves is to apply appropriate methods corresponding to each type, to obtain the unknown features. However, a key step before performing this analysis is to identify the appropriate conditions and frequencies in the case of surface waves. This is done through investigation of the response from the seismic sensors in the frequency domain and filtering out the unwanted signals. Also, it is helpful to understand how seismic sensors function. These are subjects for the following chapters.

1.4. Thesis overview

The current thesis consists of seven chapters:

Chapter 1 provides an overview of oil sand structure and its geotechnical properties. It also summarizes previous work reported in the literature with respect to the interaction of oil sand ground and active mining face materials with heavy mining equipment, focusing on haul truck interactions. The last portion of this chapter is dedicated to an introduction of seismic wave theory including applications to obtain ground properties.

In order to better analyze seismic data, it is necessary to ensure that an appropriate range of frequencies are selected. This is presented in chapter 2 where the frequency response of seismic results is highlighted. The concept of filtering in the frequency domain is explained and used to identify the presence of different noise sources and the process to eliminate their presence prior to any detailed data analysis.

In chapter 3, a brief introduction to the principles of seismic sensors (geophones) is presented. This is included as it is useful to understand the functionality of the components of a geophone as well as relationships between input and output data flow.

The fact that two different data sets were collected (VIMS versus seismic), necessitates the need for a reliable time scale synchronization. This is discussed and investigated in chapter 4. Using the truck speed as a common baseline permitted the VIMS and seismic sourced data to be compared; performed via a correction factor, applied to the time scales of one data set relative to the other to negate drift in the raw data pairs.

Chapter 5 provides some detail of the methods previously established by other researchers for establishing ground properties from seismic waves. The Matthews surface wave method, based on using a set of waves with known frequency, has been applied to the seismic data in this research, representative of the most widely accepted method to date. Due to the moving nature of the truck, as the wave source; splitting the data into several smaller data envelopes is explained in chapter 5 as a new step prior to applying Matthews surface wave method. The overall performance of the ground in terms of shear modulus is then extracted from the ensuing analysis.

In chapter 6, the results of ground modulus values determined in chapter 5 are compared against the results obtained from VIMS analysis. Combining VIMS strut pressure output (converted to force values passing through the tire to the ground) and accounting for the ground deformation from previously established oil sand strength – deformation relationships permits a ground force stiffness top be realized. This comparison of seismic versus VIMS permits monitoring of truck data by operations to reveal the variation of ground properties as the truck moves along a given haul road.

Chapter 7 presents the key concluding remarks of this thesis.

In chapter 8, recommendations for future work, extending this research further including suggested foci and implementation strategies that might be considered for industry application are outlined.

Chapter2

2. Filtering

Seismic data analysis has been chosen as the tool to discern any correlation between the passive seismic method and the data from VIMS. Similar to any seismic method, the major three components of the analysis are the source, recording device and data processing. As for all seismic investigations, the ground motion is required in order to obtain results. Such motion is normally generated by explosives, hammer or other energy sources. The energy from these sources causes the ground particles to move and vibrate with their density, physical properties, liquid content, etc. All these properties may be extracted from the seismic result through careful processing. Among numerous industries benefiting from these analyses, mining would gain a more detailed understanding of ground versus heavy vehicle interactions. For instance, in oil sand mines it has been reported that the ground underneath trucks and shovels shows significant instability in its properties [12]. It was shown that oil sand undergoes a softening process as it is constantly strained by heavy mining equipment. Ground softening can then result in a larger equipment contact footprint area and higher rolling resistance which eventually causes higher fuel consumption and lower truck tire life. A new unconventional method termed passive seismic analysis has been used over the past few years to identify the properties of oil sand underneath mining equipment [12, 45]. It is called passive since the major source of wave is the moving vehicle and not a controllable static source. However, it is expected that the other sources of waves including engines, pumps and the surrounding noise from other vehicles also contribute to the outcome of measurements. Hence, careful data processing is necessary to distinguish as much wave source as possible and to filter out the unimportant signals (noise). Passive seismic analysis has been successfully used to reveal the interactions between a shovel and the ground underneath via ground behavior during its duty cycle [12].

Apart from the wave source, the recording device is the other major component of seismic measurement. The geophone is the most commonly used instrument to sense the signal caused by ground motion. As will be discussed in chapter 3, modern geophones convert the ground particle motions into a voltage output through the concept of inertia and electromagnetic induction. The output voltage signal is the result of electromagnetic current induced by a moving coil. It is the rate of displacement of the coil and not the absolute value of the displacement that

gives rise to a voltage signal. In fact, the voltage output is theoretically proportional to the velocity of moving particles that cause the motion. However, obtaining a velocity value requires an understanding of the parameters and equations involved in such conversion.

The last and probably the most important part of seismic analysis is the data processing. A great level of knowledge exists on various techniques and methods to analyse the seismic outcome. As mentioned in chapter 1, depending on the purpose of a test and their configuration, various properties can be extracted. Passive refraction seismic analysis has been successfully employed to identify the zones of different stiffness in the oil sand mine [45]. In this thesis, the surface seismic waves are used to explore the change in the properties of the oil sand and correlate them with the on-board truck/VIMS load measurements. As mentioned above, the output voltage of the geophone is a mixed signal that is the sum of various signals from different sources. Therefore, a significant part of data processing is to deconvolute the effect of each source and obtain the desired signal. For this purpose, the first part of this chapter explains the methodology for step-by-step removal of noise of a seismic trace. This is an essential step in the process of finding a meaningful correlation between the ground velocity and voltage output. It is also important to filter out all unnecessary data points to be able to draw conclusions regarding the ground stiffness from a seismic analysis.

Before moving forward into the detail of seismic analysis, it is worth to point out an important difference in this seismic analysis approach from common types of analysis. In a conventional seismic or any passive analysis, the source has a fixed or pre-determined position; the source in our case is moving with a known speed. Here we consider the truck and more specifically the truck tires as the wave source. This results in a very complicated output signal which requires a high level of wave analysis. The interpretation of seismic traces from a dynamic source is somewhat beyond the current state of seismic analysis as well as the scope of this thesis. However, one can simplify the situation by considering the trace of seismic waves as stationary envelopes of signals in small time intervals. To perform such simplification, we must first select the desired envelopes since the whole data range can be split into too many envelopes. The seismic trace from each geophone shows a clear maximum point which can be most likely attributed to the location of the truck at a given time. In contrast to VIMS with the frequency of 1 Hz, seismic traces are recorded with a high frequency of 250 Hz which records 250 data points over the period of one second for each geophone. Hence, we can use the seismic data for the time

interval of one second around the maximum point of the seismic trace. In such small time duration, we consider the truck as a stationary source of wave for all 72 geophones. Then we analyse this envelope using conventional seismic data processing and explore the ground properties in these envelopes. This is covered in chapter 5.

2.1. Seismic data processing

2.1.1. Noise sources

As mentioned above as well as the introduction section of this chapter, the high resolution of seismic data collection compared to VIMS results in including signals from any source of wave in the environment. The high frequency range of measurement leads to obtaining a seismic plot which consists of signals from various sources. Figure 2.1 displays the results from a sample run in an oil sand mine. The data has been plotted in MATLAB software using the codes available online at the University of Alberta website "SeismicLab" [46] data processing package. The raw seismic trace is often plotted as so called "wiggles" plots. The function *wigb* in the "SeismicLab" package is used in this figure. Equation 30 shows the *wigb* function along with the parameters used in it.

$$wigb(d, scal, x, t) \quad (30)$$

This function requires four input parameters to plot the traces. The first parameter, d, is the original seismic data in the form of a matrix with each trace as a column. The second parameter, *scal*, is the scaling factor which basically is a multiplication factor. The third input, x, is a one-dimensional array of the offset or the distance values. In this case it is a matrix of numbers from 1 to 72 with spacing of 1 m. The last parameter is the time value again as 1-dimensional matrix. The time duration of a seismic test was 65 seconds. As can be seen in Figure 2.1, a rough estimate of the truck position can be obtained from this plot. Truck arrives at the first geophone after about 27 seconds from the beginning of the data acquisition.

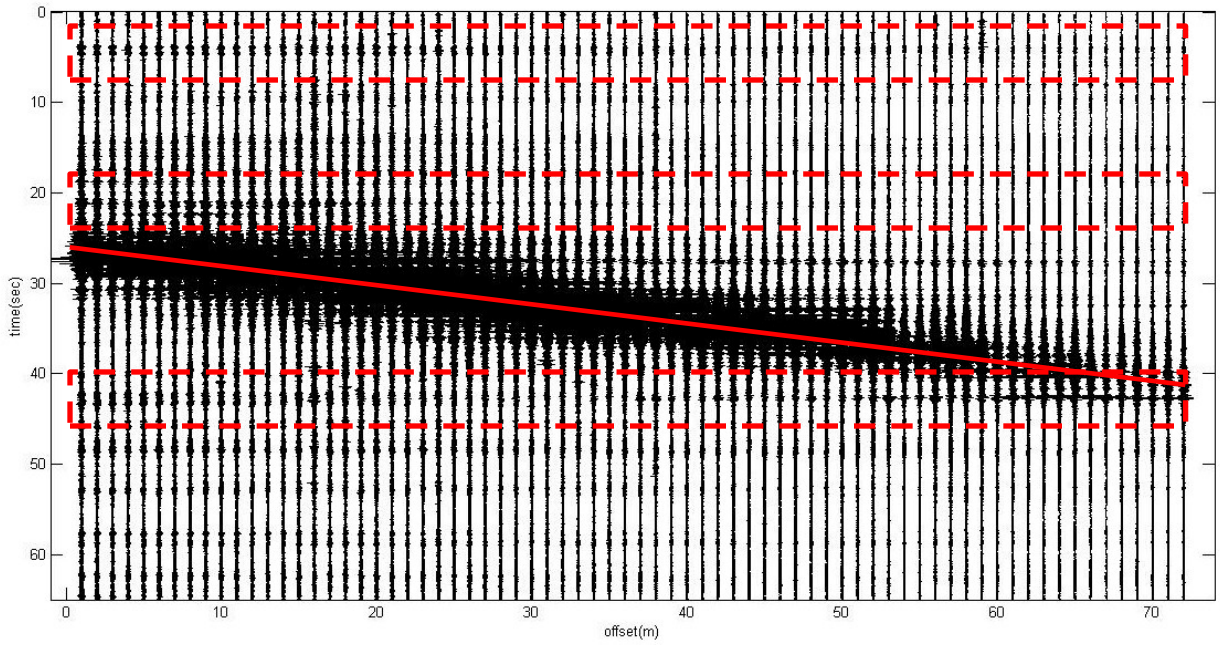

Figure 2.1. Raw seismic traces of a single run

By drawing a straight line passing through all the maximum points we have an estimate of the average truck speed when moving across the geophone arrays. The slope of this line suggests an average speed of 4.8 m/s or 17.3 km/h. The average truck speed from the VIMS data is 4.5 m/s or 16.3 km/h. However, the truck is not traveling at a constant speed as will be seen in chapter 4 showing VIMS truck speed. As the raw data clearly shows, there are several indications of noise in the data. All the geophones are affected by a source of noise that arrives at about 5, 27 and 42 s from the starting time (highlighted in Fig. 2.1). These could be due to the presence of farther equipment such as a shovel or dozer whose signal arrives simultaneously to all geophones. Other signals which are clearly not caused by the truck tire are also present. In order to have a clearer vision of all noise sources it is essential to look at the frequency response of the geophones.

As mentioned it is not easy to identify the frequency response of any wave source by looking at the original data in the time domain. The process of converting to a frequency domain is done using a discrete Fourier transform built-in MATLAB code. The function is basically an algorithm for computing a Fourier transform of a vector. A faster transform for large amounts of data could be obtained when the length of the transformed vector is specified as squared power numbers. This could be the closest squared numbers to the original length of data. Once the transformation is done, we need a frequency vector to be able to plot the data in a frequency

domain. As we know the acquisition frequency of the seismic data was 250 Hz, we can create a vector expanding from 0 to 250 Hz with the same length of the transformed vector. Figure 2.2(a) represents the frequency response of all geophones on a simple 2-D plot. The first observation is that the response is mirrored over the frequency range. This is simply because a Fourier transform breaks up a signal into complex exponentials, and a sine wave is the sum of two complex exponentials.

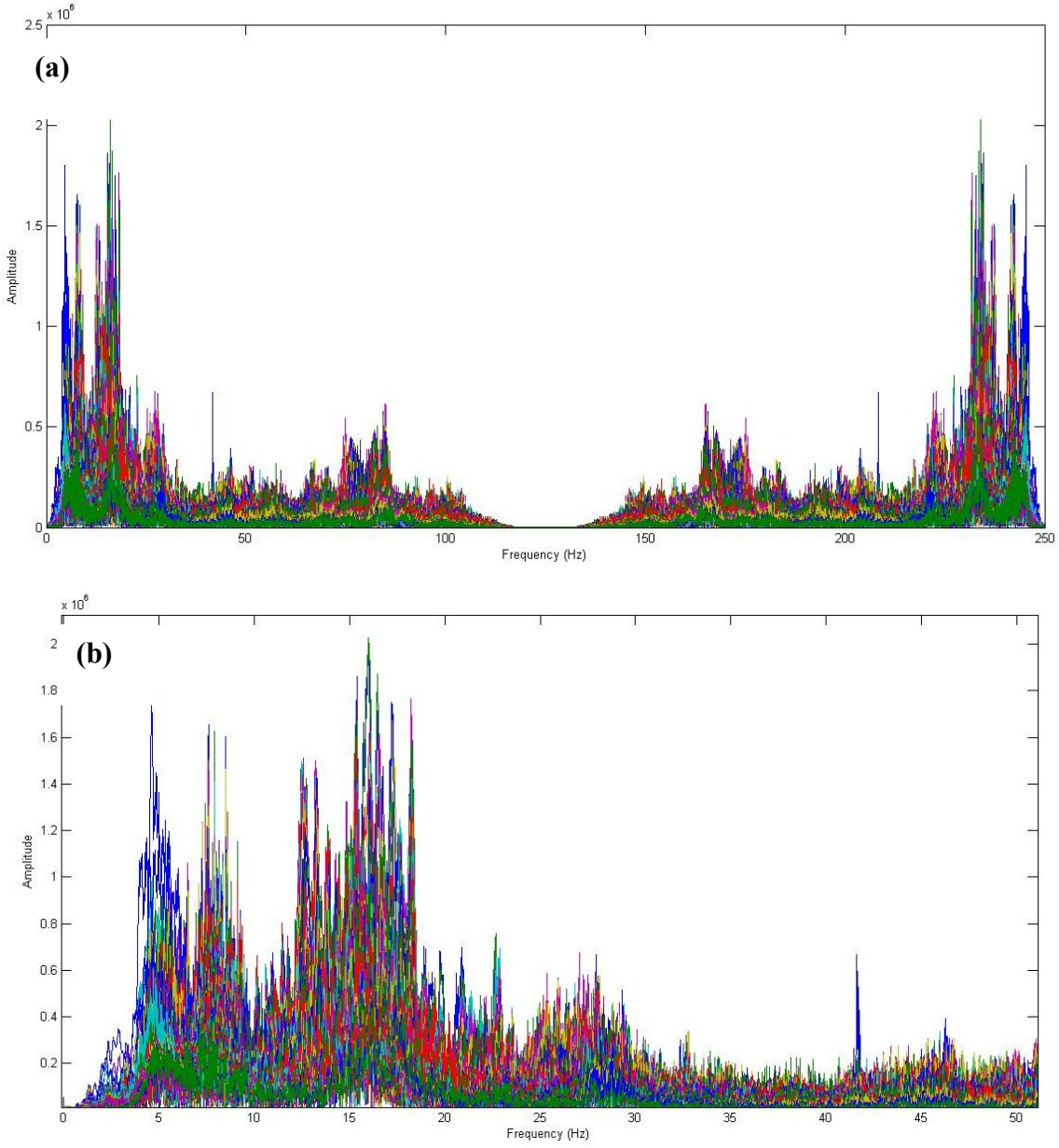

Figure 2.2. Original data in (a) total frequency domain and (b) frequency range of 0-50 Hz

Another important observation is the presence of few major peaks in the frequency domain plot. The two most intense peaks are in the range of 1-10 and 12-20 Hz, respectively. There are also some peaks in the range of 23-32 and 70-90 Hz. In order to indicate whether if all these frequency peaks are originated from the truck movement or any other source, we need to identify the frequency response of these sources. As mentioned above, the truck engine could be a significant source of noise as it is running constantly in a close proximity to the geophone array. According to the manufacturer, the Caterpillar 797 truck hydraulic and cooling systems, and engine power were listed in the range of 700 rpm (low idle) to 1950 rpm (high idle) and 1750 rpm in the standard condition [47]. Converting these values to frequency units, we find frequency ranges of 11.6, 32.5 and 29.5 Hz as the low idle, high idle and standard condition frequency responses, respectively. A quick comparison between these values and the whole data frequency response in Figure 2. 2 can easily show the traces of the motor and hydraulic systems on the geophone data. This indicates that we need to remove these effects from the original data before drawing any conclusions from seismic analysis. This is normally done through filtering the data in a certain range of frequency. Another important source of the noise stems from the tire lugs vibrations as previously reported by Joseph and Welz [48] according to the following equation:

$$f_T = \frac{100}{36\pi} V_T \quad (31)$$

Where f_T is the tire vibration frequency and V_T is the truck speed in km/h. According to the truck velocity from VIMS, the truck travels in the speed range of 7-29 km/h which corresponds to the frequency range of 6.5 to 25 Hz. The average truck speed based on VIMS and seismic were 16.3 and 17.3 km/h which corresponds to 14.4 and 15.3 Hz, respectively. This type of noise source mainly contributes to the major peak in the frequency response centered around 16 Hz in Figure 2.2. The small peak in Figure 2.2 at around 42 Hz can also be considered as noise however, its source cannot be identified with the current information. As most noise sources are now identified, the next step is to apply various filtering methods and examine the influence and effectiveness of each method on the seismic data and obtain the most optimal filtering formulation.

2.2. Filtering methods

Filters are the most common way to remove unwanted components of the frequency response of any data series. It is normally done by applying a so called bandpass filter to exclude a certain range of frequency from the whole data. Some filters also can mute a portion of data that is above a certain frequency limit (lowpass or high pass filters). Filters can be applied both in time and frequency domains however the latter is usually preferred due to its simplicity. In the time domain, the filter is applied through convolution methods as opposed to the frequency domain in which the filter is applied by multiplication. A great level of knowledge exists towards filter design methods. In general, we can divide these methods into two categories of infinite impulse response (IIR) and finite impulse response (FIR) [49]. The major difference between the two is that the former's response involves internal feedback and usually behaves in a decaying manner while the latter responds in finite duration and reaches zero in a finite time. There are numerous advantages of FIR over IIR methods including better applicability to integer math, easier to design and greater stability, etc. The known types of filter in IIR category are Butterworth, Chebyshev types I and II, Elliptic, and Bessel. On the other hand, methods like windowing and multiband and transient bands (equiripple and least square) are among the most widely used approaches in the FIR category [49]. To explain the math and equations behind each method is out of the scope of this thesis. However, the procedure to implement selected methods to our seismic data analysis to achieve the least level of noise will be presented in the following paragraphs.

In order to design and implement filters to the seismic data, MATLAB software was used. In particular, the filter design and analysis tool (FDA tool [49]) is a user interface that enables the design of various filters by inputting the corresponding specifications for each filter. Two different types of filter were selected to be applied to our seismic results.

2.2.1. Lowpass filter

In the first method, a lowpass filter in the FIR category using the equiripple approach was designed. In a lowpass filter, the signals with frequencies lower than the cut-off frequency are passed and the signals beyond this cut-off value are reduced in their amplitude. In the toolbox, the required parameters are the sampling frequency which is 250 Hz in our case; ending of a passband frequency F_{pass}, and beginning at the stop frequency F_{stop}. The last two values could be

examined to achieve the best result. A snapshot of a typical FIR filter using 10 Hz and 15 Hz as the passband and stop frequency values is demonstrated in Figure 2.3. As can be seen in this example, the signals with frequencies above 10 Hz will be reduced in their amplitude and those with frequencies above 15 Hz will be removed from the original data.

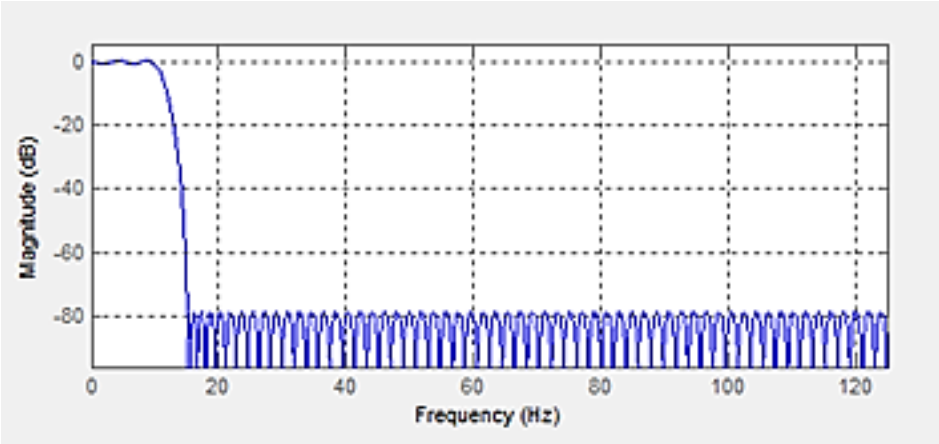

Figure 2. 3. Lowpass filter with F_{pass}=10 Hz, F_{stop}=15 Hz and sampling frequency of 250 Hz

At this point, the filter can be stored as a vector which will then be applied as the convolution vector to the original data. The results for various passband and stop frequency combinations are presented in the next section.

2.2.2. Bandpass filter

Another type of filter called bandpass was also used in our analysis of the seismic data. In this method, the bandpass is defined by four corner frequencies named as f_1, f_2, f_3 and f_4. This type of filter is also known as an Ormsby filter in the literature. The parameters f_1 and f_4 are called low-cut and high-cut frequencies and f_2 and f_3 are low-pass and high-pass frequencies. Any signal with frequency below f_1 or above f_4 will be rejected from the data. The filter is linear between f_1 to f_2 and f3 to f_4 and flat between f_2 to f_3. An example of this filter with frequency values of 5, 7, 13 and 20 Hz is shown in Figure 2.4.

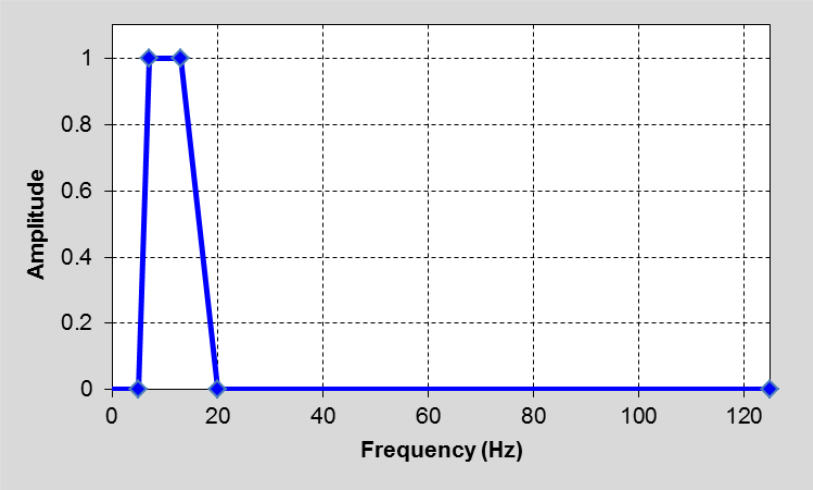

Figure 2.4. An example of a bandpass filter with 5, 7, 13 and 20 Hz as corner frequencies

Similar to the previous design, MATLAB was used to create this filter. In this case, the function *bp-filter* available in the "SeismicLab" [46] package was used. As shown in Eq. 32, the function requires six parameters:

$$[A] = bp\_filter(d, dt, f1, f2, f3, f4) \quad (32)$$

where *d* is the matrix of the entire seismic data, *dt* is the sampling frequency which is 0.004 s in our case, and the four corner frequencies of the Ormsby filter. The function returns the matrix *A*, which has the same dimensions of the original data, *d* and can be presented in the form of wiggle plots using the *wigb* function. In the following section, the process of applying these filters to the original data and their effects on the appearance of data is provided. Once the proper filter design methodology is obtained, we can seek the relationship between the geophone output and the velocity as well as the analyzing individual envelopes of signals for our stationery studies which are the purpose of the next chapters.

2.3. Filter implementation

As mentioned in the previous sections, the use of filters to remove undesired signals and obtain the representative set of signals to analyze is essential. In this section, the process of application of the two previously mentioned filters on the appearance of the seismic results will

be demonstrated in a step wise manner. In particular, using the bandpass filter allows for isolating the signals in a certain frequency range and observing their effect in the wiggle plots.

Figure 2.5 shows the design of a lowpass filter that removes the signals with the frequencies above 35 Hz. In order to apply this filter to the data, first a vector containing the filter is created. The vector is then convoluted to the original matrix of data using the built-in MATLAB function *conv* function.

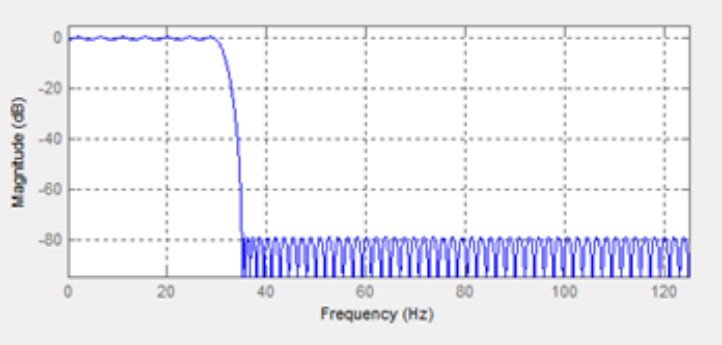

Figure 2.5. Lowpass filter with F_{pass}=30 Hz, F_{stop}=35 Hz and sampling frequency of 250 Hz

Figure 2.6 demonstrates the seismic data after applying the lowpass filter with F_{pass}=30 Hz, F_{stop}=35 Hz and its new frequency response obtained similar to the original data.

(a) Lowpass filter applied to seismic data

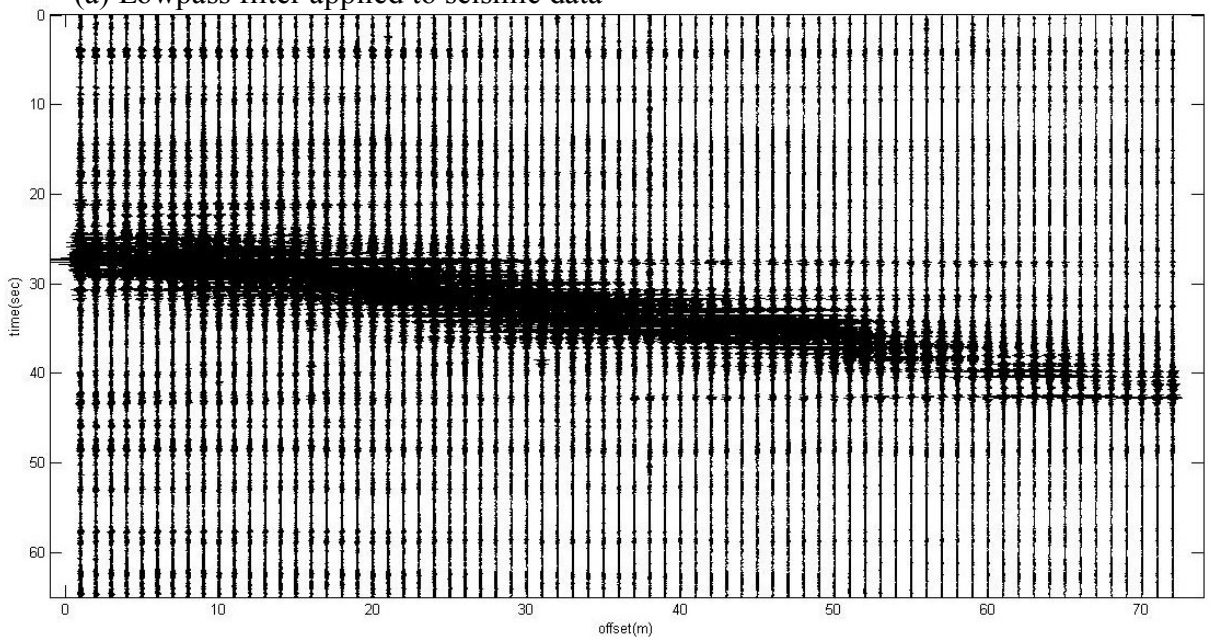

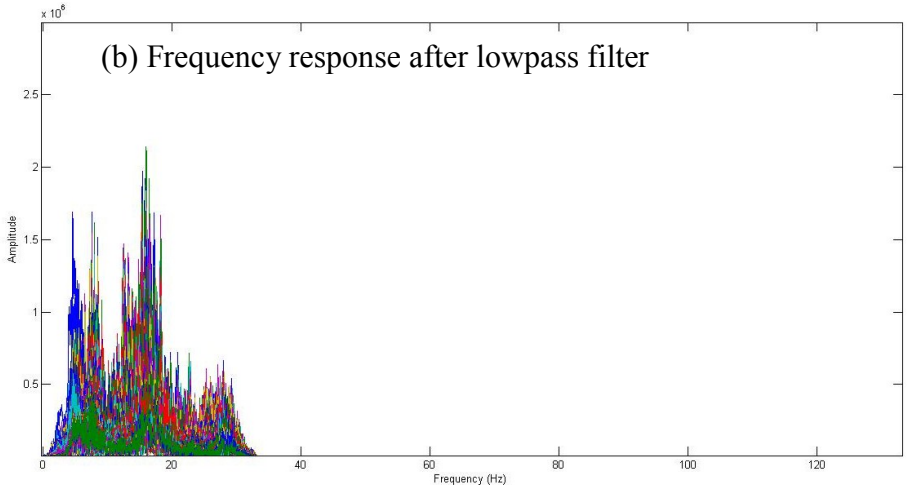

Figure 2.6. (a) Filtered seismic data and (b) corresponding frequency response after applying the lowpass filter with F_{pass}=30 Hz, F_{stop}=35 Hz

A quick comparison of the seismic data in Figure 2.6 to that in Figure 2.1 suggests a very small difference in the appearance of the data. This is expected since the signals with frequencies in the range of 0-30 Hz occupy most of the data. The next step is to lower the admission range of the lowpass filter to stopping smaller frequencies. Figure 2.7 depicts the result of application of a lowpass filter with F_{pass}=10 Hz, F_{stop}=15 Hz and the corresponding frequency response of the filtered data.

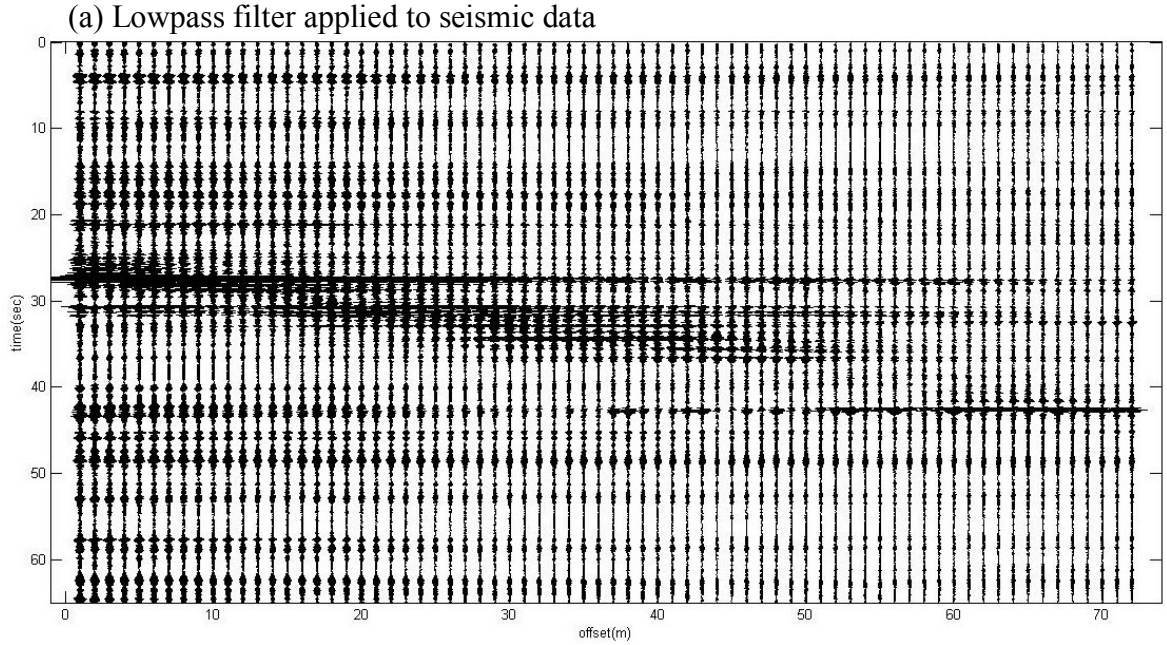

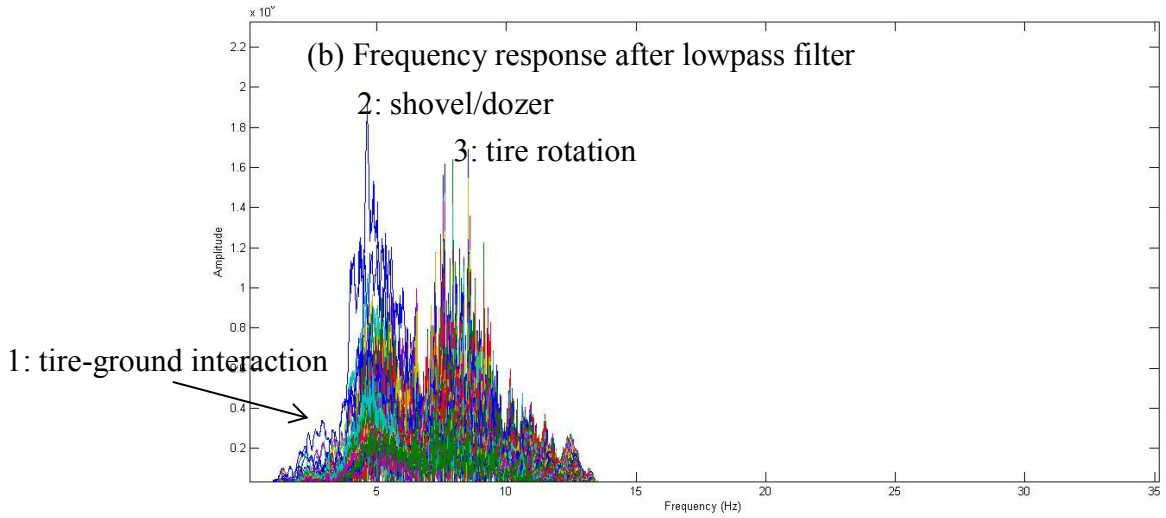

Figure 2.7. (a) Filtered seismic data and (b) corresponding frequency response after applying the lowpass filter with F_{pass}=10 Hz, F_{stop}=15 Hz

Figure 2.7 shows that there is a significant change in the appearance of the seismic traces upon applying the new filter. As the frequency response suggests, all the signals above the 15 Hz are removed. It also shows that there are still three distinct regions in the frequency domain being 0-2 Hz, 2-8 Hz and 8-15 Hz. The filtered seismic plot also shows that beside the major truck movement trace, the effect of the two noise sources of constant distances from the geophone arrays still persist. In order to distinguish the effect of each source a different type of filter known as a bandpass filter was used. Using this filter, one can select a certain region of the frequency domain. An important function of such a filter in our case is to identify the frequency range corresponding to the two constant noise traces in the seismic result at around 27 and 42 seconds. For this purpose, in the bandpass filter the four corner frequencies of 3, 3.5, 6, 8.5 Hz were used. Using the *bp_filter* function in the "SeismicLab" package [46], we can apply this filter to the original data and observe the results. Figure 2.8 shows the seismic trace filtered using the above mentioned bandpass filter. As the seismic plot shows, the filter has been able to isolate the effect of the noise sources which are located at the same distance from the geophone arrays. A careful investigation of the camera record from the field tests suggests that the noise could be due to the operation of the shovel and a dozer at constant distance from the geophone arrays. Hence, it is very important to remove these noises from the seismic result to obtain meaningful data for analysis.

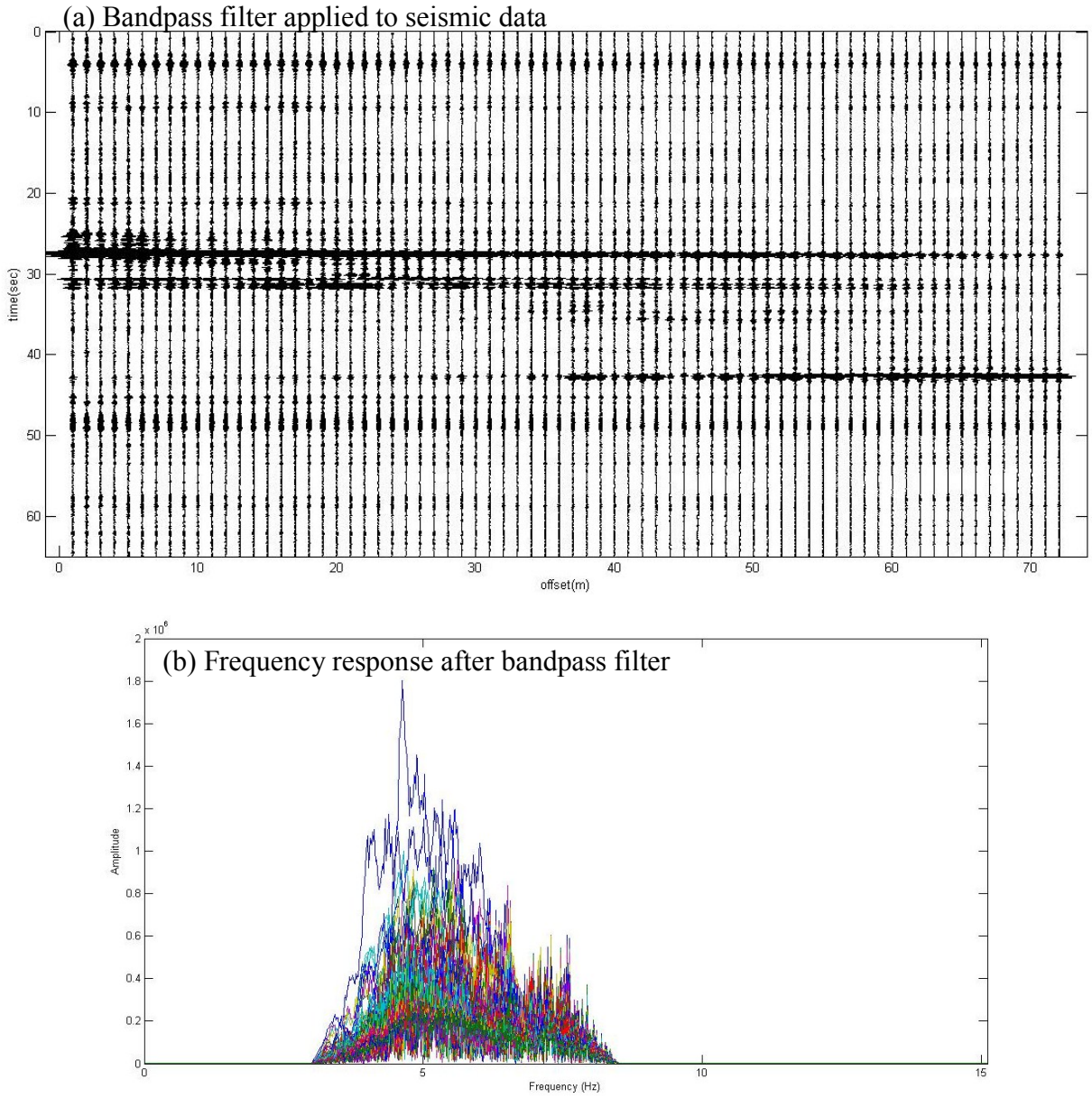

Figure 2.8. (a) Filtered seismic data applying the bandpass filter with corner frequencies F_1=3 Hz, F_2=3.5, F_3=6 and F_4=8.5 Hz and (b) the corresponding frequency response of the data

2.4. Optimized filtering options

Now that the nature of the two main sources of the noise is identified, we can use the lower frequency signals as the assumed pure truck motion effect on the geophone arrays. Several configurations of the application of the filters on the data are provided in the next few paragraphs. In the first case, the two filtering approaches were used to isolate the signals in the

range 0-2.5 Hz. Figure 2.9 shows the results of applying a lowpass filter with F_{pass}=2 Hz, F_{stop}=2.5 Hz as well as a bandpass filter with F_1=0 Hz, F_2=1, F_3=1.7 and F_4=2.5 Hz.

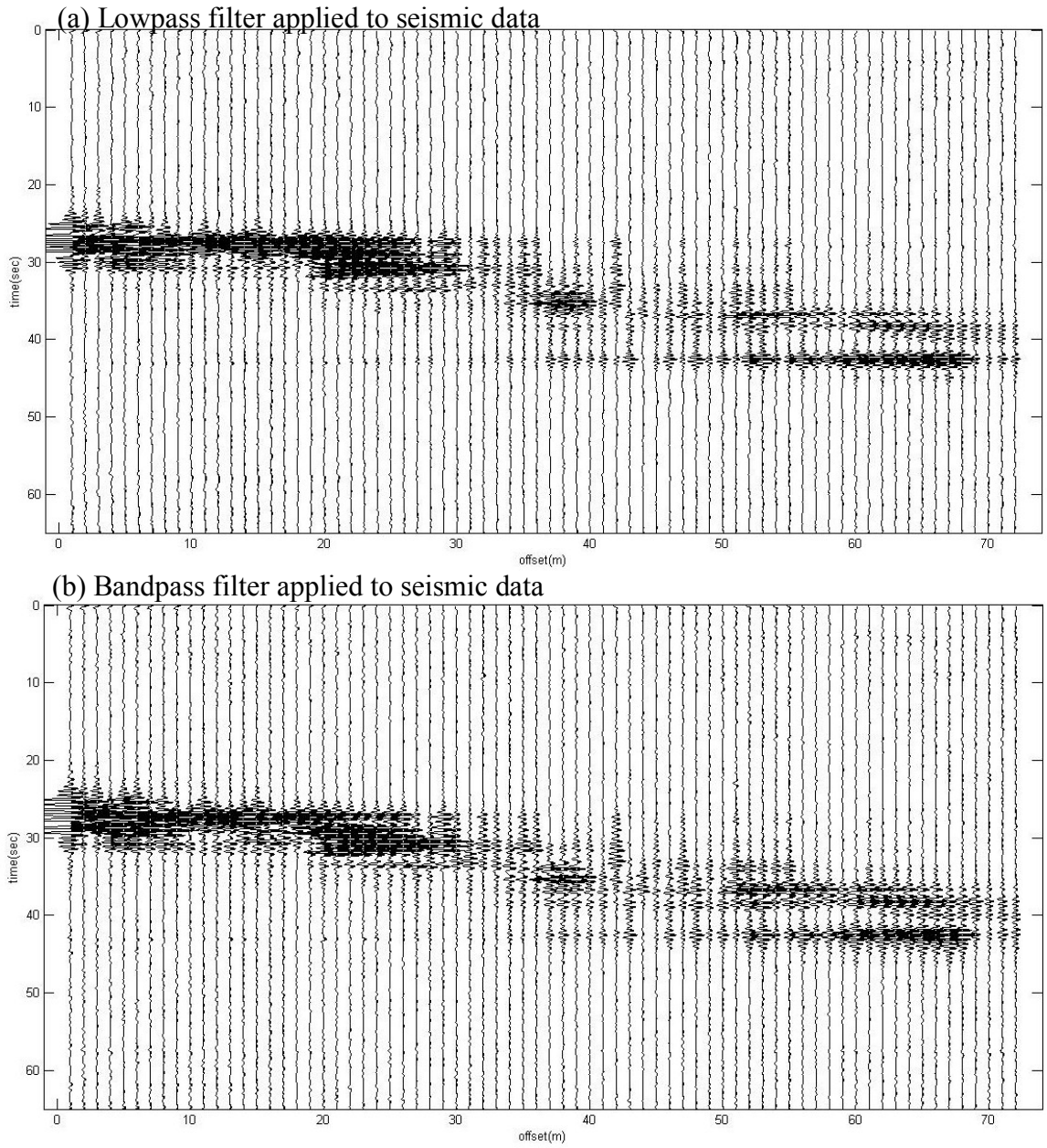

Figure 2.9. The seismic result after applying (a) lowpass filter with F_{pass}=2 Hz, F_{stop}=2.5 Hz and (b) bandpass filter with corner frequencies F_1=0 Hz, F_2=1, F_3=1.7 and F_4=2.5 Hz

As both filtered seismic graphs in Figure 2.9 show, the traces follow a trend similar to the motion path of the truck. This suggests that the utilization of the low frequency signals is the

most appropriate method for isolating the most useful part of the seismic data. As both plots show, the effect of noise source close to 27 s time line is mostly diminished. However, the presence of some noise signals around the time 41 s still persists. Interestingly, this set of noise signal is mostly evident towards the end of arrays. This highlights the importance of the choice of upper limit frequency when applying a bandpass filter. It is possible that some signals in the regions above 2 Hz still contain contributions from the shovel or dozer. In other words, an overlapping of signals might happen in the frequency range of 2-8 Hz where both truck and shovel/dozer have contributions in the original data. To eliminate such overlapping issue, the most intuitive approach would be to further tighten the passband in filtering. Figure 2.10 demonstrates the result of applying a bandpass filter which removes all the noise signals with frequencies over 2 Hz. As the plot shows, the signals with constant arrival time of about 41 s are not visible using this filtering option. This will be the first option for filtering which will be used in the next chapters. The second filtering option is designed based on removing the signals with over 20 Hz frequencies. This is to investigate the signals due to the tire rotation as well as the low frequency signals. This will be demonstrated in chapter 5 where the effect of different frequency choices for obtaining the shear modulus is investigated.

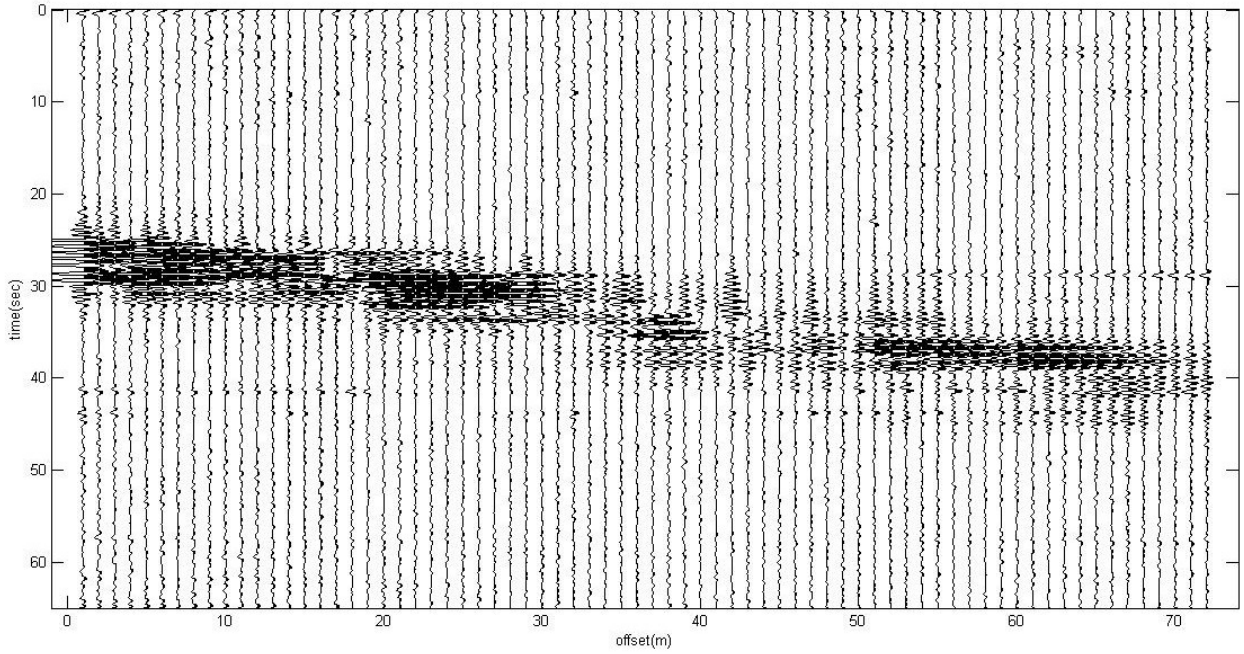

Figure 2.10. The seismic result after applying bandpass filter with corner frequencies F_1=0 Hz, F_2=1, F_3=1.5 and F_4=2 Hz

The application of the above mentioned two filtering options and their effects on the surface wave seismic analysis will be investigated in chapter 5. The first filtering option will also be used to clear the trace of each geophone and have a better vision of the maximum peak. The result will be used in identification of the drift in time scales of the VIMS against seismic data. It will also be used to calculate the area underneath these peaks which could provide new insights towards the properties of ground along the geophone arrays. The latter is the subject of last chapter where the results of surface seismic analysis and VIMS are correlated.

Chapter 3

3. Seismic sensors

The geophone is the most common type of sensing device or seismometer used in seismic analysis. It basically measures the motion of the vibrating ground surrounding it. The main function of a geophone is to convert the motion of the ground into a voltage as an output. The intention of a seismograph unit (seismometer and its recoding unit) is to measure the micrometer or even nanometer scale motion of the ground material [50]. The main considerations regarding such measurement are as follows:

The entire body of the sensor is being affected by the ground motions. Hence, it is not possible to measure the displacement versus a fixed reference point. However, the seismic waves induce temporary movements that could cause accelerations which can be measured using the geophone. This is the basic principles behind inertia seismometers. In other words, continuous motions with constant velocity might be detected but cannot be correctly measured by the geophones [51].

Another point to consider when designing a seismometer is the range of frequency and amplitude of the seismic waves. Ground motions as small as 0.1 nm can be caused by seismic signals. On the other hand, in an earthquake, movements as large as 10 m could also happen. This means a broad dynamic range of $10/10^{-10}$ or 10^{11}. In terms of frequency, the band ranges from 0.00001Hz -1000Hz. These resulted in developing numerous types of sensors such as short period (SP), long period (LP), broad band (BB) or very broad band (VBB) with desired dynamic and frequency detection ranges [52] .

3.1. Seismometer

3.1.1. Mechanical seismometer

Almost all seismic sensing devices are based on the inertia of a suspended or proof mass. The motion of the proof mass relative the ground motions is then used as the measuring parameter. In order to explain the theory of how the seismometer works, it seems useful to qualitatively demonstrate its function using a simple mechanical inertia seismometer (Figure 3.1).

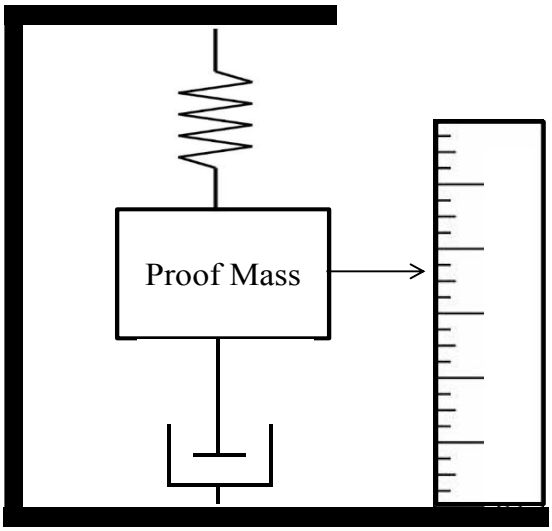

Figure 3.1. A simple mechanical inertia seismometer [adapted from [53]]

Figure 3.1 represents a conventional inertia seismometer that consists of a proof mass suspended on a spring, a dashpot to dampen the motion of the proof mass so that it does not vibrates near the resonance frequency of the system and a linear measure towards the relative displacement of the proof mass with respect to the ground. As a large signal from the ground reaches the seismometer, the whole frame would move up. At the same time, the proof mass also moves down relative to the frame and this causes a phase shift of π in the measured displacement. In the case of a sinusoidal ground signal, as the ground moves up and down, a similar response is detected by the proof mass with a phase shift of π. When the frequency of the signals is large enough, the amplitude of the proof mass displacement is equal to that of the ground (gain=1). On the other hand, at low frequency, the ground moves so slowly that the mass has the time to follow the ground motion and both the phase shift and the gain become small. In the case when the ground has the frequency close to or equal to that of resonance, the mass would get pushed in such a way that it shows larger amplitude (gain >1)[51]. The situations mentioned above are schematically illustrated in Figure 3.2 for a sensor with the resonant frequency of 1 Hz.

3.1.1.1. Theory and principles

The basic principles of a simple mechanical seismometer were explained in the previous paragraphs and now we can see the application via theoretical calculations of the sensor response [35]. We assume that the vertical ground motion is expressed as u(t) and the displacement of the

proof mass relative to earth is z(t). The total displacement of the mass is then expressed as u(t)+z(t). There are two forces being applied to the mass: the spring force (F_s) and the damping force (F_d).

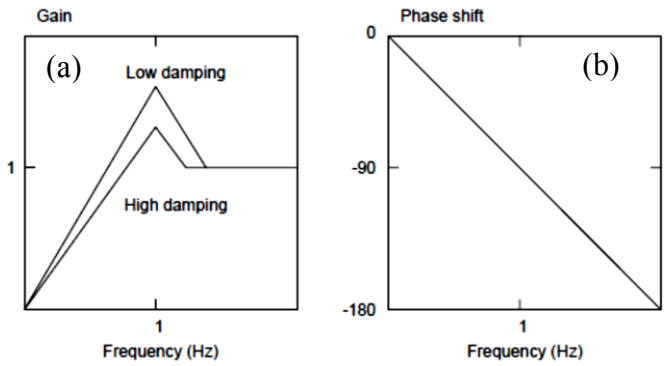

Figure 3.2. The amplitude (a) and frequency response (b) of a 1 Hz resonant frequency seismometer [54]

The spring force opposes the mass displacement and is as follows:

$$F_s = -kz \quad (33)$$

where k is the spring constant. According to a simple mass-spring system, we can define $\omega_0^2 = k/m$ as the resonant angular frequency of the system where $\omega_0 = 2\pi / T_0$.

The damping force is proportional to the mass velocity and is as follows:

$$F_d = -D\dot{z} \quad (34)$$

where D is the damping constant.

Based on the Newton's laws of motion, F=ma where a is the acceleration. The acceleration of the proof mass is expressed as:

$$- kz - D\dot{z} = m\ddot{z} + m\ddot{u} \quad (35)$$

By replacing the ω_0 and defining $h=D/2m\omega_0$ as the seismometer damping constant, we will have the following:

$$\ddot{z} + 2h\omega_0\dot{z} + \omega_0^2 z = - \ddot{u} \quad (36)$$

This equation shows that the earth acceleration can be obtained from the measurement of mass displacement and its time derivatives. In the cases of very high frequency, the acceleration term becomes dominant and we can approximate the ground acceleration as $\ddot{z} = - \ddot{u}$ and the

negative sign suggests a π shift in the response. At very low frequencies, the z term becomes important and we can write:

$$\omega_0^2 z = -\ddot{u} \quad (37)$$

This suggests that at low frequency, the relative displacement of the mass is proportional to the ground acceleration. The negative sign in this case is only due to the phase shift between the acceleration and displacement. In the cases where the damping constant, h is very high, we can write:

$$2h\omega_0\dot{z} = -\ddot{u} \quad (38)$$

Here, the seismometer velocity is proportional to the ground accelerations. In other words, the seismometer displacement is proportional to the ground velocity.

The easiest way to solve equation (36) is to assume a harmonic signal for the ground motion and solve it in the frequency domain [35].

$$u(t) = U(t)e^{-i\omega t} \quad (39)$$

The displacement response can also be expressed as the following:

$$z(t) = Z(t)e^{-i\omega t} \quad (40)$$

We can now have the following equations:

$$\ddot{u} = -\omega^2 U(\omega)e^{i\omega t} \quad (41)$$

$$\dot{z} = i\omega Z(\omega)e^{i\omega t} \quad (42)$$

$$\ddot{z} = -\omega^2 Z(\omega)e^{i\omega t} \quad (43)$$

Replacing the above equations in equation (36) and dividing by the $e^{i\omega t}$ factor results in obtaining the relationship between the $Z(\omega)/U(\omega)$ which is called the frequency response function $T_d(\omega)$:

$$T_d(\omega) = Z(\omega)/U(\omega) = \frac{\omega^2}{\omega_0^2 - \omega^2 + i2\omega\omega_0^2 h} \quad (44)$$

The $T_d(\omega)$ is a complex function that can be written as:

$$T_d(\omega) = A(\omega)e^{i\phi(\omega)} \quad (45)$$

where $A(\omega) = |T_d(\omega)|$ is the amplitude and $\phi_d(\omega)$ is the phase displacement response.

Again, we can see that when the frequency is high, $A(\omega) \rightarrow 1$ that means a gain in value of unity. Similarly, at low frequency $A(\omega) \rightarrow \omega^2/\omega_0^2$. For high damping, $A(\omega) \sim \omega/2h\omega_0$. Figure 3.3

demonstrates the amplitude and phase response of a seismometer with the natural resonant of 1 Hz and damping constant between 0.25 and 4. As can be seen in these graphs, at high frequency, the amplitude response is 1 and the phase response increases to π. A low damping constant (h< 1) results in a peak in the amplitude response at the resonant frequency. The seismometer is called critically damped when h = 1. The proof mass returns to its initial position at the least possible time in this condition [51].

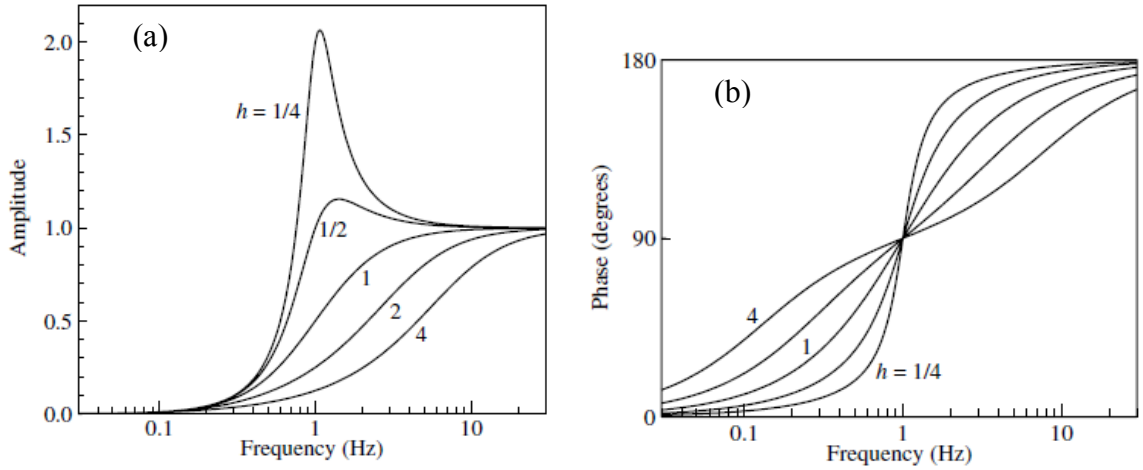

Figure 3.3. The amplitude (a) and frequency response (b) of a 1 Hz resonant frequency seismometer with damping constant 0.25[35]

3.1.2. Electromagnetic geophone

The formulation mentioned above is the basic principles of almost all conventional seismometers. In a geophone, the dashpot has been replaced by a coil moving in a magnetic field. The electromagnetic field generated in this coil in response to the relative displacement of magnet which is fixed to the frame acts as an opposing or damping force. In this case, the resonant frequency ranges from 5-50 Hz. Figure 3.4 shows a typical moving coil geophone with all components exposed.

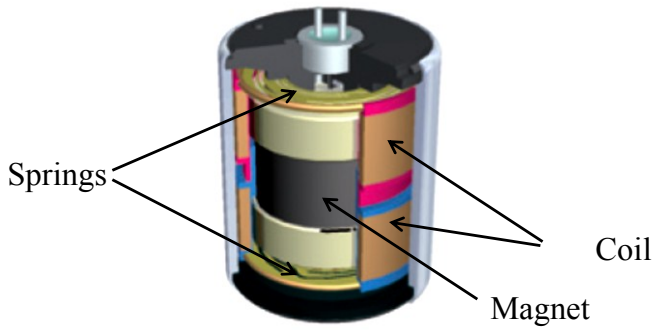

Figure 3.4. A moving coil geophone with its component [55]

3.1.2.1. Principles of geophone

The electromagnetic induction principle based on Faraday-Lens law is used in this system [56]:

$$v \propto dz/dt \text{ or } \dot{z} \quad (46)$$

where v is the voltage generated by a moving coil in a magnetic field. Two more parameters are added to this case compared to a mechanical seismometer: S_G which is the sensitivity or generator constant with units of $V/m.s^{-1}$ (typically ranges between 30- 500 $V/m.s^{-1}$), and R_G as the resistance of the coil in Ohms. In this case, $v = S_G\dot{z}$ and we can write:

$$F_d = S_G I = S_G v/ R_G = S_G^2 \dot{z}/ R_G \quad (47)$$

and hence D constant in equation (2) is S_G^2/ R_G. Dividing by mass results in

$$D/m = S_G^2/mR_G = 2h_G \omega_0 \quad (48)$$

where h_G is the electromagnetic damping constant. In the case of mechanical sensor, the Z(w) was the output. In this case, the obtained output is the voltage proportional to the proof mass velocity $\dot{Z}(\omega) = i\omega Z(\omega)$ and S_G. The displacement frequency response in this case is:

$$T^v_d(\omega) = \dot{Z}(\omega)S_G/U(\omega) = \frac{i\omega^3 S_G}{\omega_0^2-\omega^2+i2\omega\omega_0^2 h} \quad (49)$$

The voltage output from the geophone can then be expressed in the form: $V_G = H_G \times A_G$ where H is a transfer function and A is any type of input including ground displacement (U), velocity (dU/dt) or acceleration (d^2U/dt^2) [57]. The seismometer voltage response can be expressed in terms of these inputs in the following equations:

$$V_G = S_G \frac{i\omega^3}{\omega_0^2-\omega^2+i2\omega\omega_0^2 h} U \quad (50)$$

$$V_G = S_G \frac{\omega^2}{\omega_0^2 - \omega^2 + i2\omega\omega_0^2 h} \frac{\partial U}{\partial t} \quad (51)$$

$$V_G = -S_G \frac{i\omega}{\omega_0^2 - \omega^2 + i2\omega\omega_0^2 h} \frac{\partial^2 U}{\partial t^2} \quad (52)$$

Figure 3.5 demonstrates a comparison schematic of the amplitude frequency response of mechanical and electromagnetic seismometers based on three different inputs. The resonant frequency is assumed to be 1 Hz. The slope of each portion of a graph is also shown. It is interesting to note that each curve can be translated to another by varying the slope by one unit up or down. From the curves corresponding to the electromagnetic sensor it may be seen as the ground velocity is equal to the direct output value of the geophone at $\omega > \omega_0$. However, it should be noted that there is a phase variation which causes a difference between the input and output values. It is possible to correct the data for the phase change by performing a deconvolution technique [58]. However, in most circumstances such correction results in a change in the amplitude and hence, the correlation between the ground velocity and the output response might also be altered. Moreover, in most cases the sensor is used for measuring signals at frequencies below ω_0.

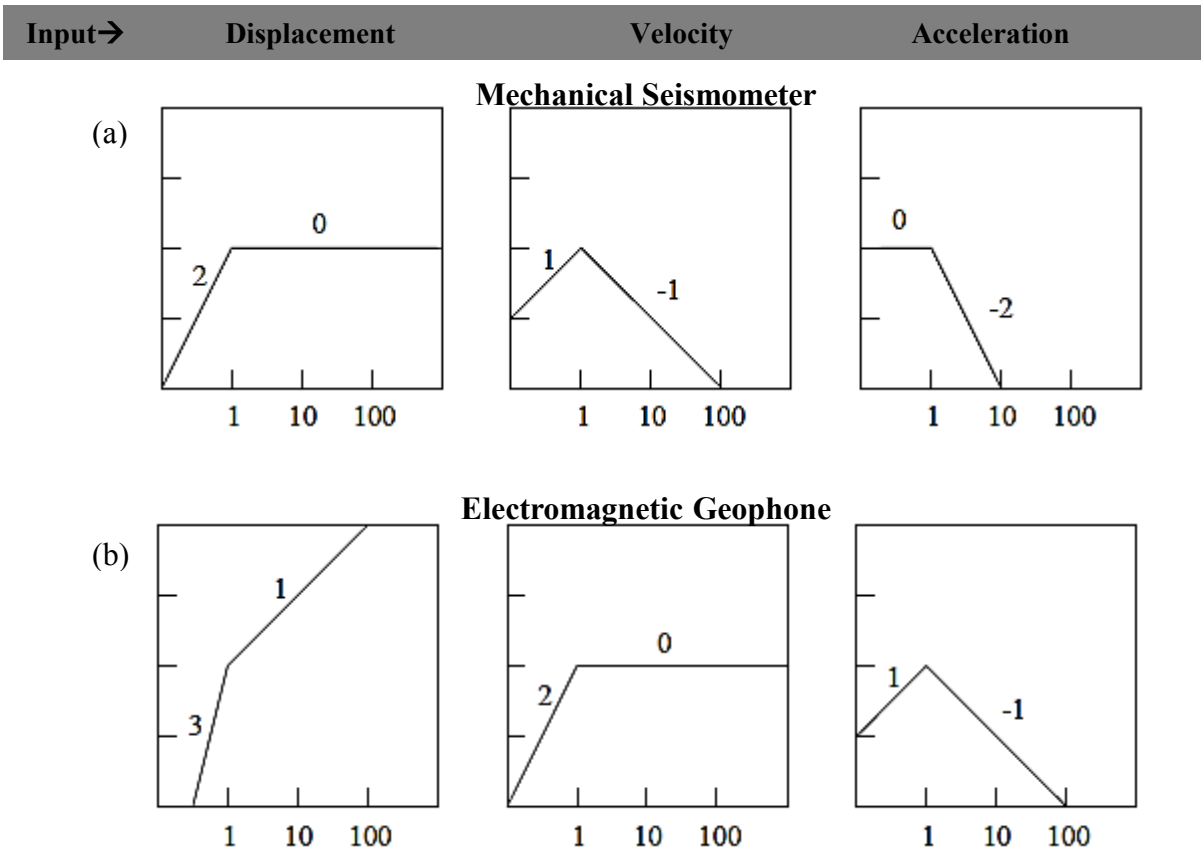

Figure 3.5. The amplitude response of mechanical (a) and electromagnetic geophone (b) with the resonant frequency of 1 Hz [adapted from [51]]

3.1.3. Geophone parameters

As was shown in the previous section, seismometers have certain characteristic parameters that are designed for different purposes. The selection of the appropriate geophone should be made by considering the frequency range at which it will be used. Other factors such as dynamic range, sensitivity, linearity and output are also of importance in choosing the most suitable sensor. In the following sections, a brief description and functionality of each of these factors will be discussed.

3.1.3.1. Frequency response range

Every sensor is designed to work in a certain range of frequency. In general, they are designed to have a flat velocity or acceleration response in a specified frequency range. In those cases where this range is exceeded, the response can be affected by the probable damage to the geophone. Also, it is recommended to use every sensor in its specified frequency band where its

response is linear and predictable. It should also be noted that some parameters such as dynamic range and sensitivity could be altered by varying the frequency range. For instance, a sensor might have a dynamic range of 100 dB in the frequency range of 0.01 to 50 Hz and 150 dB in the range of 0.01 to 20 Hz. Such a sensor is expected to show more noise when used above 20 Hz [59].

3.1.3.2. Sensitivity

Generally the sensitivity of the sensor is defined as the change in the output values in response to the unit change in the signal that is being measured. For some geophones, the sensitivity is specified in terms of $V/m.s^{-1}$. This is the same number used in Eq. 45. It is worth mentioning that reporting the sensitivity is this format might not be able to provide quick information about the smallest signal that can be detected by geophone. This is another way of describing the geophone sensitivity. In many cases, this is restricted by the level of the noise caused by the electronics. For instance, in some geophones the number of turns for the coil wire can be altered by using a different wire size to achieve certain sensitivity. On the other hand this might cause the resistivity to increase which in turn increases the generator constant or the sensitivity.

3.1.3.3. Dynamic range

The ratio between the largest and smallest signals detected by the geophone is defined as its dynamic range [51]. For instance, the smallest detectable displacement in a 1 Hz sensor is 0.1 nm at 1 Hz. Assuming sensitivity values of 300 $V/m.s^{-1}$, the output value of $0.1*2*\pi*300=188$ nV is obtained. On the other side, the mechanical limitations of the sensor allows for maximum displacement of 10 mm. This will result in the dynamic range of 10 mm/0.1 nm = 10^8 = 160 dB. However, to obtain the same voltage output at 0.1 Hz the displacement should be increased by three orders of magnitude. This means that the dynamic range will decrease by three orders of magnitude.

3.1.3.4. Linearity

The most convenient sensor is the one that has a linear transfer function. This means that the output is directly proportional to the input. This could be difficult to achieve in some cases where

springs are used. It is normally a challenge to get the springs to behave linearly. Linearity is usually not specified in the specification sheets of the instrument.

3.1.4. Analog to digital conversion

To be able to analyze the signals obtained from a sensor, it is first necessary to convert the analog signals to a data format readable by computers, i.e. numbers. The process of converting a continuous signal to a series of numbers is called analog to digital (ADC) conversion and is performed by AD convertor. In this section, a brief explanation of this process and the contributing parameters is provided.

The conversion from an analog signal to digital involves two major steps of sampling the signal in discrete time intervals and then, assigning a number to each sample and outputting the results in the form of code. In such process, there will be some errors introduced into the data since some parts of the original signal are lost during the process. Before introducing the most common ADC method, several parameters involved in this process are described.

Resolution is the smallest portion of the analog signal that can be detected. For instance, most common ADCs are able to detect as low as a 1μV step. However, for a seismometer such as a passive seismometer with output values in the order of nV, the convertor requires a preamplifier to be able to perform the conversion. *Gain* or sensitivity will be expressed in terms of counts/V. For a resolution of 10μV, the gain would be 1 count/10^{-6}V or 10^5 counts/V. *Sampling rate* is the number of samples acquired per second. It is in the range of 1 to 200 Hz for seismology analysis. The dynamic range of the ADC is the ratio of the largest to the smallest number it can produce. The dynamic range is usually given in terms of bit available in output data. For example, a n-bit convertor has 0-2^n numbers as its output.

Several methods and algorithms have been used for converting the analog results to the digitized data. A brief description of these methods is given here. The ramp ADC is amongst the simplest method of digitization. Figure 3.6 demonstrates the operation of a ramp ADC where the analog signal enters the comparator. It then triggers the control logic unit to send a ramp to send a ramped signal through the generator with a minimum level of zero to the comparator. The counter also counts the ramping level simultaneously. Once the ramp signal is equal or larger than the input signal the counter stops counting and the last counted level would be the output voltage. The counter will be reset after a certain time and the next sampling will start. One of the

disadvantages of this convertor is that it is quite slow when working with a high number of samples for high resolution measurements. Some modifications have been applied by implementing more complex logic systems to improve this system [51].

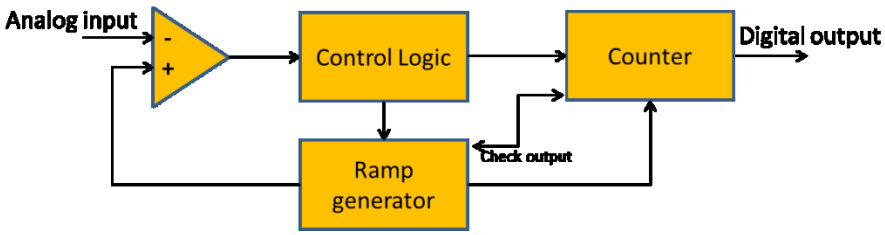

Figure 3.6. A simple schematic of ramp ADC [adapted from [51]]

Several digitizers have also been developed within the concept of multi-channel ADCs. In the least complex scenario, each channel works with a separate digitizer and the results will be collected in a computer. In some cases where the incoming signal is very weak such as in seismology and earthquake analysis, it is usually necessary to pre-amplify the signal before entering the digitizer. Gain ranging has been used in these cases as a method to amplify the gain of the ADC using a program. However, in this method the resolution might be compromised when a low gain is used for a signal with both small and large amplitudes. Another method for improving the weak signal is to use oversampling. In this case the signal is samples at a higher rate to improve the amplitude and then is subjected to a low pass filter. It is then sampled at a lower rate where the samples are the average of the many points taken at high rates. This method enables for obtaining higher accuracy and a higher dynamic range.

One of the most commonly used methods in converting analog signals is the Delta-Sigma ADC. The basic principle behind this method is similar to oversampling. It samples the signal at low resolution and at a fast pace and then applies a running average to these input values to improve the resolution. The simple schematic of this convertor is illustrated in Figure 3.7. In summary, the analog signal goes through an amplifier and then a differential amplifier and an integrator. It then gets digitized and the digitized signal goes into a digital filter where the running average of all values is calculated and resampled at a lower rate.

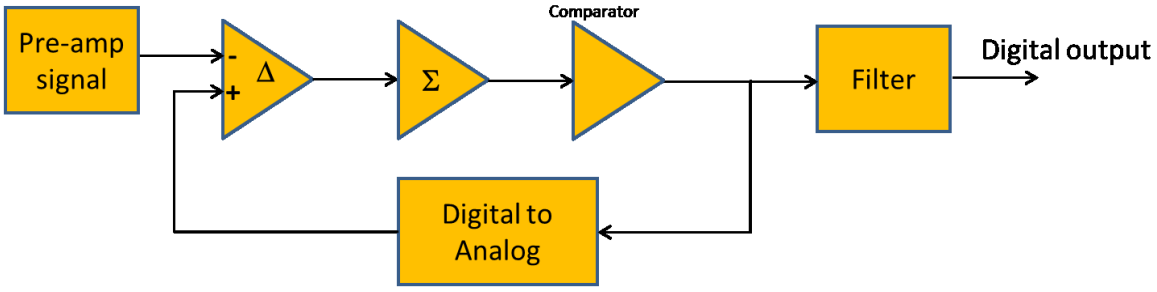

Figure 3.7. Schematic of Delta-Sigma ADC [adapted from [55]]

Although many other methods have also been implemented to convert an analog signal and also to improve the resolution and the speed of this conversion, the detailed description of all these methods is out of the scope of this thesis. Readers might refer to this chapter's references and the citations therein for further information about seismology instrumentation.

Chapter 4

4. Drift correction

In order to investigate the interaction between a moving truck tire and the ground beneath, which is oil sand in our case, three different sets of data were collected. The available techniques to collect such data in our studies were the truck on-board data acquisition system known as vital information management system (VIMS), a video camera recording the location of the truck and the seismic data. To be able to find correlations between the loading data from the truck and the ground properties requires a careful examination of this data. In the other words, some level of synchronization is necessary when the information comes from three different devices with specific sampling rates and independent time scales. In this chapter, a detailed overview of the process of minimizing the so-called drift in this data and in particular the seismic and VIMS data will be provided.

The on-board data collection system, VIMS consists of a large number of sensors manufactured for the truck to provide vital live information about the health and function of different parts of the truck. An important role of VIMS is to monitor the weight of the truck in empty and loaded states through strut suspension pressure measurements [60]. This allows not only for tracking the overall dynamic weight of the truck but also identifying the loads over individual tires. This ability can be further utilized to study the different key parameters including pitch, rack and roll as recently reported by Joseph [7]. Truck payload and velocity is acquired via VIMS data. An important factor to be considered is the rate of data acquisition in VIMS. According to the manufacturer, the data is acquired with the rate of 10 Hz. However, an internal process of data sampling for enhancing the signal to noise ratio is also performed. The output data is given at the rate of 1 Hz. The sampling rate of the camera is 30 Hz but converted to 1 Hz.

In our seismic analysis, an array of 72 vertical geophones with resonant frequency of 1 Hz were used. The geophones were placed along an oil sand route where the truck hauls material from the shovel towards a dumping area and travels back to the shovel. The sampling rate was 250 Hz with a geophone spacing of 1 meter. The total time of data acquisition which includes the time the truck reaches the array as well as the time for the truck to pass through the geophones. The data acquisition rate for the geophones at 250 Hz allows for sampling a wide range of

frequencies caused by various sources including the truck components, other heavy vehicles as well as the tires. The concept here was to use the truck and tires in particular as the source for generating seismic waves. However, the sampling environment is not isolated from surrounding sources and hence the data contains some noise signals. The high resolution of seismic data is beneficial for identifying such sources and mitigating their effects in the seismic traces. Such process can be prepared in the frequency domain where the characteristic frequency range for each particular source is known. In this way, we can obtain a more meaningful correlation between the VIMS and seismic data. As mentioned above, the first step in correlating these results is to assure that they are time synchronized. Since the time scale for the seismic analysis is limited to 65 seconds, we could minimize the amount of drift within this time frame. Moreover, due to its higher resolution the seismic trace is chosen as the reference for performing the drift correction. In the following section, the detailed process of minimizing time drift is presented.

4.1. Drift correcting procedure

4.1.1. Matching unfiltered seismic and VIMS

As mentioned above, in order to perform a drift (possible time difference) correction we must assume one set of data as the reference. Assuming the seismic results as the reference seems to be a more appropriate choice, as we have about 250 seismic data point for every second as opposed to only one VIMS data points per second. The first step is to obtain a clear picture of the drift and its amount in the data. For this purpose, two sets of VIMS and seismic results from the same run were chosen. Figure 4.1 shows the first trace of seismic data along with the VIMS results. In this case, two sets of VIMS data for the left-front (LTF) and left-rear (LTR) are selected. As can be seen, the VIMS data for the two selected struts show no drift between the two data sets since they were collected with the same onboard instrument. Furthermore, the seismic trace displays a maximum point at t=27.7 s. It is worth mentioning that to simplify the calculations both data sets were re-scaled to start from time zero. As explained, these calculations are made in the time frame of 65 s which is the maximum length for the seismic analysis. It seems safe to assume that t=27.5 s is the moment at which truck is the closest to the target geophone.

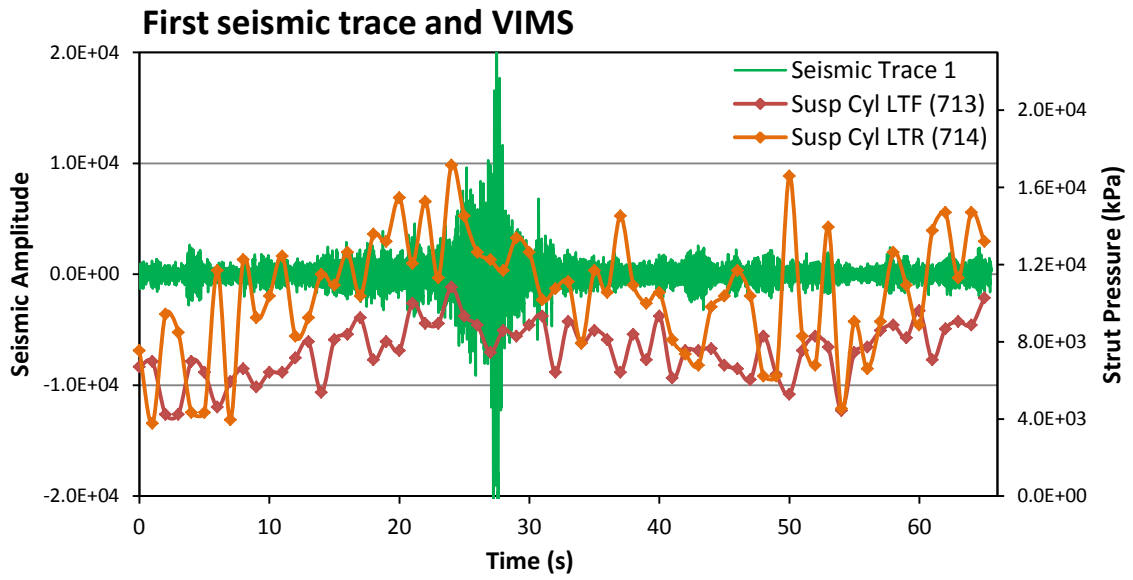

Figure 4.1. The first seismic trace and the VIMS result

As the resolution of the VIMS data is only 1 s, we cannot match the truck position based on trace 1 with any of the VIMS points. Hence, we need to move along the seismic traces until the maximum point overlaps with a data point in VIMS. This first occurs at t=28 s at geophone 7 as shown in Figure 4.2.

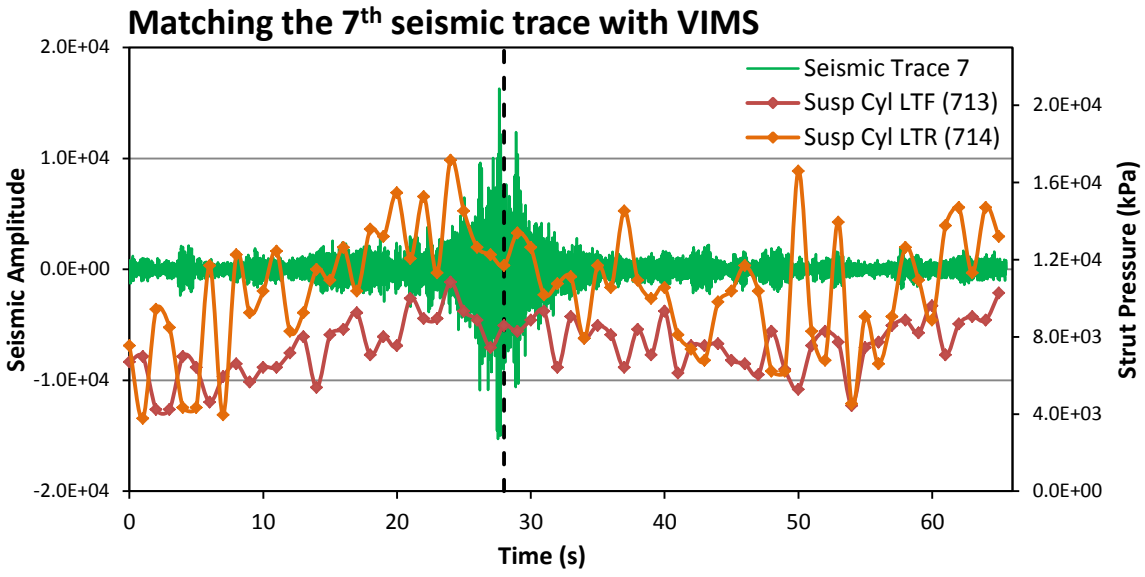

Figure 4.2. The seismic trace 7 showing good match with the VIMS result

4.1.2. Matching filtered seismic and VIMS

Moreover, due to the high number of data points in the seismic trace as well as the presence of several noise sources, it is beneficial to perform such matching process on the filtered signals. As discussed in chapter 2, related to filtering methods, the original data series contain noise signals within several ranges of frequency. Data in the low frequency range of 0-5 Hz still showed some presence of shovel/dozer vehicles working at a farther distance from the geophone arrays. Similar noise traces from shovel/dozer have been observed by other researchers analysing similar set of data [48]. This resulted in an even smaller range frequency for filtering the seismic data. The most promising results obtained from removing all the signals with frequencies above 2 Hz. This leads to obtaining a clearer vision of ground response due to truck motion without interference of any noise source. Therefore, in the following sections the seismic traces of below 2 Hz frequency are used for the matching process.

Figure 4.3 demonstrates the first and 7^{th} seismic traces after the filtering process. To better visualize the matching process, the absolute values are plotted. The solid line over the seismic trace shows a simple fitted curve obtained using the Gaussian curve fitting option in MATLAB. The fitted curve helps better realize the exact time of the maximum point in the seismic trace. Similar to the cases of the original traces, the maximum point of trace 1 lies somewhere between times 27 and 28s. The maximum point of the trace 7 overlaps with t=28 s where a VIMS data point is also present. The trace 7 in the seismic analysis is the first location where we see a fairly good overlapping of a point in the VIMS data with the position of the truck based on seismic results. The traces between these two numbers expectedly show maximum point between the time 27.5 and 28 s.

We now assume that both data series are perfectly synchronized up to this point. This is a necessary assumption as the truck approaches the geophone array after about 27.3 s and its location cannot be traced before this time. The following section summarizes the step-by step procedure towards correcting the drift existing between the seismic and VIMS data.

4.1.2.1. Step-by-step drift correcting procedure

In this section, the details of all the steps involved in the process of correcting the drift between the two data series of seismic and VIMS is outlined.

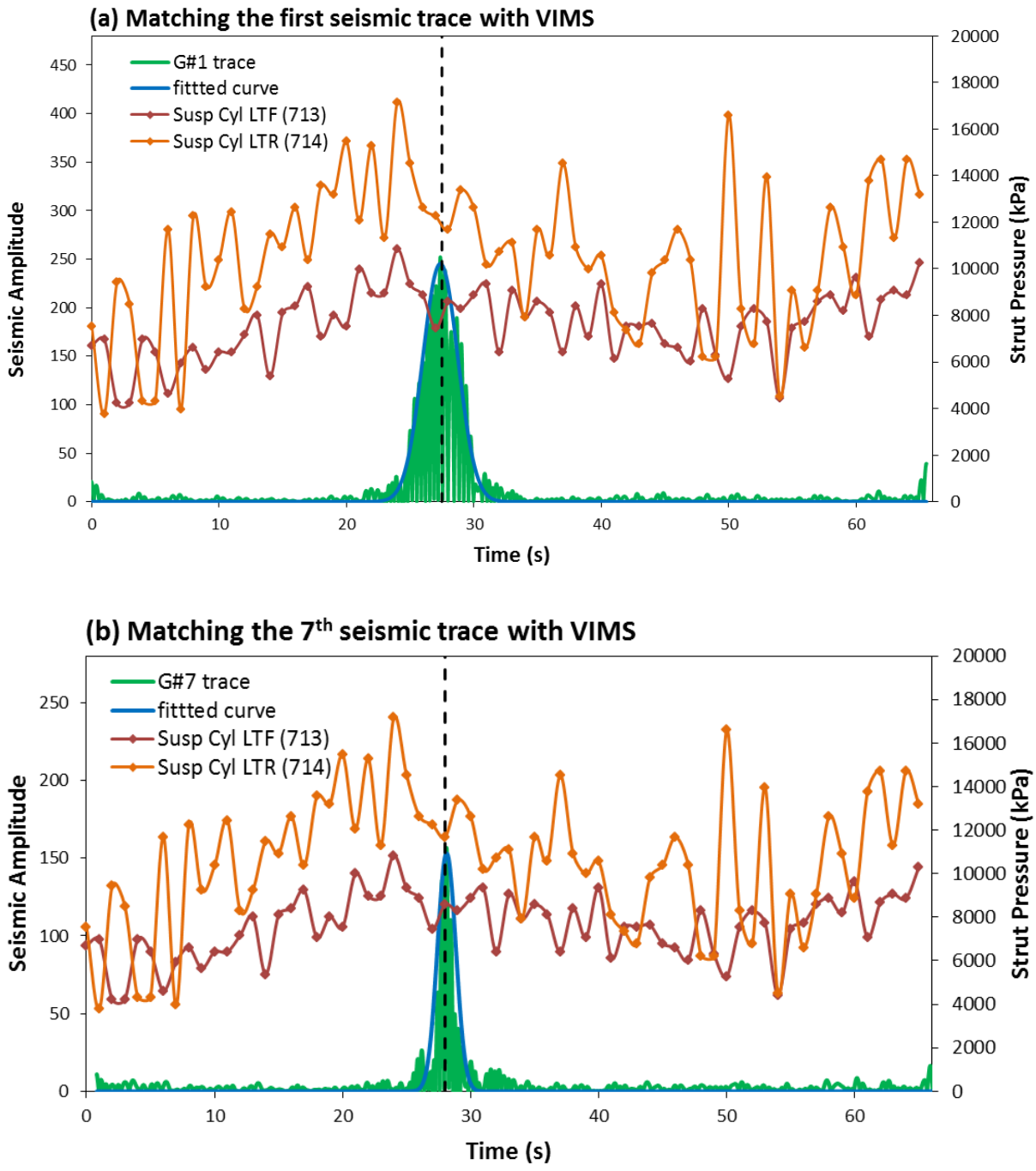

Figure 4.3. The filtered seismic trace for geophone(a) 1 and (b) 7

1- As mentioned previously, the first step in the drift correction process is to define a reference point at which we assume a negligible amount of drift. The difference in the resolution of the two data series, our calculations are limited by the lowest resolution set which is VIMS in this case. Starting with the first seismic trace, we can find the position of the truck based on the

location of the maximum point. Fitting the data as well as filtering help to better identify this point as shown in the previous section. If the time corresponding to this maximum value contains any decimal number, the matching of such points with any VIMS points which do not have any decimal number would not be possible. Hence, we need to look for the first seismic trace for which the time of the maximum point is a number without the decimal part. This occurs for the seismic trace 7 as shows in Figure 4.3. Once this point is found, we can assume that the two data series, seismic and VIMS have the least amount of drift.

2- The next step is to use the VIMS data to predict the location of the truck after a certain amount of time. This is possible using the truck speed values and the time frame between t_0=28s and time at any of the peak values of the VIMS data. Figure 4.4 represents a portion of the VIMS data for the speed of truck during the 65 seconds of seismic measurements. At any given time for VIMS, we have the speed of the truck. For instance, at t_1=30s we can obtain the speed of the truck for every second. During the time frame of t_0=28s and t_1=30s we can predict the distance traveled by truck by multiplying the average speed of truck within these 2s by time (2s).

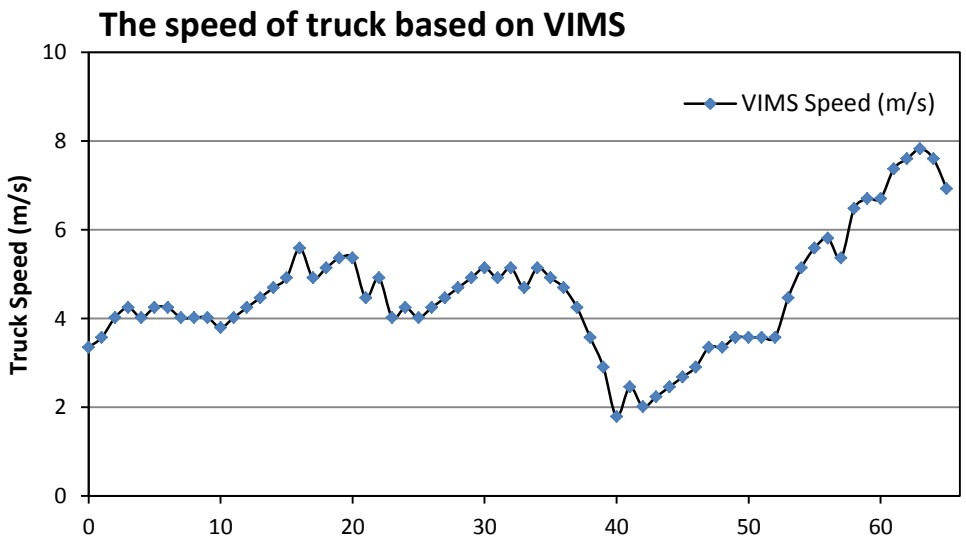

Figure 4.4. Truck speed based on VIMS

We can perform such prediction for multiple points in the VIMS data to measure the distance traveled based on the basic motion equation:

$$\Delta x = \bar{V} \times \Delta t_V \quad (53)$$

where $\bar{V}$ is the average speed during the time $\Delta t_V = t_1 - t_0$. This has been done for a few points and the results are shown in Table 4.1. The first row of the table suggests that at time 31s ($\Delta t_V = 3s$) the truck has traveled 14.9 m from its reference point (which is $t_0 = 28s$ in our case). Based on this calculation we can expect that the truck passes over geophone 22 at time 31s. The number 22 comes from the fact that the geophone 7 was chosen as the reference point and assumed to be in the least drift with the VIMS data. The next step is to explore whether if the trace 22 supports this prediction.

Table 4.1. The distance traveled by truck at different time steps from t_0= 28s

time t_1 (s)	$\Delta t_V(s)$	$\Delta x\ (m)$
31	3	14.9
33	5	24.8
35	7	34.7
37	9	44.0
40	12	53.5
43	15	60.0

3- If we assume that there is no drift the data from VIMS and seismic, the trace 22 must show a peak value overlapping the peak value observed in VIMS. This is plotted in Figure 4.5 to examine this argument.

As can be seen in this plot, the maximum point of the seismic trace does not exactly overlap with the peak at t_1=31 s. The dashed line indicates the time 31s. The seismic trace 22 indicates that the truck passed over that location at time of about 30s while the VIMS prediction suggests that truck must be at geophone 22 at time 31s. This is a clear indication of the time drift between the two time frames. To further demonstrate this drift, we can use the other Δx values in Table 4.1 to make similar predictions and overlay them with the predicted seismic trace. It should be noted again that the Δx values in Table 4.1 are the distance traveled by the truck starting from the reference point. Hence, all these number must be added to the first trace which is 7th geophone to obtain the corresponding geophone number. It is also worth noting that for the case where Δx is not a round number, the closest round number is selected to be able to choose the corresponding trace.

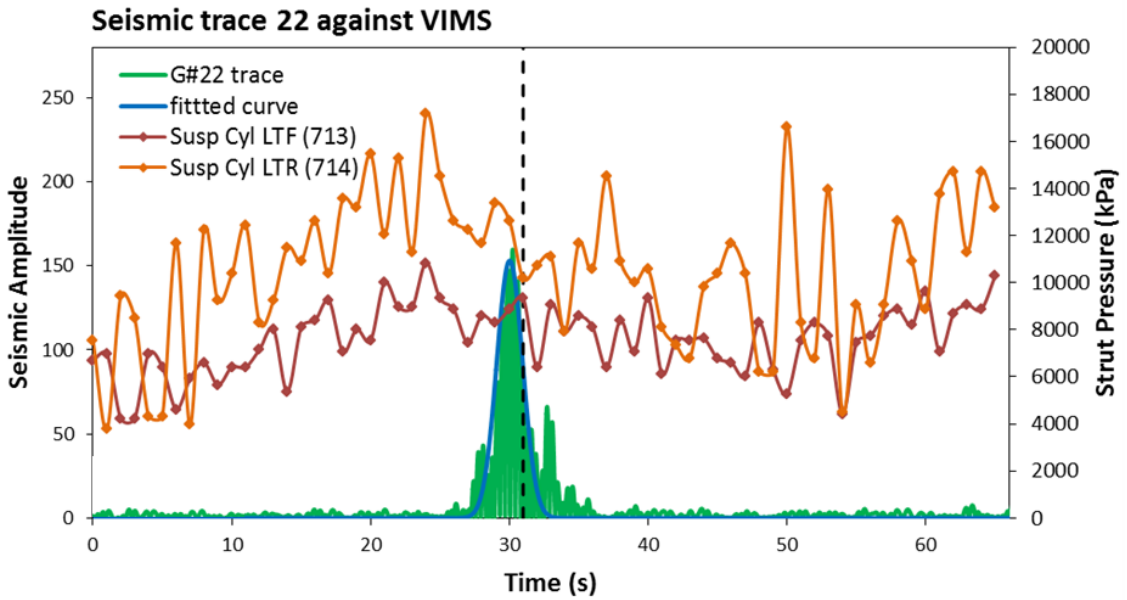

Figure 4.5. Overlaying seismic trace 22 with VIMS

Figures 4.6-9 demonstrate the VIMS data along with the seismic traces corresponding to each Δx value for different time steps in Table 4.1.

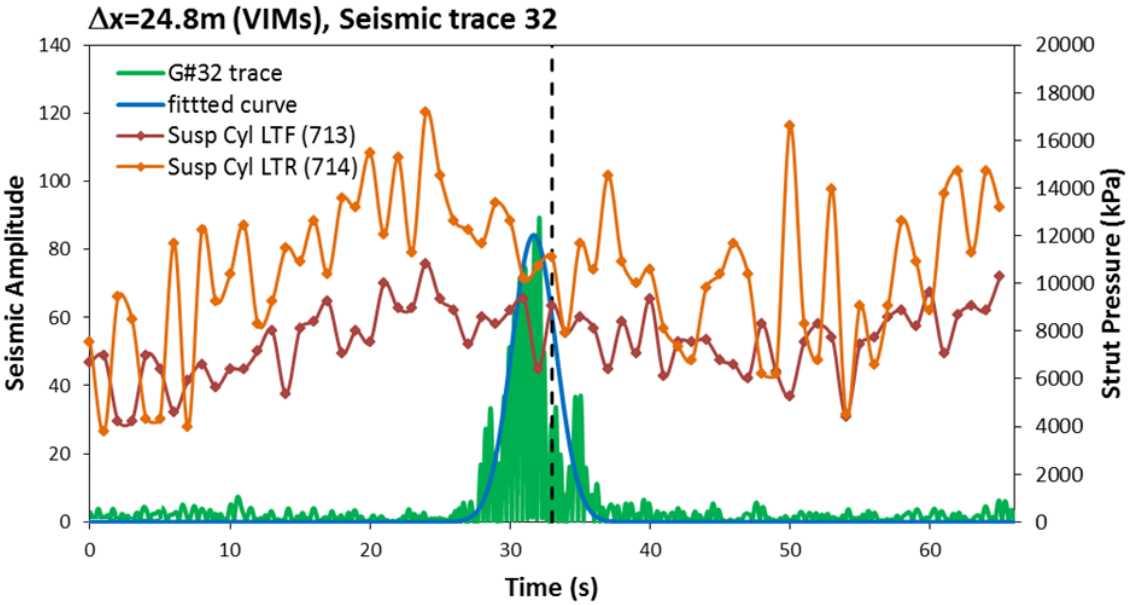

Figure 4.6. Overlaying seismic trace 32 with VIMS

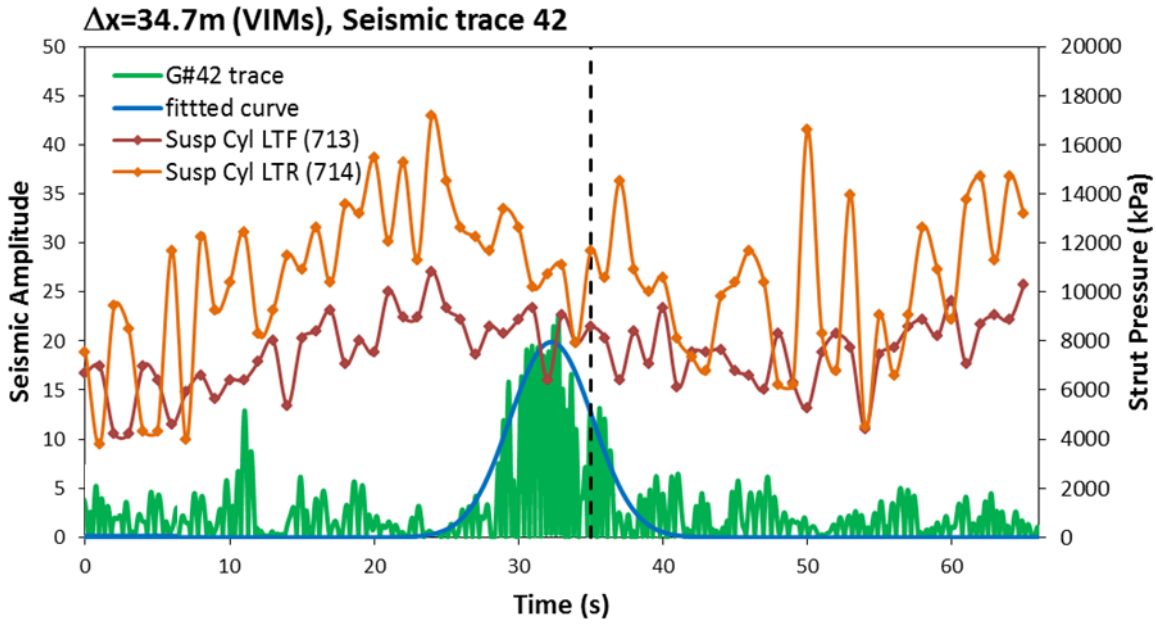

Figure 4.7. Overlaying seismic trace 42 with VIMS

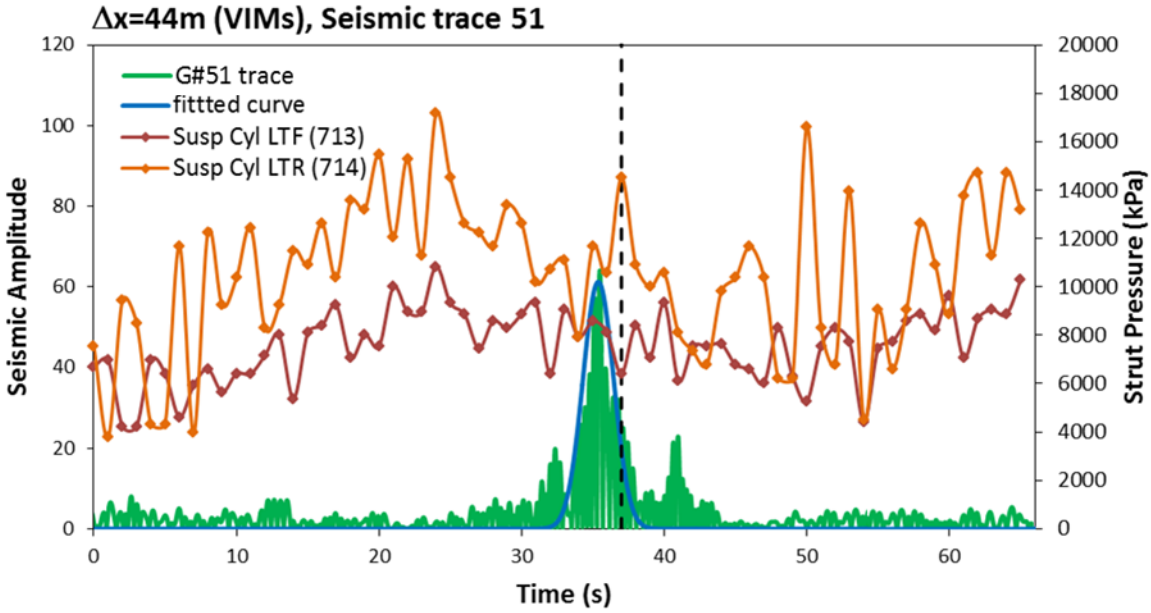

Figure 4.8. Overlaying seismic trace 51 with VIMS

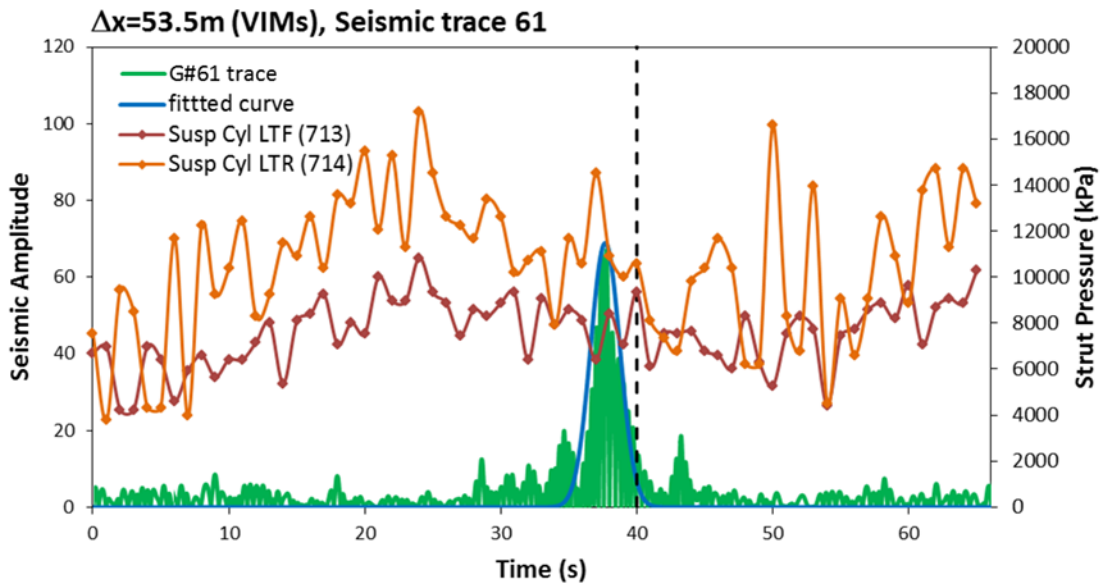

Figure 4.9. Overlaying seismic trace 61 with VIMS

As can be seen in these Figures, the drift seems to increase as the Δt_V increases. In other words, the farther the distance from the reference point, the larger the time difference between the maximum point of the predicted seismic trace and VIMS predicted time.

4- In order to find a correlation between two data series we first explore the actual trace that better matches the peak positions of the VIMS data. For instance, in the first time step, i.e. t_1=31 s, we need to move towards later geophone traces in order to match the maximum point of the seismic with the dashed line which is the predicted time based on VIMS. In the first case, the seismic trace 24 shows a better time matching than the initial trace 22. This is shown in Figure 4.10 where the trace 24 is overlaid on the VIMS data.

As this plot shows, the position of the maximum amplitude point which indicates the most probable location of the truck overlaps with t_1=31s. Based on our previous calculation on VIMS truck speed and time, the truck should be close to geophone 22. However, the maximum point of trace 22 does not overlap with this time.

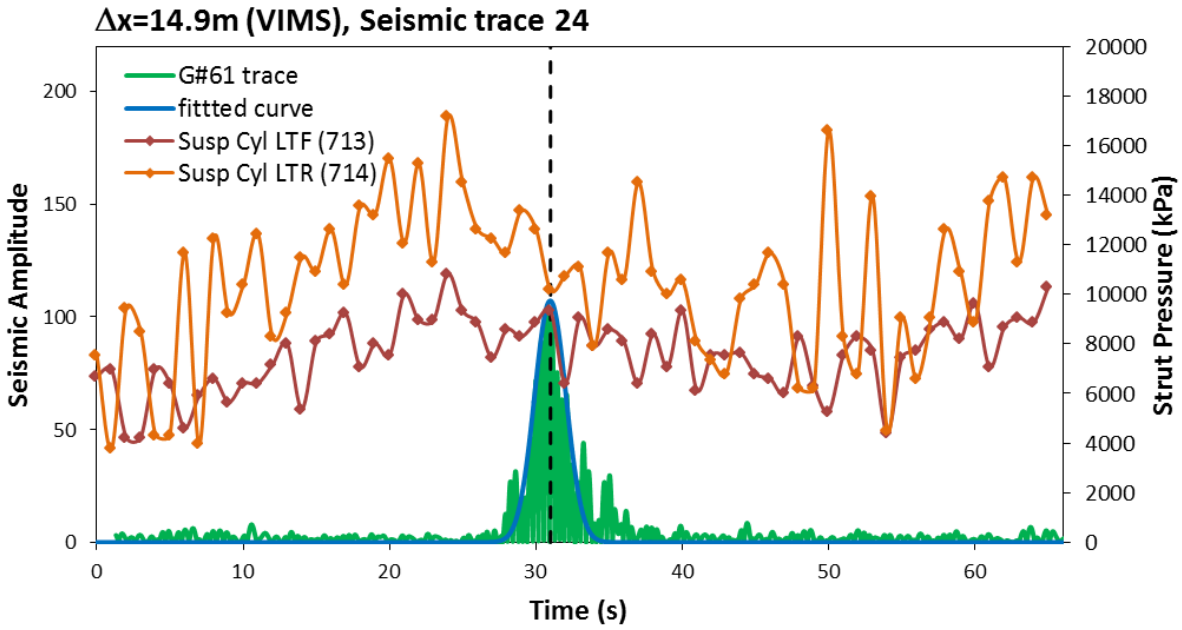

Figure 4.10. Overlaying seismic trace 24 with VIMS

In this case, the actual distance traveled by truck based on the seismic is Δx_s=24-7=17 m. Here, Δx_s is the distance traveled by truck to reach to the time 31s. Using the average truck speed from the VIMS data we can back calculate the $\Delta t_s=\Delta x_s/\bar{V}$. In other words, the average time taken by the truck to travel the distance of Δx_s can be calculated based on its average speed. In the case where there is not any drift between the two data series, the quantities Δt_V (from the second step) and Δt_s as well as Δx values should be equal. However, the differences between these values are caused by the drift.

Table 4.2. The Δt and Δt_s values for the selected peak points

Δt_s (s)	Δt_V (s)
0	0
3.46	3
5.64	5
7.68	7
9.76	9
12.87	12
15.91981132	15

We can perform similar calculations for all the selected peak points and obtain Δt_s values for each point in Table 4.1. Table 4.2 shows the initial Δt_V values and the new Δt_s for each point. We can now draw the values for Δt_s against their corresponding Δt_V values to explore if they follow a trend. Figure 4.11 is a plot of Δt_s vs. Δt_V that shows there is linear relationship between the two.

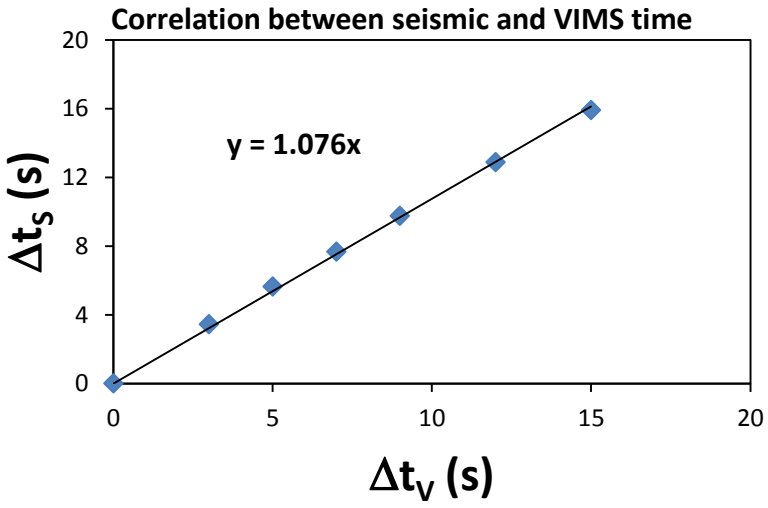

Figure 4.11. The relationship between Δt_s vs. Δt_V

If we multiply the VIMS change in time by the constant 1.076, we can expect that the data series from seismic and VIMS have the lowest drift during the time frame of the seismic analysis. This can be tested in the same manner of obtaining the Δx values from VIMS and trying to match the corresponding seismic trace following the second step. Again, trace 7 seems to be the first trace that lies exactly of top of a VIMS data point and hence, is taken as the reference point. The t_0 values in the modified time scale is 22.98 s. Using this reference point we calculate the distance traveled based on VIMS for the t_1= 39.81 s. The selection of this point is because the farthest point from the reference having the largest drift. The Δx in this case is 57 m which corresponds to the trace 57+7 or 64. Figure 4.12 shows the trace 64 and the VIMs data and as it can be seen, the extent of the drift has been relatively decreased.

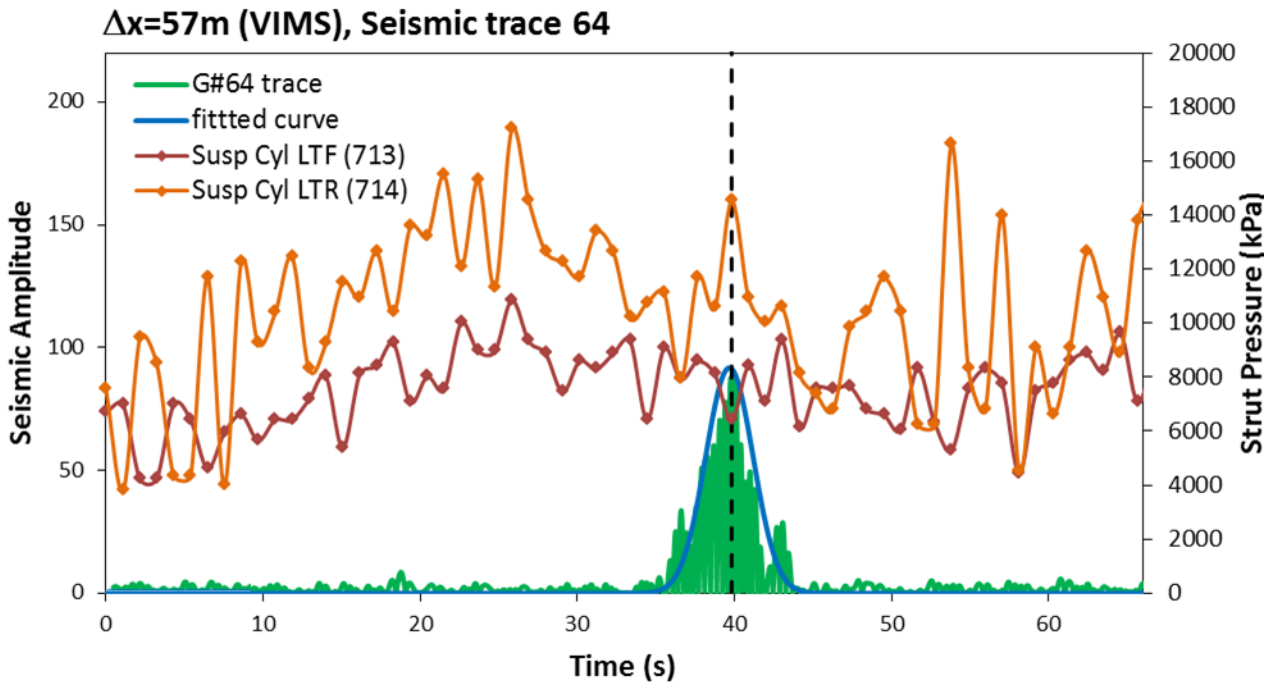

Figure 4.12. Overlaying seismic trace 64 with modified VIMS time

4.2. Confirming the drift correction

In the previous section, an empirical method for minimizing the amount of drift in time scale of two data series from VIMS and seismic was developed. Although the method showed promising results after being applied to the VIMS data and plotted against the seismic data, further confirmation with another method could still be advantageous. For this purpose, we can examine the variation in the forces detected by the truck struts and seek for similar trend in the seismic data. A simple assumption in this case is that the magnitude of ground particle movements follows the amount of force/pressure exerted by the truck tries. For instance, we can expect that when the truck strut pressure decreases, there is less motion in ground particle as the result. The key question here would be how to measure the motion of ground underneath the tires.

As mentioned in the chapter describing the geophone mechanism, the configuration of the geophone is designed in such a way that any infinitesimal motion from the ground particle is transformed into a motion and then voltage in the geophone. In other words, the geophone records the motion of particles surrounding it in the ground. It was also explained that the

voltage output of the geophone is proportional to the particle velocity. Hence, we can expect that applying higher force to the ground could result in larger motions in the ground particle. The magnitude of the geophone output will then be a function of the applied pressure. Finding the actual relationship between these parameters is not the purpose of this chapter. However, the trend of variation of the geophone signal magnitude with time must follow the trend in the pressure struts.

To measure the magnitude of geophone signal the best way would be to calculate the area underneath its peak. This can be done through fitting a simple Gaussian function as seen in the previous section and integrating the function. The important parameter to consider for this integration is the time interval selection. This is related to the time interval during which truck is passing over a geophone. We need to consider the distance between the two sets of front and rear tires passing each geophone. For a CAT797 truck, this distance is about 7 meters [47]. The whole length of the truck is about 14 meters. Assuming the truck speed range of 2-4.5 m/s (during the time frame of 27-41s), it could take about 3-7s for the truck to completely pass over the geophone. It should be noted that these values are estimated values and a more applicable time interval could be obtained by examining the length of the peak seismic signal.

Another important factor is the independent effect of each set of tires, either front or rear on the geophone. The ideal case would be to separate the signals from each set in the seismic trace. After thorough examination of each trace, it was found out that the separation process is extremely difficult. In fact, in most of cases a single peak is observed. The length of the peak is normally over 3s which indicates that the signals from both rear and front tire are included in the peak signal. Hence, for better correlation of the VIMS force values and the areas underneath seismic peaks, the sum of rear and front tire pressures should be considered. The results of calculations of area underneath the peaks for some of the geophone traces are shown in Figure 4.13. The plot also shows that the sum of forces for the front and rear tires in the time frame of truck traveling through the geophone arrays which is between 27-41s. It is worth mentioning that the pressures of for each set of tires have been averaged for each set. For instance, before the summing process, the pressures of all rear tires have been averaged and then added to the average pressures of the front tires.

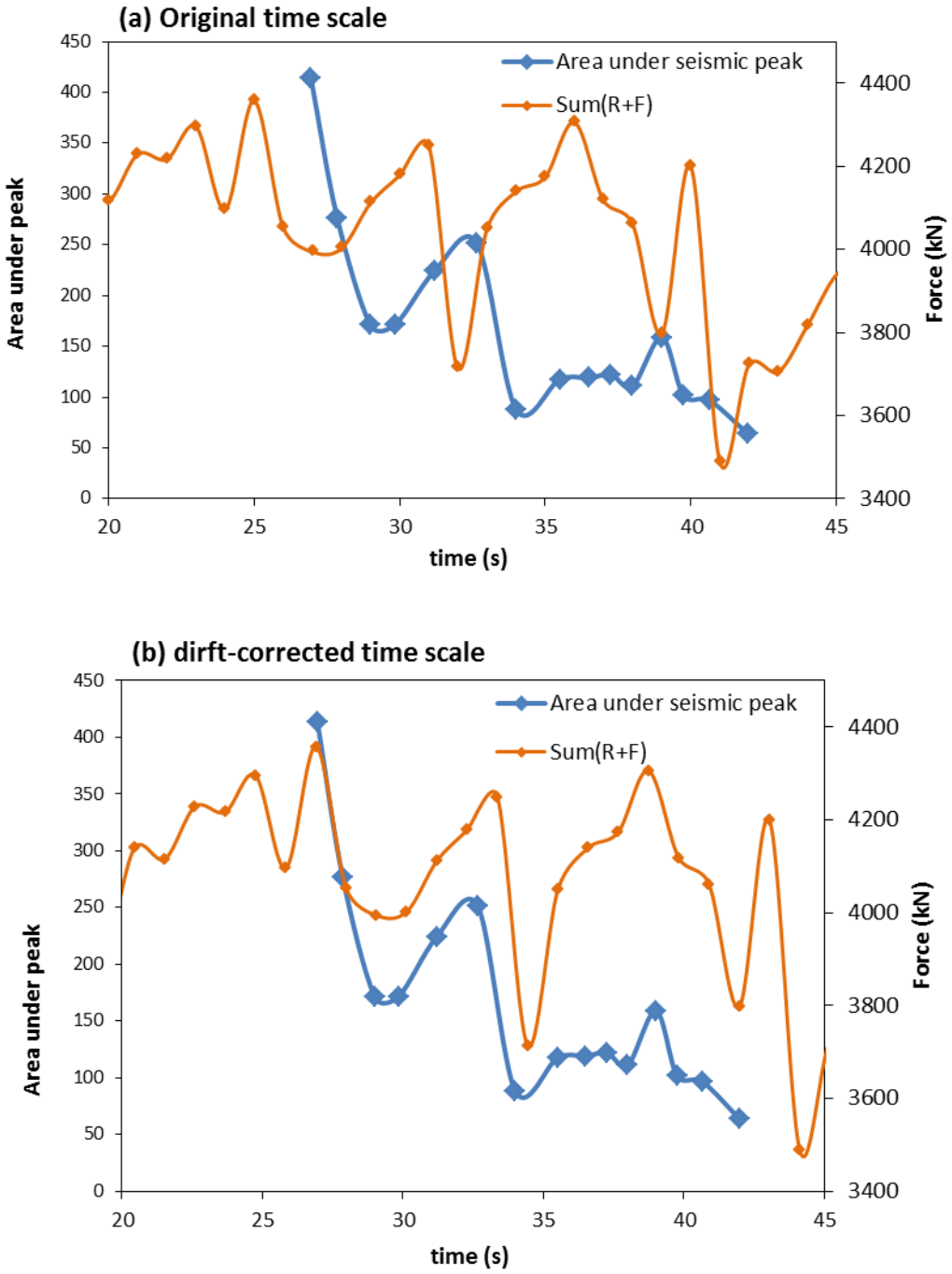

Figure 4.13. Force of rear+front tires vs. area under peak in (a) original time scale and (b) drift corrected time scale

The comparison between these two plots confirms the effectiveness of the drift correction methods. As can be seen in Figure 4.13(b), the magnitude of area underneath selected peaks in

seismic traces follows similar trend to that of the average forces from the tires. We can further utilise this results towards obtaining some key ground parameters through proper extraction of data from the geophone signal. This is the subject of the last chapter where the results of seismic analysis methods and the VIMS data will be compared to obtain some correlations between these two methods.

Chapter 5

5. Surface wave methods for predicting ground properties

5.1. Ground stiffness from Rayleigh waves

5.1.1. Theoretical background

The use of seismic analysis to estimate the material properties of the ground such as bulk modulus, shear modulus or stiffness has been the subject of many research and practical works in the past few decades. Originally, these methods were used as complimentary tests to conventional laboratory tests on soil samples. Compared to conventional test methods, seismic approaches have the advantage of in-situ measurements that are independent of the sample size, disturbance and unrepresentative sampling [38]. The testing methods can be divided into two major categories which depend on the configuration of the equipment being subsurface and surface methods. In the subsurface method, the main requirement is to prepare boreholes in order to receive incoming waves at a certain depth from the ground [39]. Such conditions are not necessary for surface methods since sensors are placed on the surface of the ground. In general, the velocity of the generated waves depends on the properties of the ground through which it travels. While in the case of subsurface methods, the P- and S-wave velocities are measured, the surface methods mainly rely on the velocity of surface waves such as Rayleigh waves [42, 61]. In this section, the results of an analysis on a selected passive seismic run for truck motion of oil sand are presented. As previously mentioned, an array of 72 geophones with spacing of 1 m was placed on an oil sand haul road. Due to this configuration, the analysis was based on a surface rather than a subsurface method. In the following paragraphs, the method principle to determine a ground shear modulus from seismic data is provided. Later, the method will be applied to stationary envelopes of data filtered at different conditions to obtain a conclusive comparison.

It is necessary to understand the basic rules governing seismic analysis of surface waves. Here, a brief explanation of step-by-step method to obtain ground shear modulus using surface waves is provided. It is usually assumed that the magnitude strain in due to the presence of seismic waves is very small [61]. The behavior of most of soils varies non-linearly with strain. At very small strain values (<0.001%) the ground is expected to behave elastically and hence a

constant stiffness may be achieved. At higher strain levels, the stiffness decreases as a function of strain and eventually reaches a plateau dominated by the plastic behavior of the ground. The stiffness obtained from a seismic analysis would hence provide an upper limit for ground stiffness due to the small strain values. In most of the seismic methods, the wave source is a hammer or wave generator. Similar to any other type of source, both body waves and surface waves are generated. The two major components of body waves are P- and S-waves which propagate into the ground. The surface waves move along the surface in a manner described by Rayleigh [40, 62]. In fact, more than 75% of the source energy propagates in the form of Rayleigh waves along the surface [39, 61]. Many geophysical measurements used to treat Rayleigh waves as noise or ground roll signals. However, it was realized that these waves travel at a velocity proportional to the stiffness of the ground and hence, it is now used as strong indicator to measure the properties of the ground near the surface [41]. It is believed that the shear strain caused by Rayleigh waves is in the order of 0.001% which makes it a suitable candidate to measure stiffness [61, 63]. It is also reported that Rayleigh waves extend only to a depth equal to their wavelength and diminish thereafter. Hence, ground properties directly affect the velocity of the Rayleigh wave propagating away from the source. The following section briefly reviews the steps to obtain the shear modulus from Rayleigh waves following the method introduced by Matthews et. al [63, 64].

5.1.1.1. Surface wave method

The determination of Rayleigh wave velocity which in turn results in calculating shear modulus has been reported by many authors over the past few decades. Matthews et al. [63] presented a systematic approach to obtain shear modulus based on all previous works. In principle, the method requires a wave source with the capability of generating a signal at specific frequency and specially low frequencies for higher penetration. The signal could be generated by either an impact source such as a hammer or a continuous wave source like a wave generator. The former is used in method known as spectral analysis of surface waves (SASW) developed by Strokoe and Nazarian [65-67]. The latter is used in continuous surface wave (CSW) methods [68]. In both case a series of geophones located at known distance from the source are used to collect the signals. The use of the impact source has the disadvantage of limited control the range of frequencies generated by the source. In a typical surface wave method, a frequency range of 3 to 200 Hz might be covered to create a complete dispersion curve of shear modulus vs. depth

[63]. The lower frequencies give information from the deeper points in the ground due to their larger wavelength. Once a signal at a certain frequency is generated by a vibrator, the geophone response is recorded as the amplitude vs. time. The signal received by each geophone is then transformed into the frequency domain using the Fourier transform method. From the frequency response, one can deduce the phase angle of the frequency amplitude at any frequency. In surface wave methods, this would be the angle of the signal at the frequency generated by the source. Mathematically, any point in the frequency domain is complex number in the form of $a \pm bi$ where $i = \sqrt{-1}$. The angle of the signal at any frequency would be $\tan^{-1} {}^{b}/_{a}$. For two geophones at a distance d from each other, the phase angle difference ($\Delta\phi$) at a particular frequency can then be measured. From the phase difference and the spacing between the geophones, one can obtain the Rayleigh wavelength using the following equation [63]:

$$\lambda = \frac{2\pi d}{\Delta\phi} \quad (54)$$

The velocity of the Rayleigh wave can be obtained by the following formula:

$$V_R = f\lambda \quad (55)$$

where *f* is the source frequency.

By generating signals at different frequencies one can create a plot of wavelength vs. phase velocity or what is known as a dispersion curve. Figure 5.1 shows a schematic representation of the surface wave process method for a continuous wave source based on the work of Matthews et al. [63] . As can be seen, the slope of the plot of $\Delta\varphi$ vs. distance from source gives a parameter of ${}^{2\pi}/_{\lambda}$. Adding a number of geophones can enhance the accuracy of the fit and results in a more reliable velocity. However, adding more geophones at the distances farther away from the source might not be beneficial as the Rayleigh wave amplitude weakens with distance.

Once Rayleigh wave velocity is obtained, it can be converted to estimate a shear modulus of the ground using the some basic equations governing wave motion in elastic media. According to Timoshenko and Goodier [36], when a wave travels within the surface of an elastic body, it produces two types of wave of the surface as well as those that travel into the body. The former type is the Rayleigh wave while the latter are the S- and P- waves that are so called waves of distortion and dilatation. A final elastic estimate solution becomes a single equation in terms of υ, Poisson ratio and α which is the following definition:

$$V_R/V_s = \alpha \quad (56)$$

Where V_R is Rayleigh wave velocity and V_S is shear wave velocity.

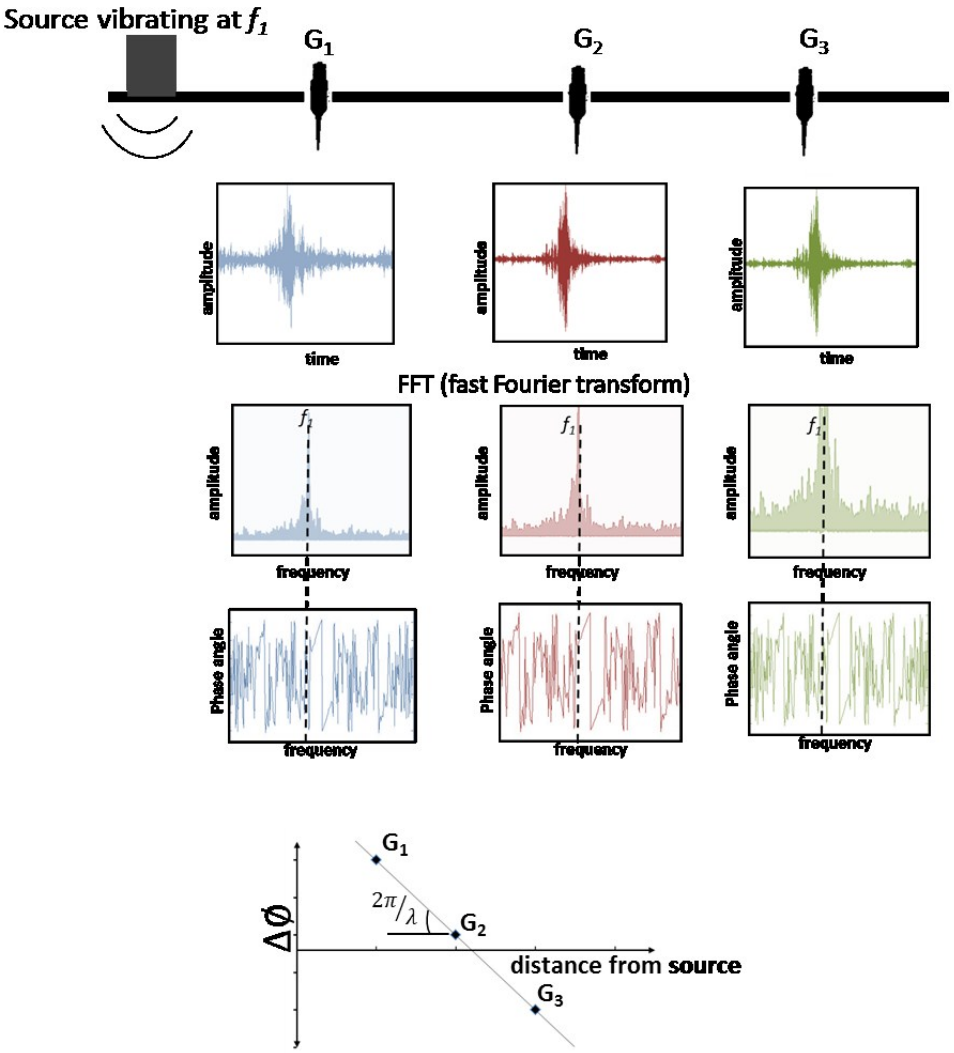

Figure 5.1. Schematic of the surface wave method using a continuous wave source (CSW) (adapted from [63])

The equation to solve for α is:

$$\alpha^6 - 8\alpha^4 + 8\left(3 - \frac{1-2\nu}{1-\upsilon}\right)\alpha^2 - 16\left(1 - \frac{1-2\nu}{2(1-\upsilon)}\right) = 0 \quad (57)$$

In Eq. 57, two parameters are involved. In order to solve the equation, one needs to assume certain values for Poisson ratios and then solve the equation to obtain α. For given Poisson ratios:

$$\upsilon = 0.2, \alpha = 0.911 \quad (58)$$
$$\upsilon = 0.3, \alpha = 0.928$$
$$\upsilon = 0.4, \alpha = 0.942$$
$$\upsilon = 0.5, \alpha = 0.955$$

The α ratio is based on the properties of the ground such that calculations to obtain a shear modulus may be applied:

$$V_s = \sqrt{\frac{G}{\rho}} \quad (59)$$

where ρ is the ground density. Then the shear modulus can be calculated as follows:

$$G = \rho V_s^2 = \rho \left(\frac{V_R}{\alpha}\right)^2 \quad (60)$$

Also, based on the knowledge of mechanical properties of elastic bodies, the shear modulus can be used to estimate a Young's elastic modulus, E via:

$$E = 2G(1 + \nu) = 2\rho(1 + \nu) \left(\frac{V_R}{\alpha}\right)^2 \quad (61)$$

As mentioned above, the use of a surface wave analysing method allows for obtaining a dispersion curve of wave velocity vs. wavelength. The curve can be further analyzed by converting the wavelength to depth and the velocity to shear modulus. The process of converting the wave velocity to modulus was explained above. To obtain a depth profile, the simplest approximation was made based on the fact that a surface energy attenuates as it travels into a body of material. Abbiss [69] and Matthews [63] among many authors showed that the velocity measured by surface wave methods most likely corresponds to a depth of material equal to $z/2$. Using a ratio $\lambda/z = 2$ and performing the above mentioned approach for various frequencies, or wavelengths one can obtain a depth profile.

5.1.2. Analysis of the modulus using a surface wave method

5.1.2.1. Defining stationary envelopes of seismic data

The procedure for obtaining a ground modulus using a surface wave method as described in the previous section requires three major components; a wave source or vibrator, a sensor or geophone and a recorder. An important and intuitive consideration in performing such measurements is that the source has a fixed position and geophones can be placed at different locations on either side of the source. In our case, the position of the source is not fixed. The wave source in our case is the truck motion which travels along an array of 72 geophones with 1 m spacing. The moving nature of the source in our measurement causes the waves received by each geophone to be affected by successive new incoming waves from the truck. The analysis becomes extremely complicated if not impossible when we consider the interference of waves received by geophones throughout the entire array of data. Such complexity requires some simplification before applying surface wave method. The most plausible solution in this case is to split the data into several envelopes of data points. The criteria for creating these subdivisions would be based on the position of the truck. As seen in chapter 4 the truck can be approximately located using the maximum point in the individual geophone trace. The time at which the geophone trace shows a maximum amplitude is the most probable moment that the truck passes that geophone. Since the ultimate goal for our analysis is to establish correlation with the VIMS data, the resolution of the truck on-board systems also plays an important role. The resolution of VIMS is 1 Hz or 1 data point per second. The resolution for seismic traces is 250 Hz. This implies that for any second of measurement we can expect 250 points of the seismic data. Hence, a data range over one second of seismic traces for all geophones was chosen as the criteria to define a the data envelope. In this way, for a specific geophone above which the truck is located, the time frame of one second of the seismic data centered by a maximum amplitude is considered as an effective stationary data envelope. It is assumed that the truck movement during a second of chosen data is negligible and it can be taken as a fixed wave source.

Figure 5.2 graphically shows the process of choosing a data envelope based on maximum amplitude point in a single geophone trace. It is worth mentioning that in order to obtain a more accurate location of the truck and its corresponding time, the filtered data using the first filtering option, i.e. low frequency range is used. A simple Gaussian curve fitting using MATLAB is also employed to the absolute seismic values. This helps better find the maximum intensity point in

the seismic trace. This fitting method will also be utilised to obtain the area underneath the seismic curve which could provide some meaningful information about the ground-tire interaction. This will be further discussed in the next chapter. The plot shows the response of an individual geophone during the seismic measurement. As can be seen in the plot, the maximum amplitude occurs at 27.4 s. This implies that the truck most likely has arrived on the geophone at this time. Hence, the location of the geophone at this moment can be assumed as fixed for the duration of one second. The time frame of one second can be split into two half-second portions before and after the maximum point. The dashed line on the plot indicates the center of time frame. The inset shows the trace in a smaller time frame where the maximum points appear.

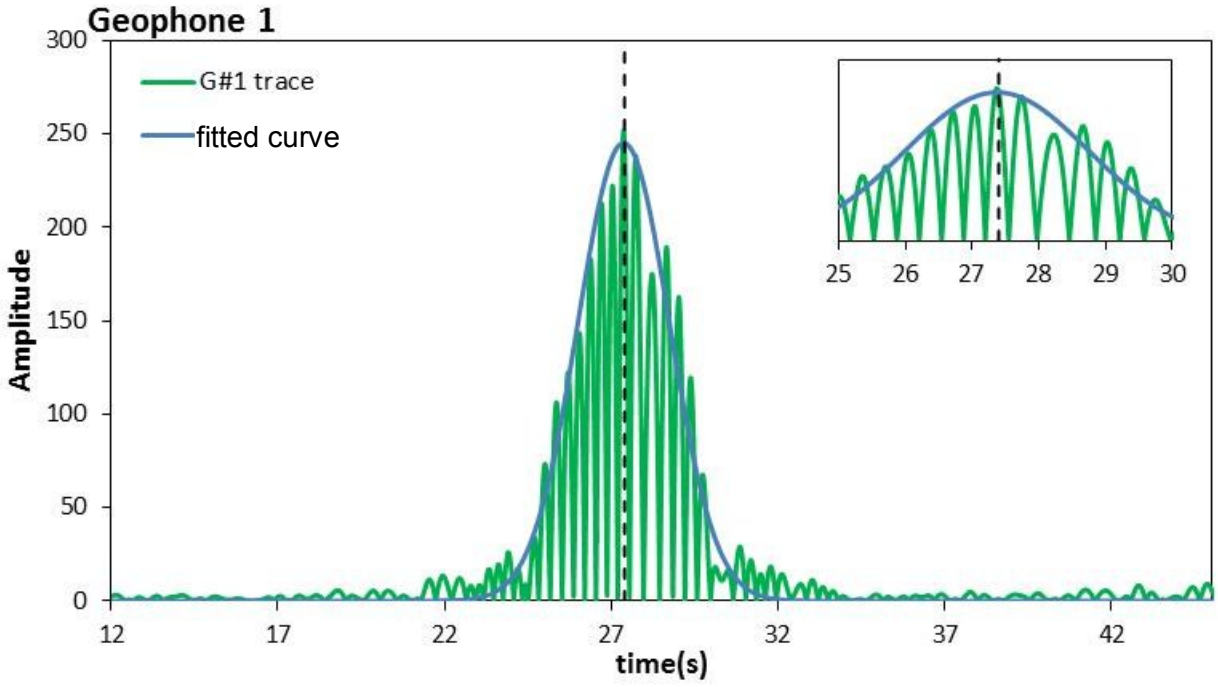

Figure 5.2. Selecting the time range based on the maximum amplitude point at geophone 1

Using the time window shown in Figure 5.2, we now select the seismic data for the entire geophone array. Figure 5.3 demonstrates the wiggle plot for all geophone traces over the duration of the defined one second window. The window originally starts at the time 26.9 s and ends at the time 27.9 s. It is also worth mentioning that no filtering has been applied to the illustrated data show in this plot.

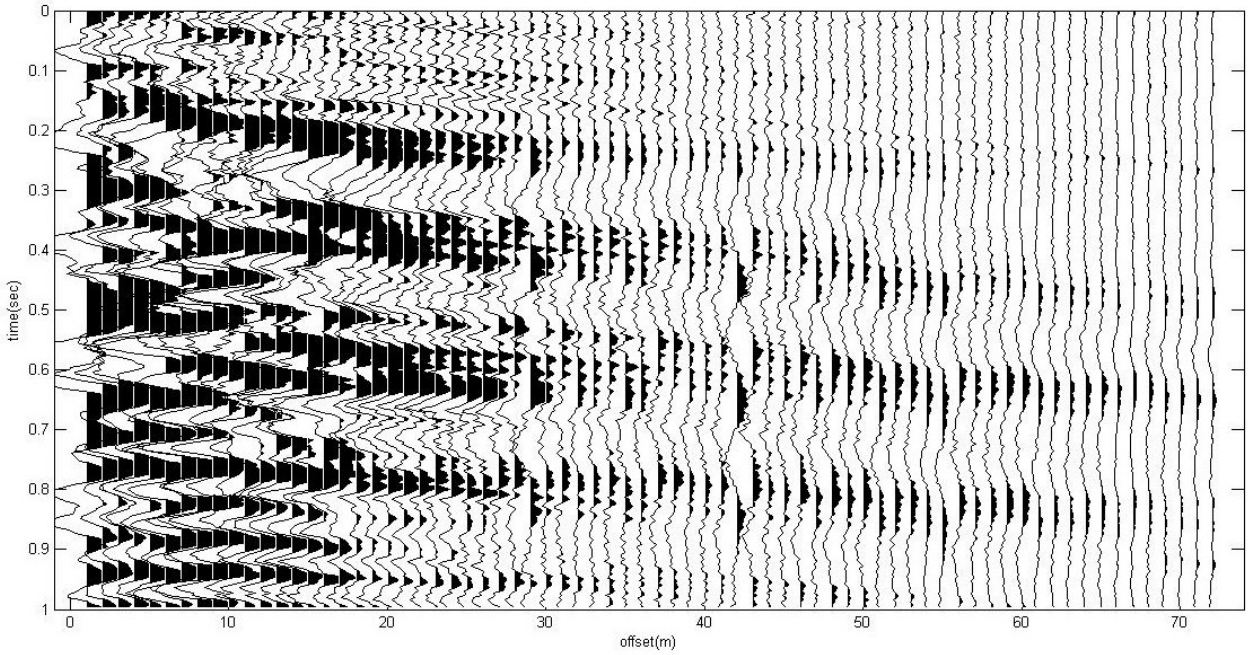

Figure 5.3. A sample envelope of data

As the intensity trend of the waves in Figure 5.3 suggest, the chosen time frame corresponds to the location of truck at the beginning of array at sensor 1. In this case the truck was located above the first geophone in the array. This is the reason for the attenuation of the wave's amplitude towards the end of geophone array. It also indicates the presence of Rayleigh waves for which the amplitude decreases with distance from the source. Figure 5.4 shows the seismic traces in this time frame in the frequency domain. As can be seen in this graph, the envelope has a similar frequency response to the parent data as seen in Figure 2.2. The two major frequency peaks located at 5 Hz and 16 Hz are present. The former corresponds to the motion of truck on the ground and the latter is due to the rotation of tire at of 5 m/s. Some minimal noise trace due to the presence of dozer and shovel with a peak around 7-8 Hz is also present. The noise is minimal in this case due to the choice of a time frame outside the range of the arrival time of the dozer/shovel noise. The noise from the engine movement seems to be reduced but still present to some extent at around 30 Hz. Hence, applying filters using the methods described in chapter 2 is necessary.

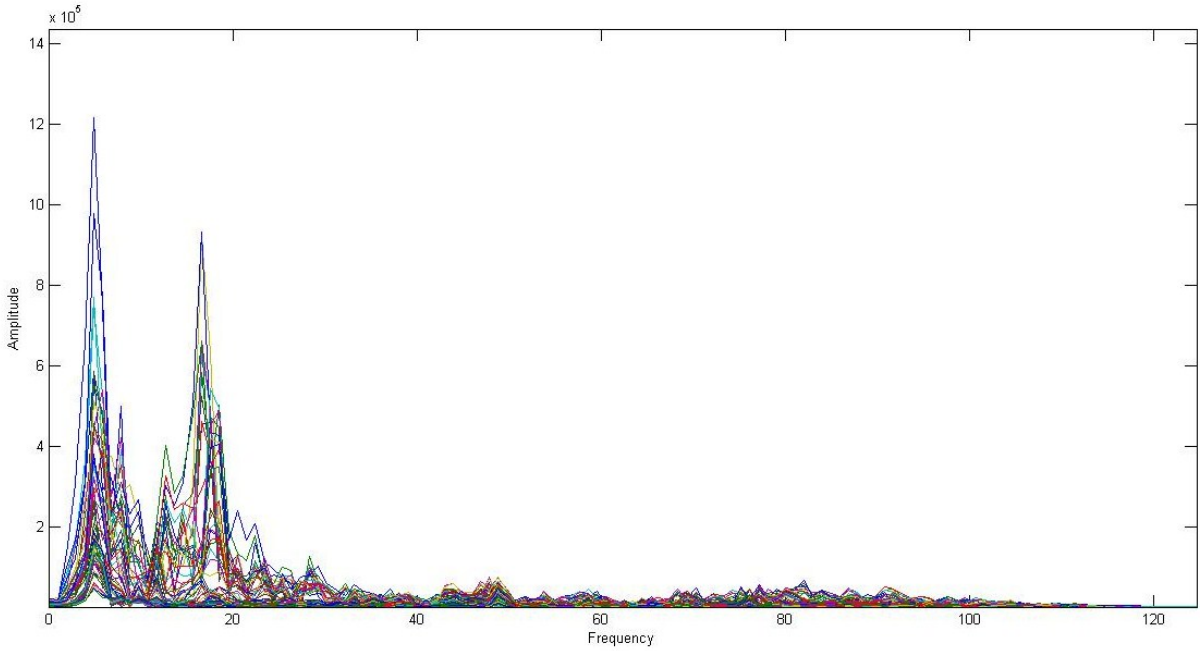

Figure 5.4. Frequency response of the sample data envelope

5.1.2.2. Filtering options

As discussed in the filtering chapter, different types of filter with varying frequency limits can be utilized. A key constituent of noise in data is the presence of the dozer/shovel noise which lies in the range 2 to 8.5 Hz according to the data survey in the frequency domain in chapter 2. Although the noise from the dozer or shovel is present in the frequency response in Figure 5.4, the peaks show some reduced amplitude. As discussed in the filtering chapter 2, this is due to the fact that the signals from dozer and shovel arrival times ~26 to 27 s as well as 41 s which are outside the time frame selected for the envelope. Hence, it is less likely that we see much of the noise from the shovel or dozer in our time frame. This allows for a better view of the effect of truck motion on the ground and its corresponding frequency response without having a nuisance effect from the shovel/dozer. Again, as it was shown in the filtering chapter, the signals up to 5 Hz of frequency do not contain significant noise in the 26-27 s regions. However, there are still some noise signals in this frequency range at 41 s region. Filtering the signals of over 2 Hz frequency seems to clear all noise signals from the seismic trace. In order to clarify whether if the signals within frequency range of 2-8.5 Hz can be used for the seismic analysis, few peak frequencies are chosen in the low frequency range. The rotation of the tire which has a direct

contact with the ground in the frequency range of 10-20 Hz might also provide useful information about the ground stiffness. Hence, combining the effect of truck motion with tire rotation while removing the dozer/shovel noise could be the second filtering option considered in the analysis. Figure 5.5 shows the frequency response of the sample envelope data after applying filtering. Figure 5.5(a) represents a filtering option where only signals with frequency below 20 Hz were selected. As seen in this plot, few major frequencies in the range of 10-20 Hz are observed. However, a closer look at the low frequency range shows that there are few peak frequencies in that range as shown in Figure 5.5 (b). Based on our knowledge in chapter 2, most of these frequencies are created by the dozer/shovel working at a distance from the geophone array. However, it is useful to investigate whether if these frequencies are able to predict the ground stiffness. We also found that the most reliable frequency range is below 2 Hz where then effect of any noise source is removed. It is hence appropriate to filter the data above 2 Hz and observe as shown form Figure 5.6 (a).

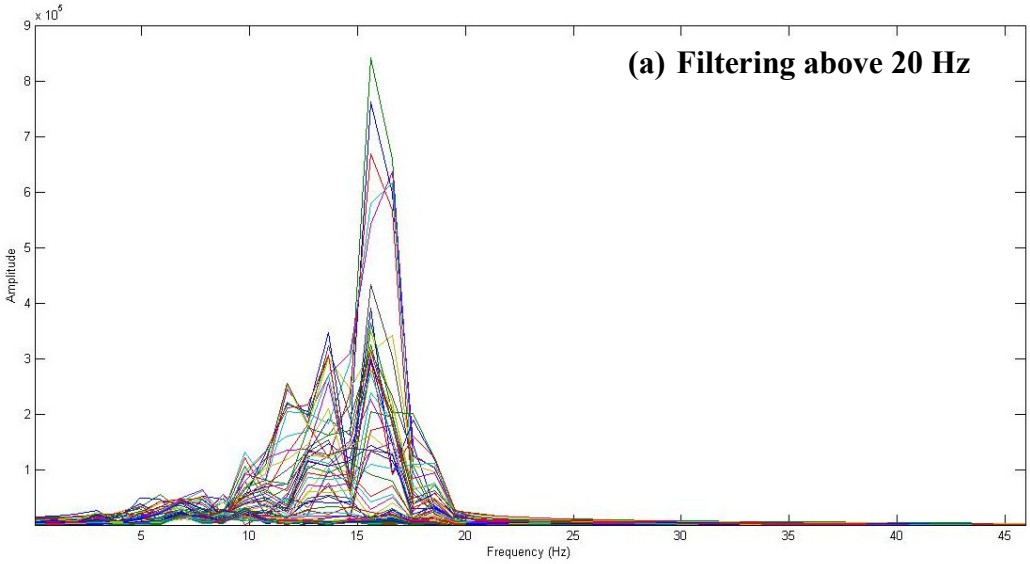

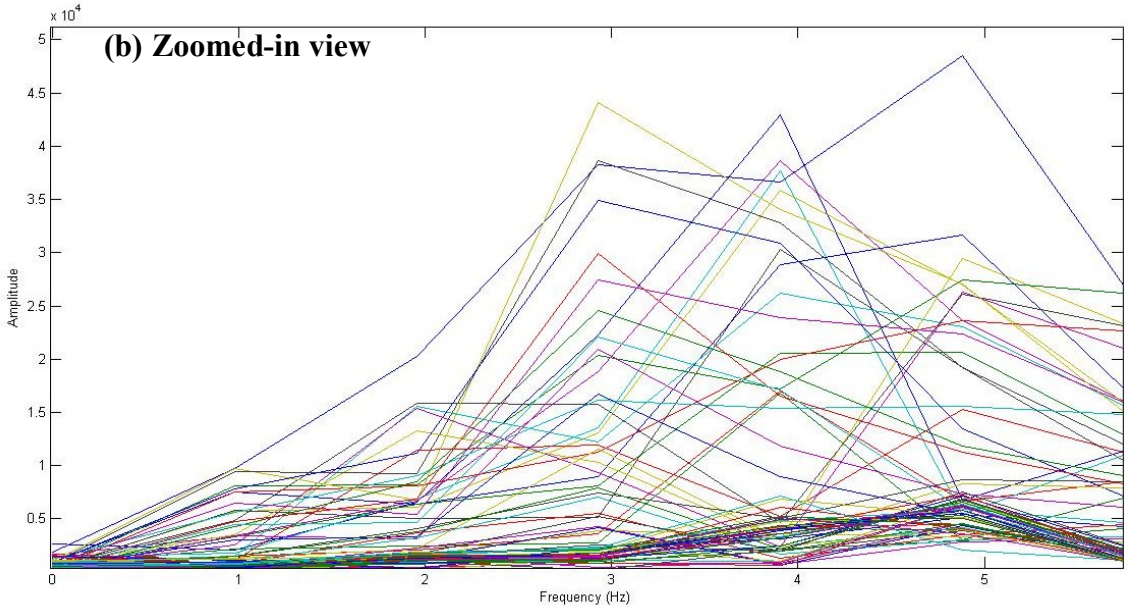

Figure 5.5. Frequency response after applying (a) filtering above 20 Hz and (b) zoomed-in view

The effect of applying the two filtering methods on the appearance of the entire data envelope is shown in the wiggle plots of Figure 5.6.

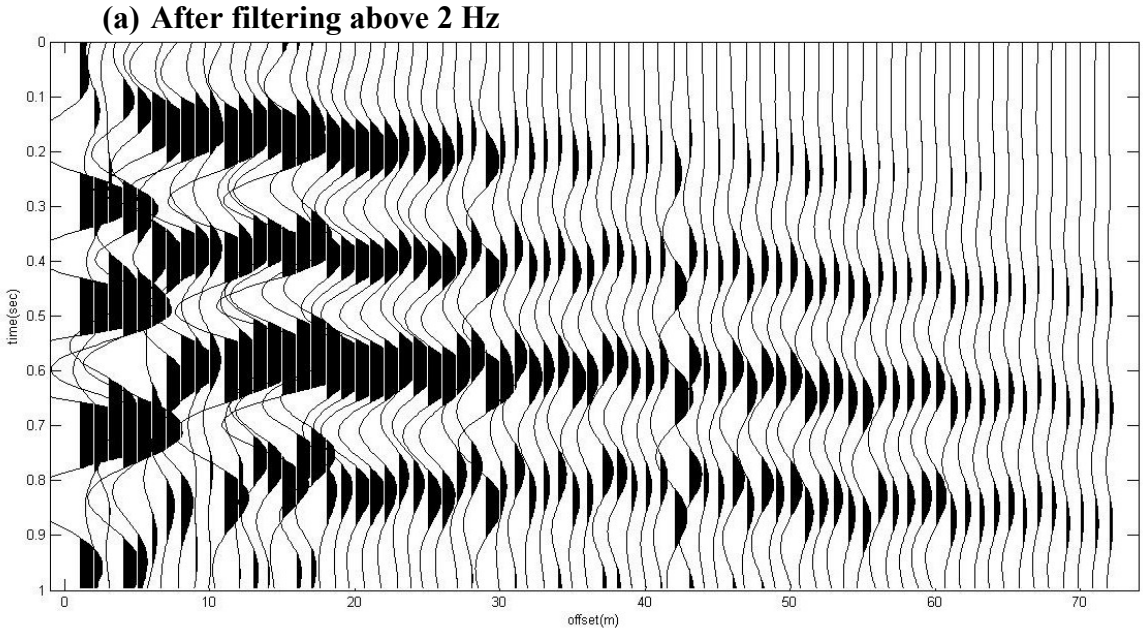

(b) After filtering above 20 Hz

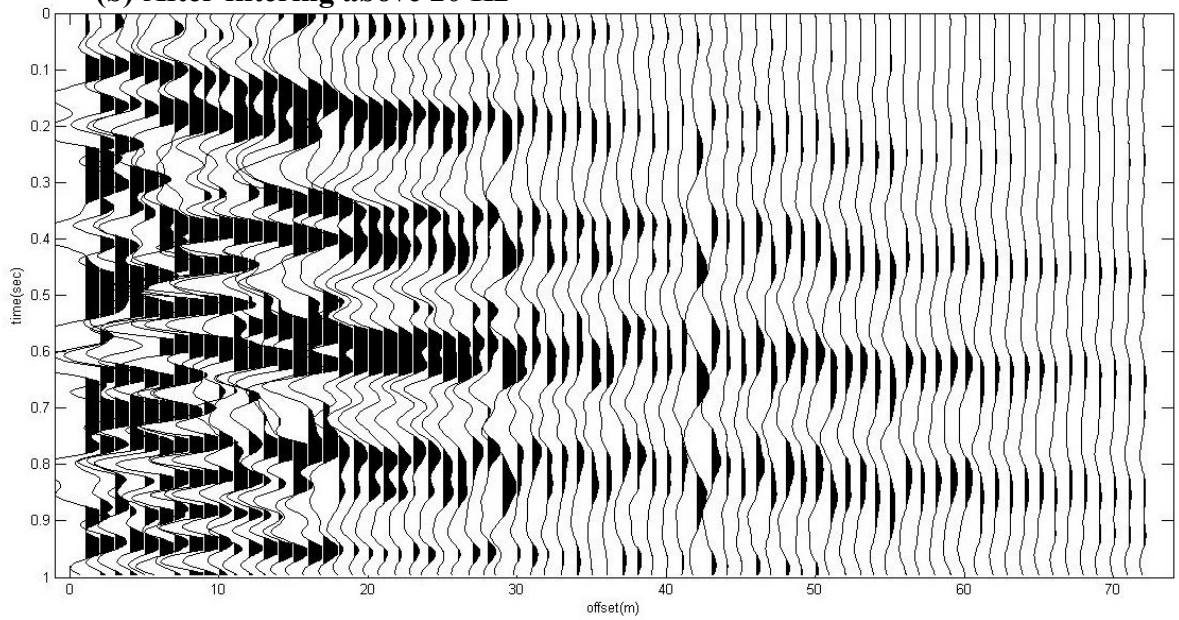

Figure 5.6. Seismic traces after applying (a) filtering above 2 Hz and (b) filtering above 20 Hz

The two data series obtained after applying the above mentioned filtering method can be used as the stationary seismic data that further analyzed by the surface wave method. As mentioned before, the first envelope is obtained based on the truck position over the first geophone. Hence, the position of the source is now considered as geophone 1. Since the spacing between the geophone is one meter, the distance from the source for each geophone is its offset value minus one, i.e. offset-1. We also need to choose a wave with specific frequency. In the case of a conventional surface method, the vibrator generates a single frequency wave. In our case the truck generates a range of frequencies which after filtering contains two major signals. In the most reliable case, we can use the peak frequency at around 1 Hz. Furthermore, we can use a peak frequency from the tire rotation as well as some peak frequencies in the low frequency range. These cases will be examined in the next section to verify the validity of using any peak frequency in determining the ground shear modulus.

5.1.2.3. Phase vs. distance from source

The method of analysing the Rayleigh waves and obtaining the ground modulus is based on using waves with known frequencies. This is in contrast with our seismic measurements where a

range of frequencies are generated by the motion of a truck. Even after filtering implementation, performing the analysis on a single peak frequency would not be conclusive. To test this argument, the values for phase angles at different frequencies below and above the peak frequency are plotted against the distance from the source. In the first case, the data corresponding to the position of the truck over the first geophone is used. The following graphs represent the results of the phase angle vs. the distance from source at frequencies 1, 1.95, 2.93, 3.91, 4.88, and 5.86 Hz. These values are selected based on observation of the frequency peaks in the filtered data shown in Figure 5.5. Figure 5.7(a)-(f) show the plots for the phase angles against distance. The angles are reported in radians and distance in meters. As can be seen in these plots, the gradient (slope) of the phase over distance significantly changes with the frequency. Since the angles have different signs, the plots of the absolute phase angle values vs. distance are also shown in the inset plots. These plots only help better visualize the variation of phase angle with distance. It is worth to note that the sign of the phase angle only changes the sign and not the value of the resulting slope of ϕ vs d. However, the sign of the slope does not affect the final shear modulus value as the Rayleigh wave has a square power in Eq. 60. The plots also show clear singular slopes in some frequencies or impulsive behavior in other frequencies. Such difference in the appearance of the graphs might be due to several factors. A possible explanation can be made based on the fact that the Rayleigh wave generated by the truck has one or a few characteristic frequencies. Not all the examined frequencies in this case are amongst these characteristic values. Hence, some frequencies might result in meaningless shear moduli and trends.

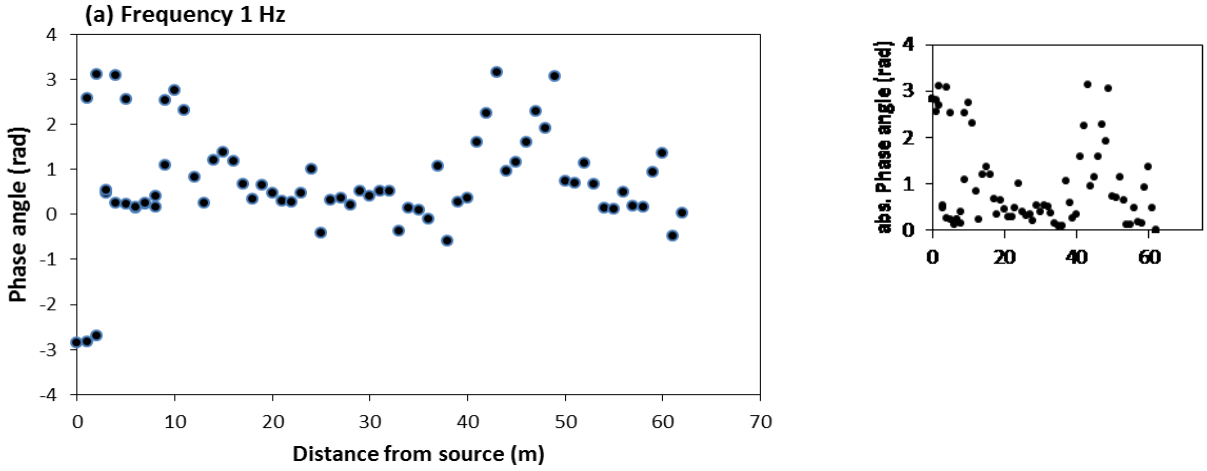

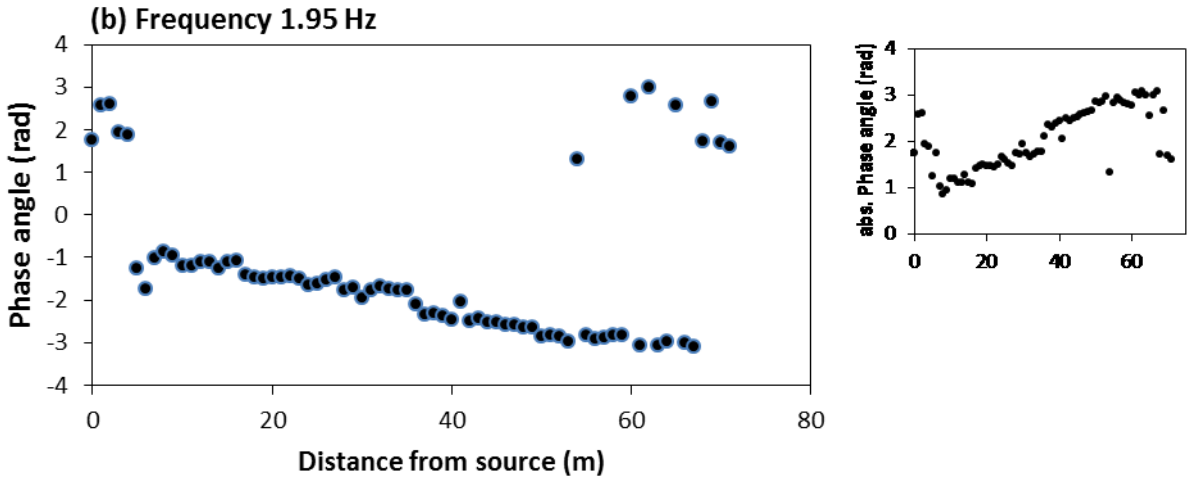
(b) Frequency 1.95 Hz
Phase angle (rad)
Distance from source (m)
abs. Phase angle (rad)

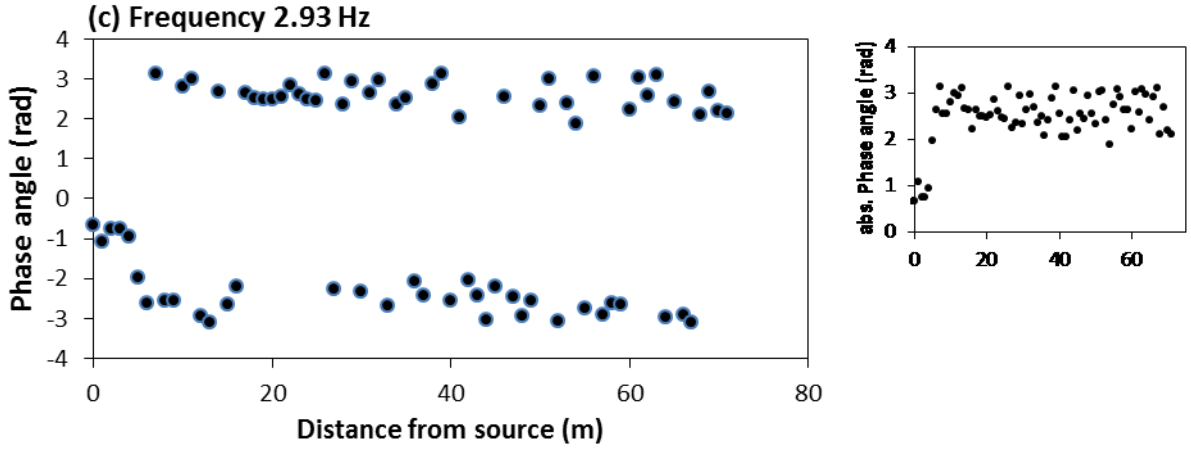
(c) Frequency 2.93 Hz
Phase angle (rad)
Distance from source (m)
abs. Phase angle (rad)

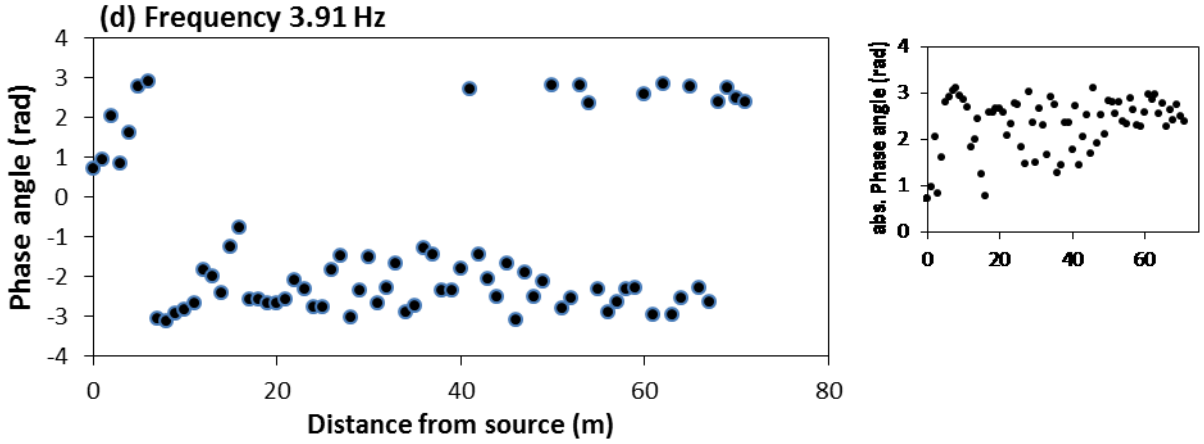
(d) Frequency 3.91 Hz
Phase angle (rad)
Distance from source (m)
abs. Phase angle (rad)

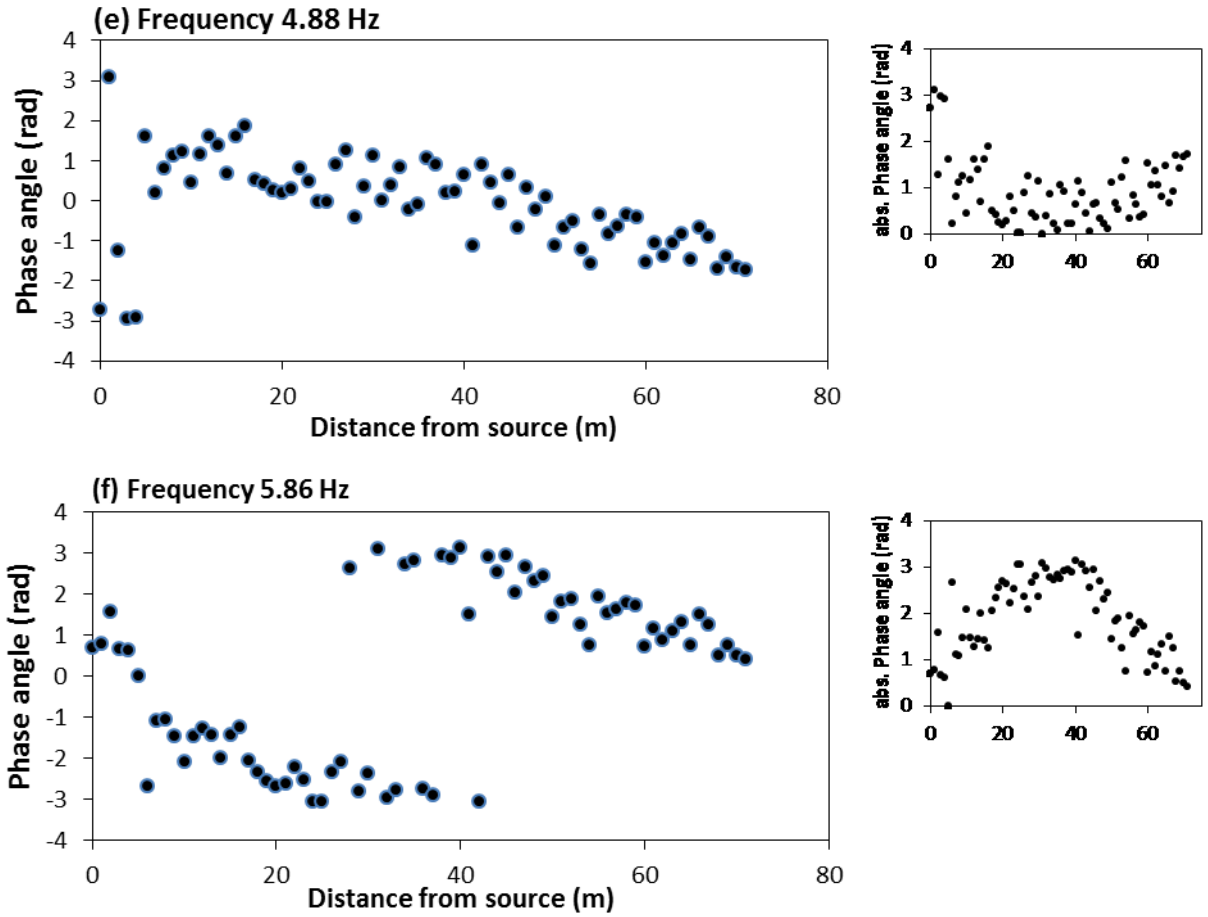

Figure 5.7. Phase vs. distance for different frequencies. Insets show the absolute phase value.

As can be seen in these graphs, it is difficult to draw any conclusion from the phase angle vs. distance plot towards the ground properties. There are also certain challenges when calculating the shear modulus based on Eq. 60. Apart from the proper selection of the frequency, the number of data points for obtaining the slope of the ϕ vs d plot is also important. This will be addressed in the next section.

5.1.2.4. Frequency for calculating shear modulus

To find suitable and meaningful frequency or frequencies, obtaining shear moduli values seem to be the only identification. However, another issue must be resolved before obtaining any modulus value. As mentioned in the theoretical background, the slope of the phase angle vs. distance results in a wavelength which is then used for velocity and modulus calculations. It is essential to identify the number of points in the calculation of the slope. For this step, the results

for a sample frequency which is 1.95 Hz (Fig. 5.7(a)) are selected. Using different numbers of points to calculate a local slope of phase vs. distance, one can observe the variation in the final shear modulus values. Two main assumptions made are the density of the ground and its Poisson ratio. According to Sharifabadi [13, 17], the density varies with the bitumen content of the oil sand as well as with its compactness. A range of density values were reported by the author from 1.7 to 2.1 Mg/m^3. A density value of 2 Mg/m^3 is chosen in our work as the representative density of oil sand. It is also assumed that the density of the oil sand does not change as the truck moves over it. This assumption is not necessarily true as the density of oil sand changes with its compactness. However, in order to account for the variation of the density as the truck travels separate set of experiments needs to be designed and performed. This is beyond the scope of this thesis and a single density will be assumed. The Poisson ratio for oil sand has also been reported by many authors and average value of 0.25 [13]. This results in the α value of about 0.92 to be used in Eq. 60. It is noteworthy that performing a sensitivity study is necessary for the effect of density and Poisson ratio on the shear modulus value. Such study will be performed in a separate section. Figure 5.8 shows the results of the shear modulus calculations according to different number of data points taken for the calculation of the slope, i.e. wavelength.

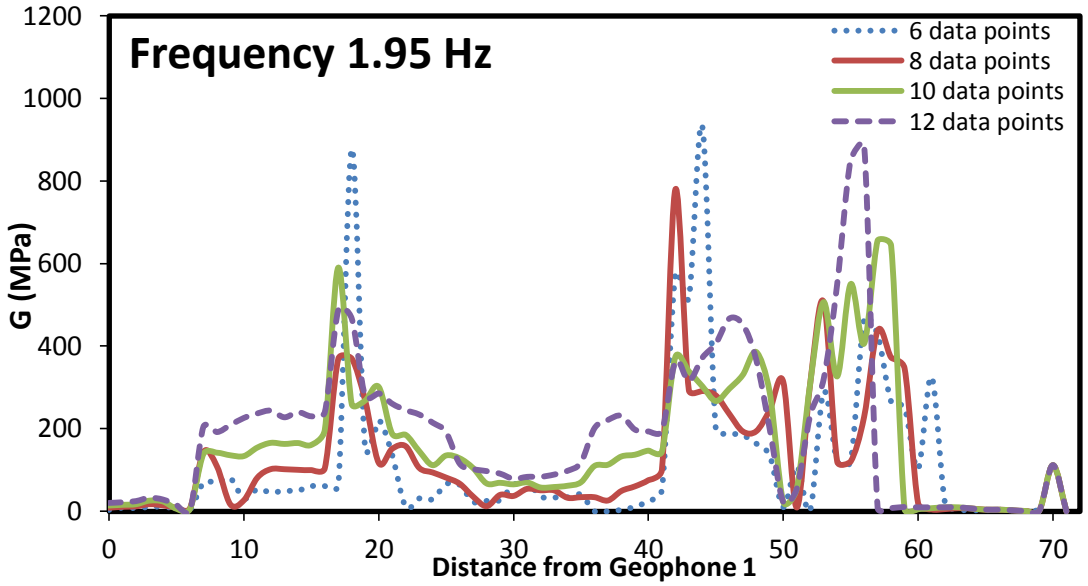

Figure 5.8. Shear modulus calculated based on different number of points

As this graph suggests, taking a lower number of data points, i.e. 6 results in higher modulus values. On the other hand, the 8 and 10 point slopes result in similar values. Large numbers of data points also seems to decrease the resolution. It is therefore concluded that 8 data points will give a reasonable estimate of the variation of the shear modulus vs. distance. In the next section, this number is taken as the general number of point considered in the calculation of any slope.

To observe the influence of the choice of the frequency on the final shear modulus value, several frequencies discussed in previous section are used. Figure 5.9 demonstrates the value of shear modulus calculated based on the slope of phase against geophone number at different frequencies. It should be noted that for the sake of simplicity, the distance from source has been converted to the geophone number.

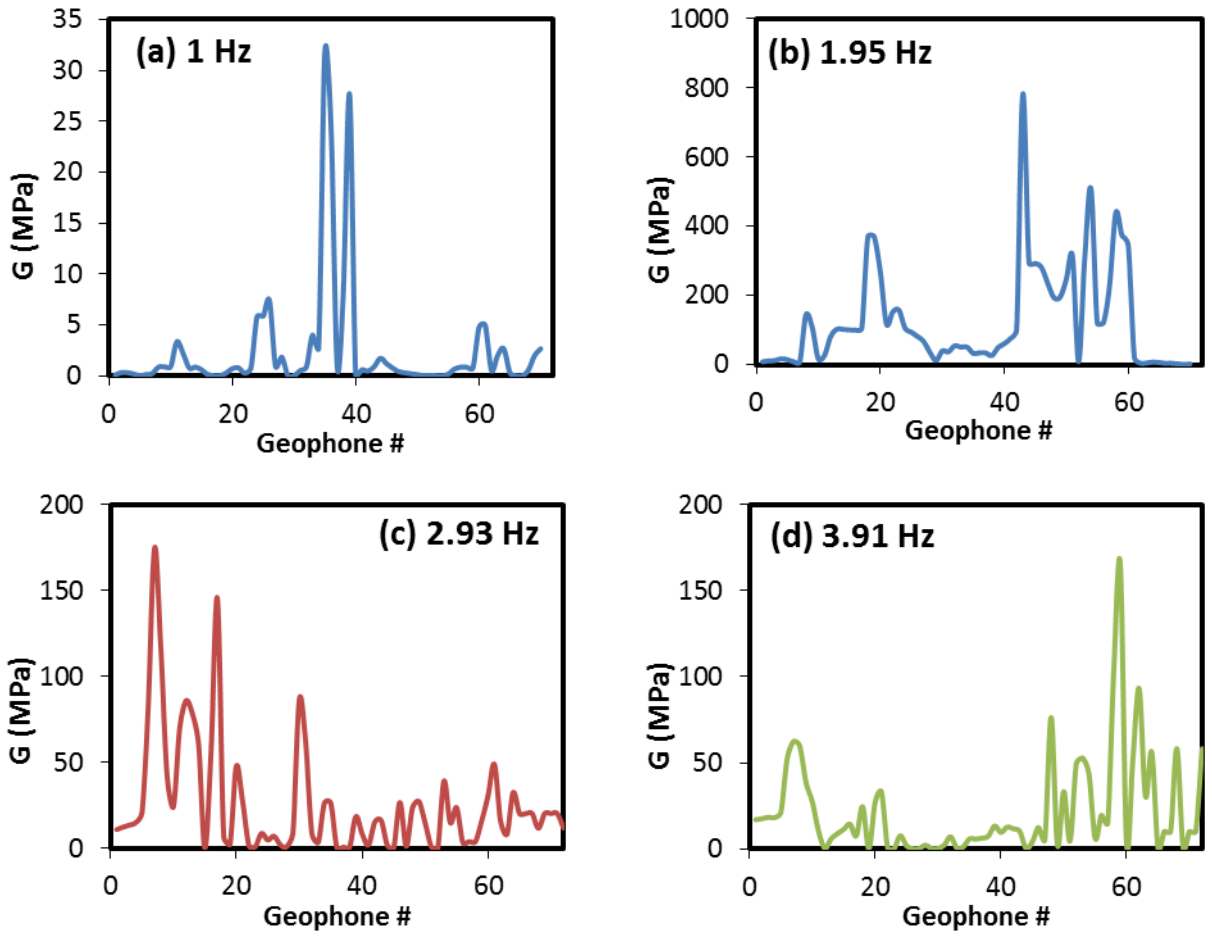

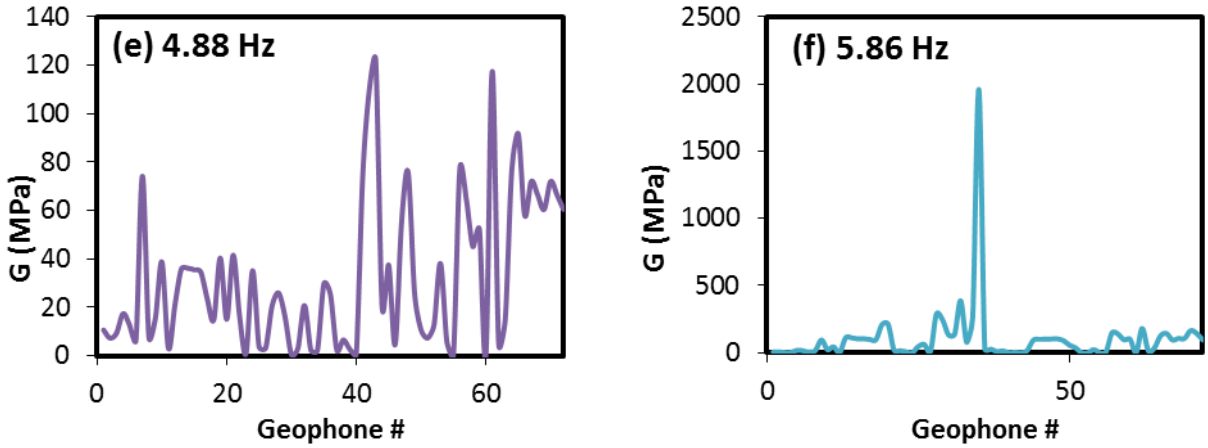

Figure 5.9. Shear modulus calculated for different low frequencies

As these plots show, using different frequency values results in a different shear modulus profile. This confirms the importance of the choice of frequency. A closer look at the shear modulus values of each frequency indicates that a large variation in the values is observed. Overall, three ranges of shear modulus values are observed in these results. The lowest and most indicative frequency, 1 Hz shows shear moduli up to 30 MPa. The frequencies 2.93, 3.91, and 4.88 Hz show shear moduli up to 160 MPa. Higher moduli values up to 800 and 2000 MPa are observed for the frequencies 1.95 and 5.86 Hz, respectively. A comparison of these values with those obtained by Shraifabadi [45] for similar oil sand materials suggests that 1.95 and 5.86 Hz calculations definitely overestimate shear moduli. In their study, a range of 37 to 136 MPa was reported by Sharifabadi [45] . The shear moduli based on 2.93, 3.91 and 4.88 Hz agree with the values for the deepest region of Sharifabadi's study. On the other hand, 1 Hz frequency seems to predict the shear moduli in accord with the near-surface region of oil sand in Sharifabadi's study [45]. Furthermore, another observation is in the trend of shear moduli vs geophone number for these three frequencies. The frequencies in the range of 1.95-4.88 Hz results in higher moduli values in the beginning and end of the geophone array. An opposite trend is observed for 1 Hz where the middle of the array seems to have higher moduli. From the observations above, it can be concluded that the shear moduli obtained using 1 Hz frequency is the most reliable in the low frequency range. The shear moduli value agrees well with the data obtained for near-surface low stiffness oil sand. Moreover, based on Matthews et al. [63] and Eq. 55, one expects that even lower moduli are obtained when using higher than 1 Hz frequency for calculating values. This is due to the fact that higher frequencies provide information from regions closer to the surface

which is known to be loose for oil sand. Hence, the values obtained from the higher frequency range seem to be invalid in this case.

The magnitude of the ground moduli can also be calculated based on the higher frequency values in the range of 10-20 Hz. This can be performed on the data filtered <20 Hz filtering (Fig. 5.5(b)). As seen in Fig. 5.5 (b), three main frequency peaks are observed in this range being 9.76, 12.7 and 16.6 Hz. Figure 5.10 shows the plots of shear moduli obtained using these three frequencies.

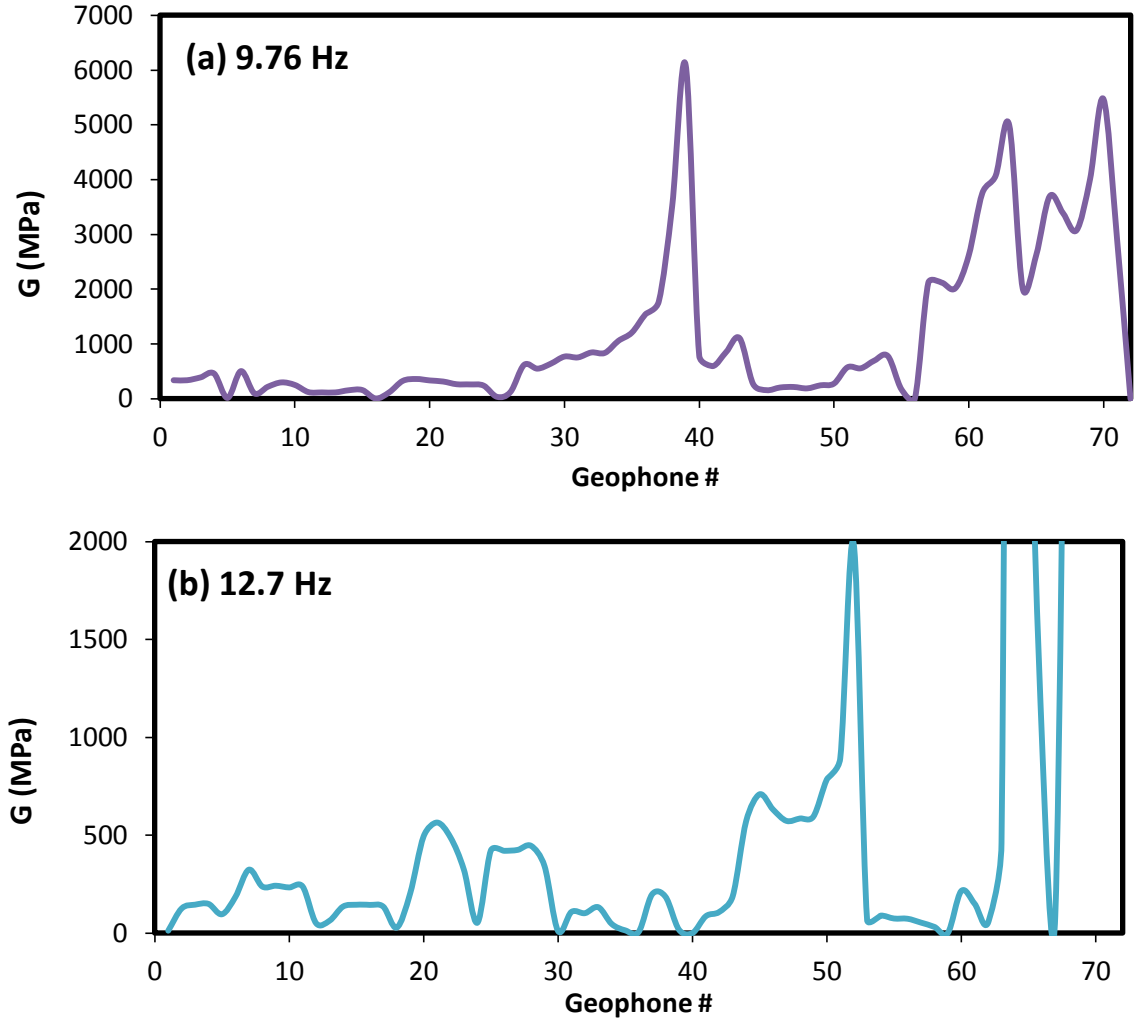

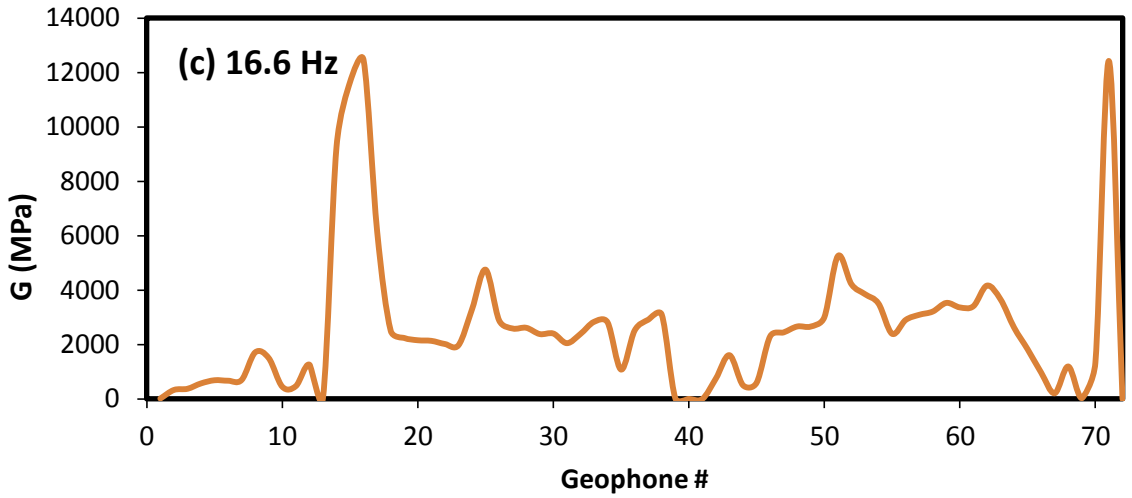

Figure 5.10. Shear moduli calculated for high frequency in second filtering method

The shear moduli graphs vs geophone number for high frequencies show an order of magnitude higher result compared to those obtained at lower frequencies. As mentioned previously, the peak frequencies obtained in this range are most likely due to the rotation of tires corresponding to truck speed. These frequencies could be due to the fact the geophones collected the vibration of the tire and not the ground at this frequency range. Hence, the moduli values in this range are not representative of the ground properties. Furthermore, according to basic wave physics, the higher frequency waves have lower wavelength. In the case of Rayleigh waves, the penetration depth of a wave is proportional to its wavelength. Therefore, high frequency Rayleigh waves must give more information from regions closer to the surface. In the case of oil sand material, the surface usually contains loose particles which result in lower moduli. This is contradictory to the results of shear moduli at higher frequencies where we obtained larger moduli values. This argument also supports the fact that high frequencies in the range of 10-20 Hz most likely result in unrealistic moduli values.

5.1.2.5. Change of source

So far, the calculations of shear modulus have been performed for the first seismic envelope. Some conclusions regarding the number of points for calculations of the slope of ϕ vs. d were made. Also, the choice of frequency is essential since the choice of frequency can significantly change a modulus value. Choosing low frequencies observed in the frequency response of the seismic data envelope seems to result in the most realistic results compared to that at high

frequency. However, such conclusions were drawn based on the data of a single data envelope. To establish a more conclusive selective rule for the analysis frequency, the data for another data envelope should be examined. For this purpose, the data envelope over geophone 10 was selected. Figure 5.11 demonstrates the selection of the time frame in which the maximum amplitude occurred for geophone 10. As expected, the beginning of the time frame is shifted to later time of 27.9 s compared to that of geophone 1. The wiggle plot representation of this data envelope is also shown in Figure 5.12. Similar to the previous section, the two filtering options were applied to this envelope. The phase angles vs. distance from source at geophone 10 in this case are presented in Figure 5.12. As these graphs show, the x-axis which is the distance from source extends to values smaller than those seen in Figure 5.7. This is due to the fact that as the source moves forward, a larger number of geophones will be in symmetrical distance from geophone 10 before and after the source.

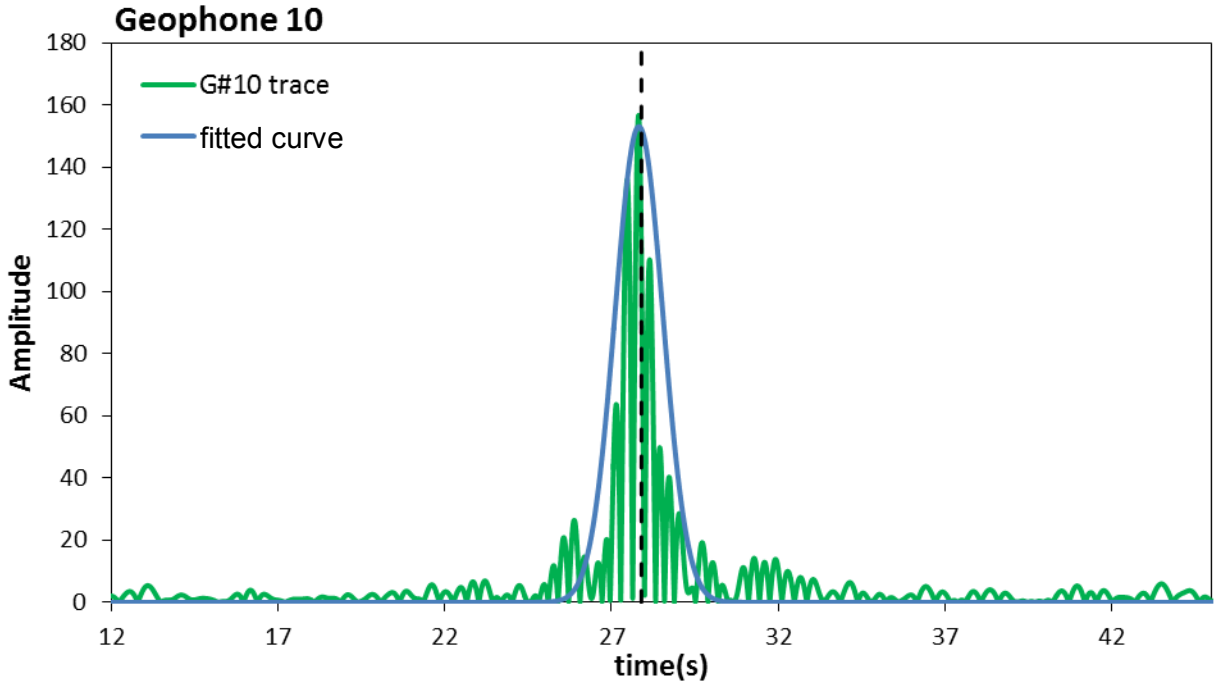

Figure 5.11. Selecting the time range for the geophone 10

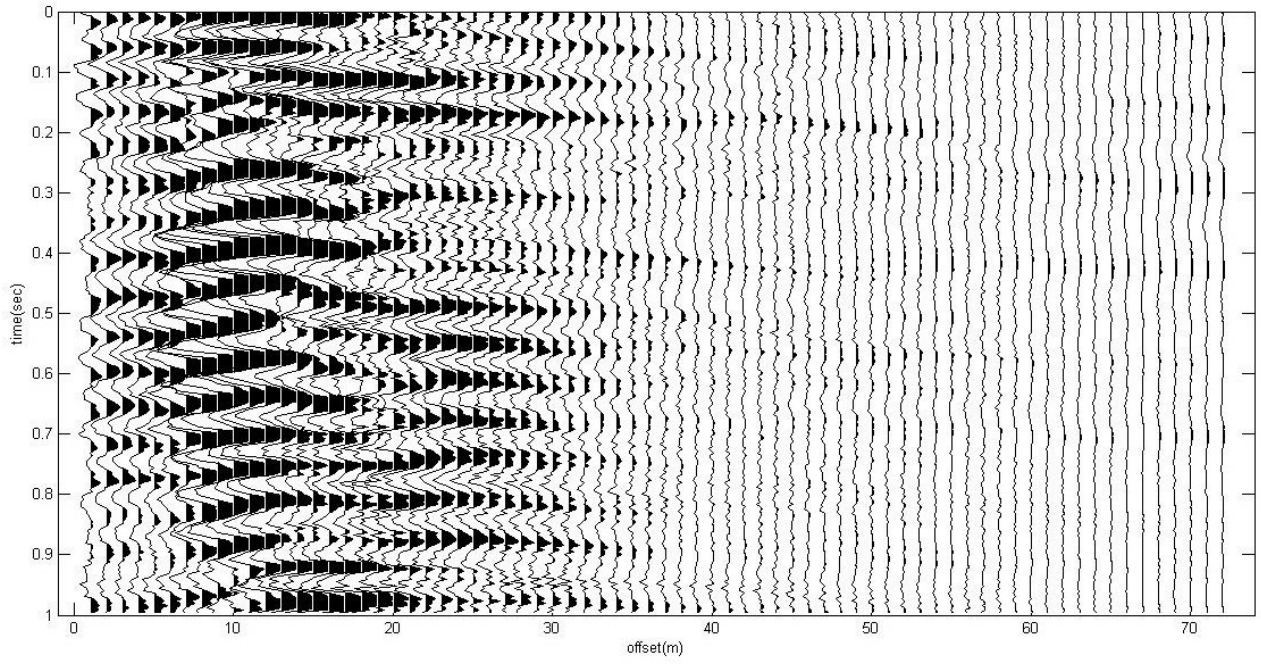

Figure 5.12. Seismic data envelope for the geophone 10

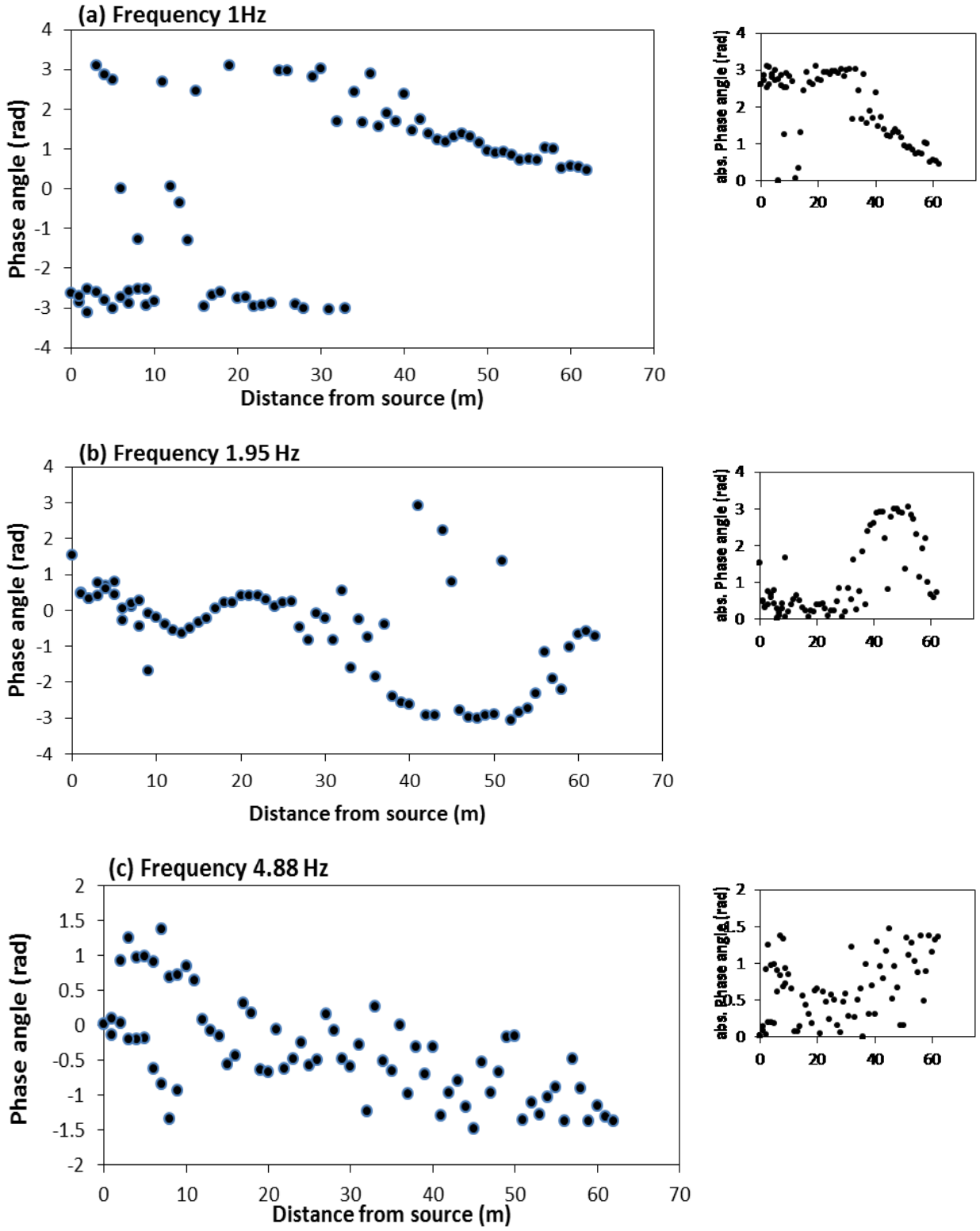

Figure 5.13. Phase-distance at 3 frequencies for geophone 10. Insets are the absolute phase value.

Using the filtered data and the slope of the phase vs. distance plots, we can establish the shear modulus plots as a function of geophone number. To help better visualize the variation of modulus by geophone, the values of the distance from source are converted back to the geophone number and plotted in Figure 5.14 for various frequencies.

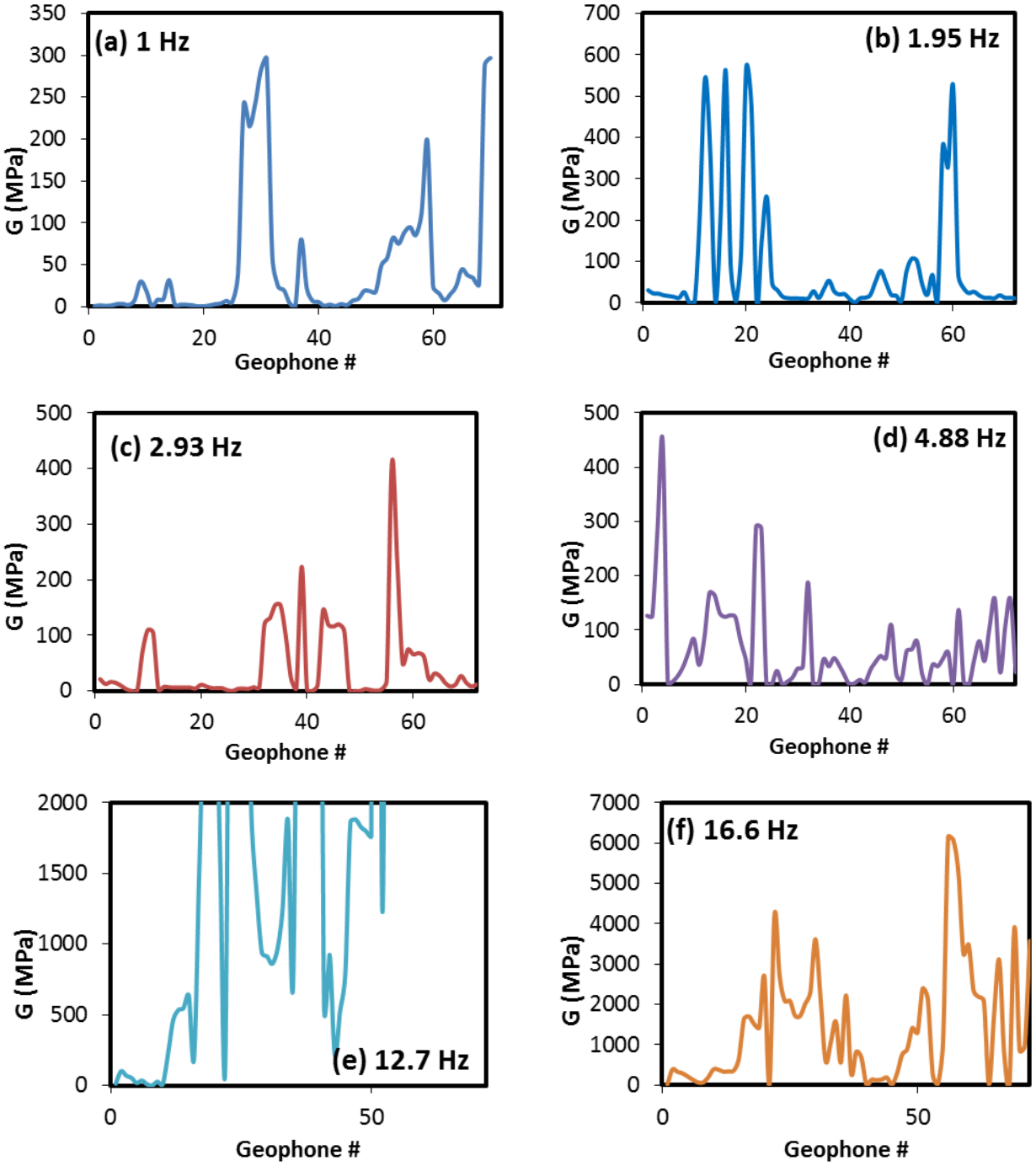

Figure 5.14. Shear modulus calculated for low (a,b,c) and high (d,e,f) frequencies (source G#10)

Similar to previous the case of the data envelope for geophone 1, the high frequency results show overestimation in the shear modulus of the ground. Again, we can conclude that the use of high frequencies which are mostly due to the tire rotation does not give realistic shear modulus values. Comparing the low frequency results, similar observation to the previous can be made. While the frequencies of 1.95, 2.93 and 4.88 Hz result in modulus values up to 500 MPa, frequency 1 Hz predicts somewhat lower range of up to 300 MPa. The trend is also different between these two categories where modulus in 1 Hz is high at around geophone 30 as opposed to the cases for 2.93 and 4.88 Hz with highest modulus at the beginning and end of array. From the above results and discussion, it could be concluded that the frequency 1 Hz is the most reliable choice to calculate the shear modulus of the ground. In the next section, more geophones were selected as the source and shear modulus at this frequency was calculated.

5.1.2.6. Shear modulus for different geophones as source

As previously discussed, the choice of low frequency seems to be essential for obtaining realistic results. Hence, in the following paragraphs the results of the shear modulus for several geophones are presented based on low frequency 1 Hz. The selection of this frequency is based on the fact that according to the results in previous section, the moduli of this frequency is the closest to the previously reported data in the literature. To keep the spacing between the data envelopes consistent, the data presented in this section are based on the case where geophones 20, 30, 40, 50, 60 and 70 are positioned under the truck and hence, as the wave source. However, in some cases where the geophone response contains too many spikes that may result in misidentification of the proper time frame, the response from the neighboring geophone are used. This will be indicated in the plots as well as the text.

Figure 5.15 shows the time frame selection for the case where geophone 20 is located underneath the truck and is the source position. Figure 5.15(b) also shows the wiggle plot of the seismic data for all geophones at that time frame. The time frame in this case is between 29.5 and 30.5 s. From this data the profile of the phase angle against the distance from source located at geophone 20 is extracted (Figure 5.16(a)). The shear modulus profiles vs. geophone number is then calculated and plotted for this frequency as shown in Figure 5.16(b). As the profile in this plot shows, the modulus is in a reasonable range of 5-200 MPa. Two regions of high stiffness can be seen in the ground based on this plot. The regions near the beginning of the array show

modulus as high as 90 MPs. The ground modulus is as high as 300 MPs close to the end of the geophone array.

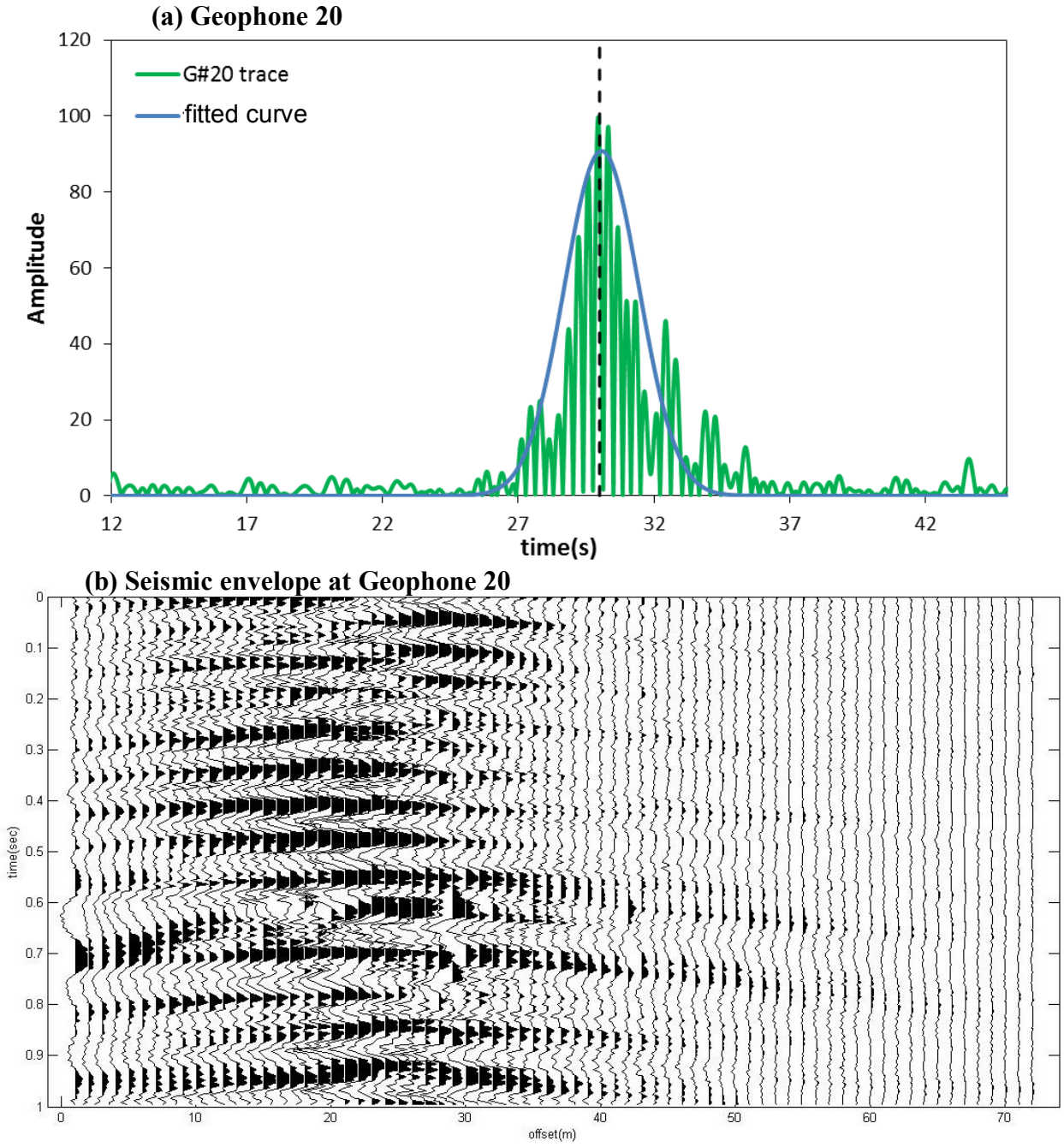

Figure 5.15. (a) Time frame selection and (b) seismic envelope data for the geophone 20 as source

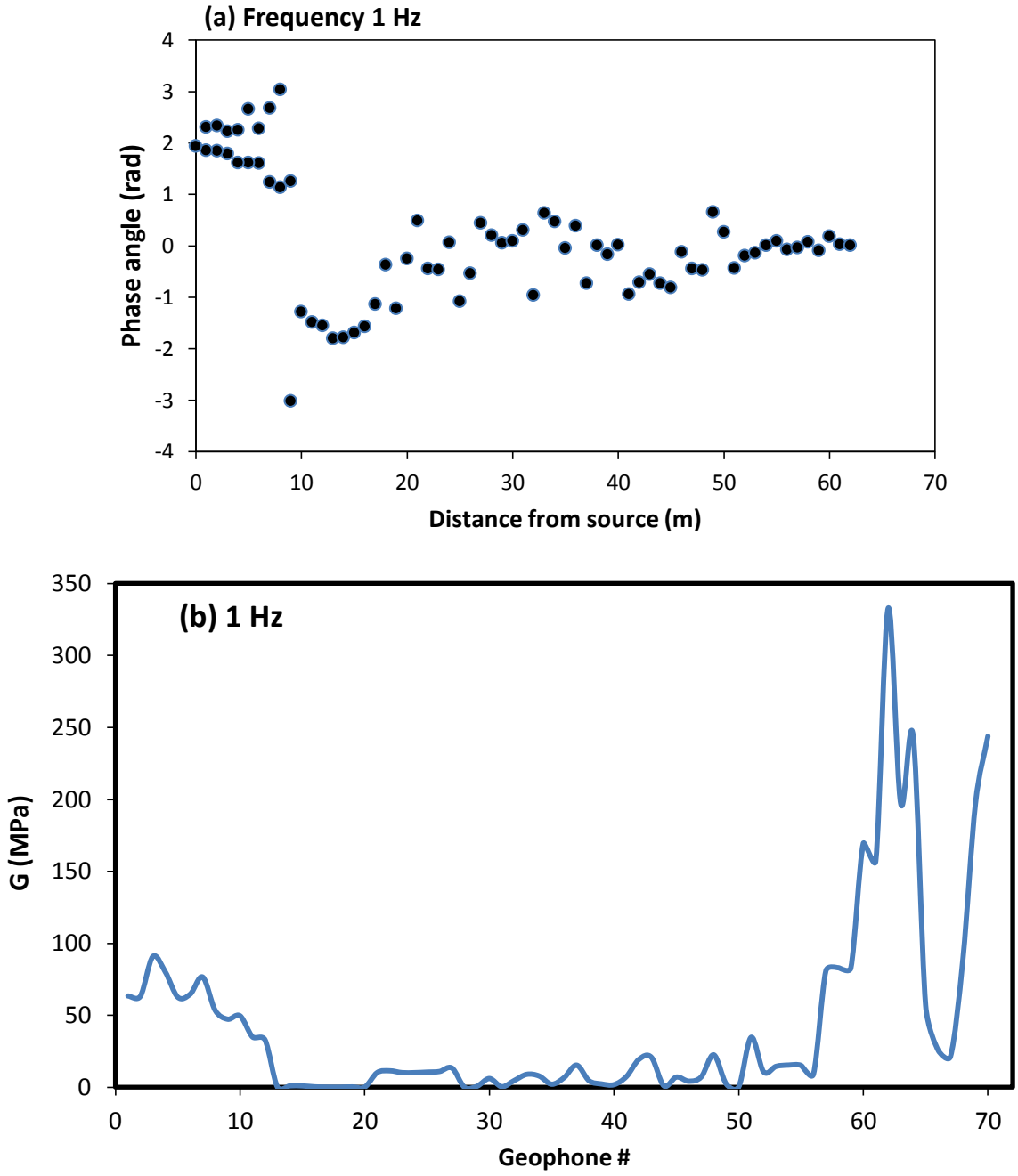

Figure 5.16. (a) Phase angle vs. distance and (b) shear modulus (source at G#20)

Again, a similar procedure was performed based on the position of source on the geophone with 10 m spacing. The response and time frame for geophone 30 is selected. The results of the source location at geophone 30 are shown in Figure 5.17 and 18.

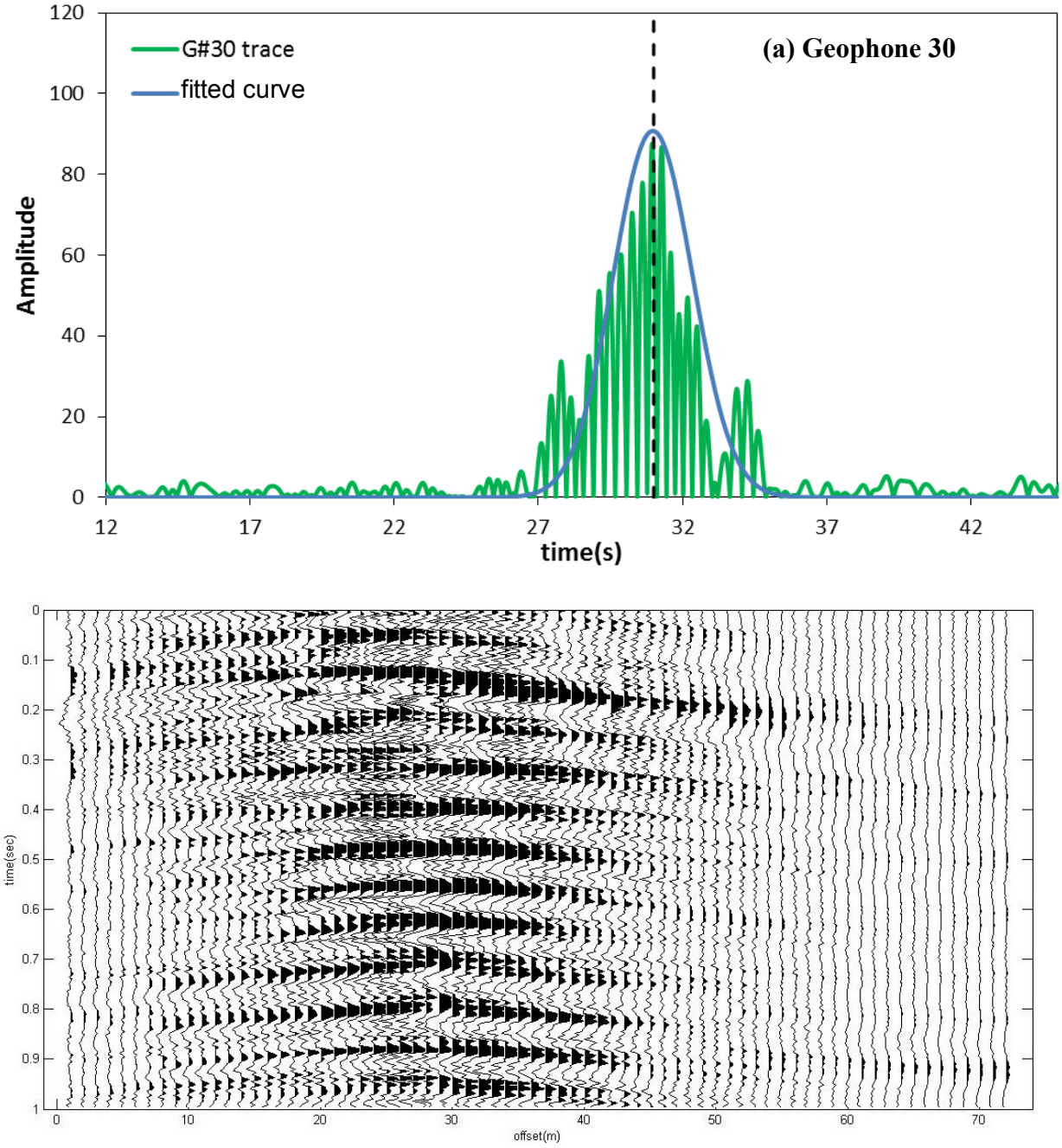

Figure 5.17. (a) Time frame selection and (b) seismic envelope data for the geophone 30 as source

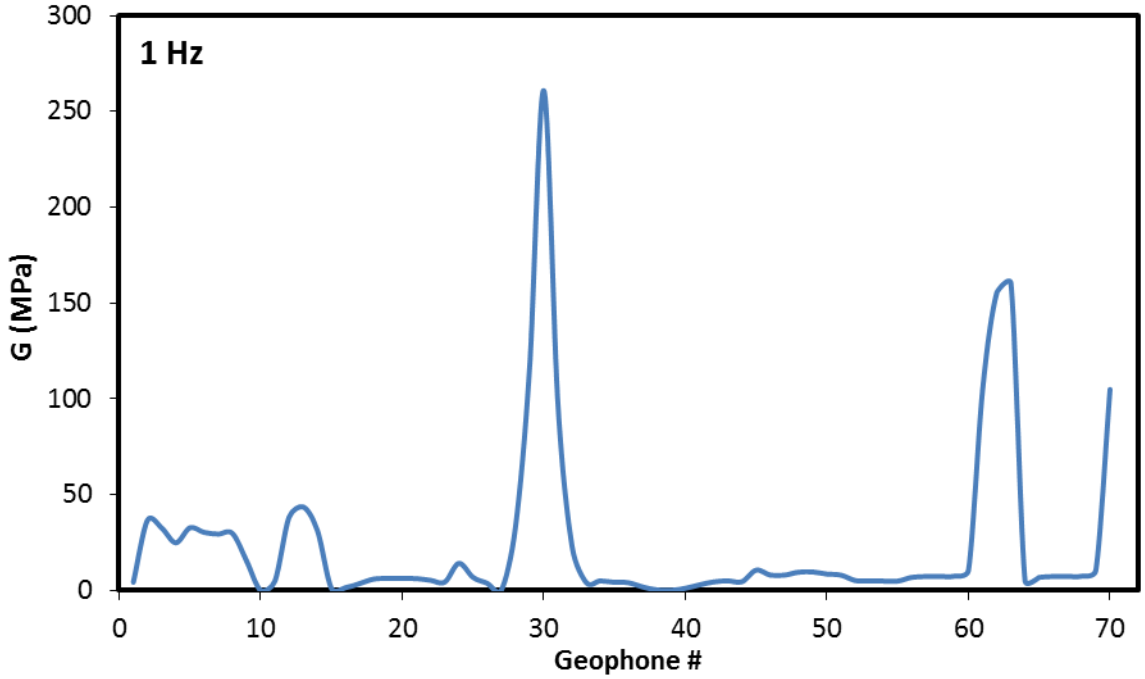

Figure 5.18. Shear modulus based on the position of source at geophone 30

Again, the regions near geophone 30 as well as 61 show some sign of high stiffness while areas close to the beginning of array still show softening characteristics. The next location as the source is at geophone 40.

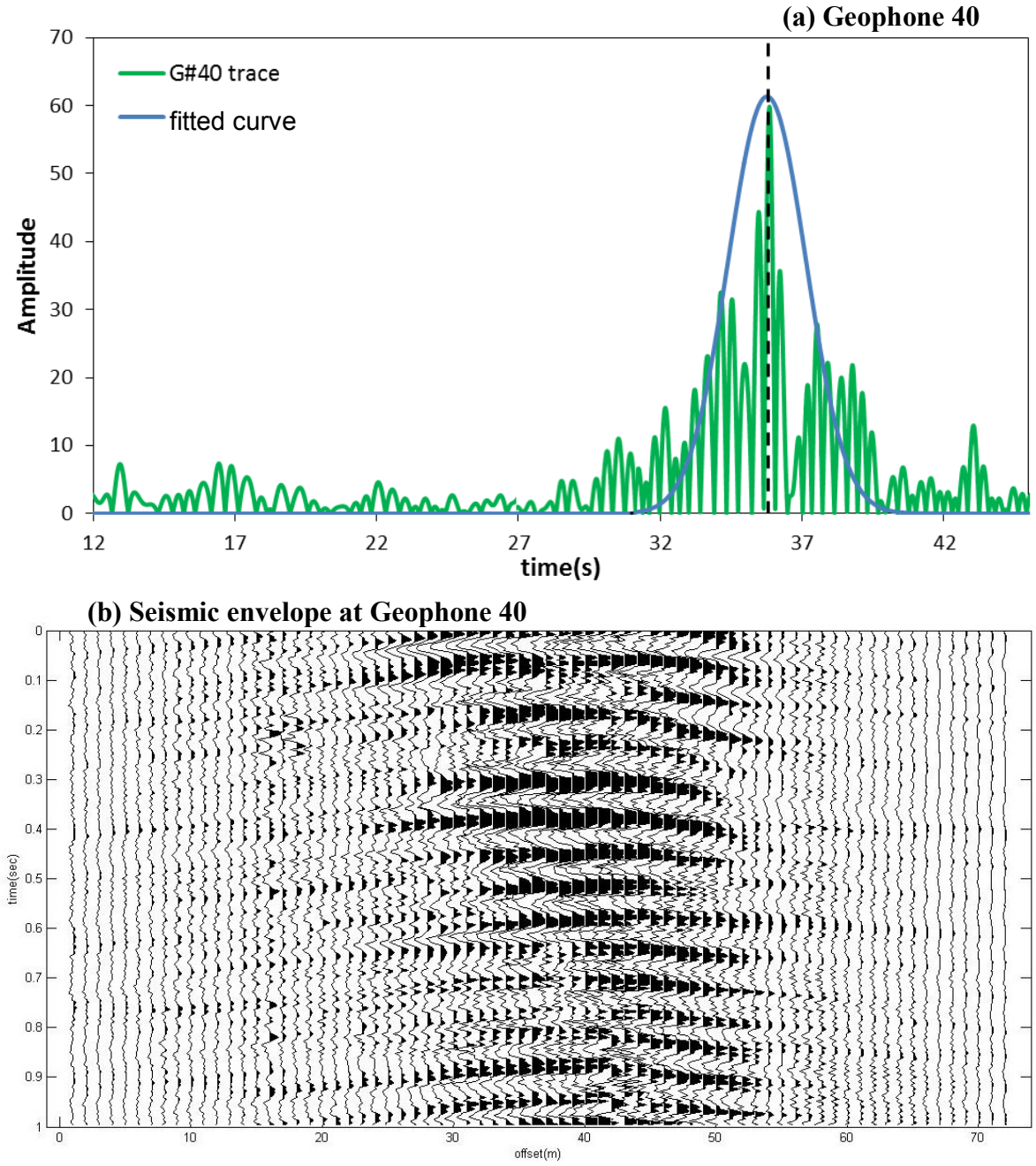

Figure 5.19. (a) Time frame selection and (b) seismic envelope data for the geophone 40 as source

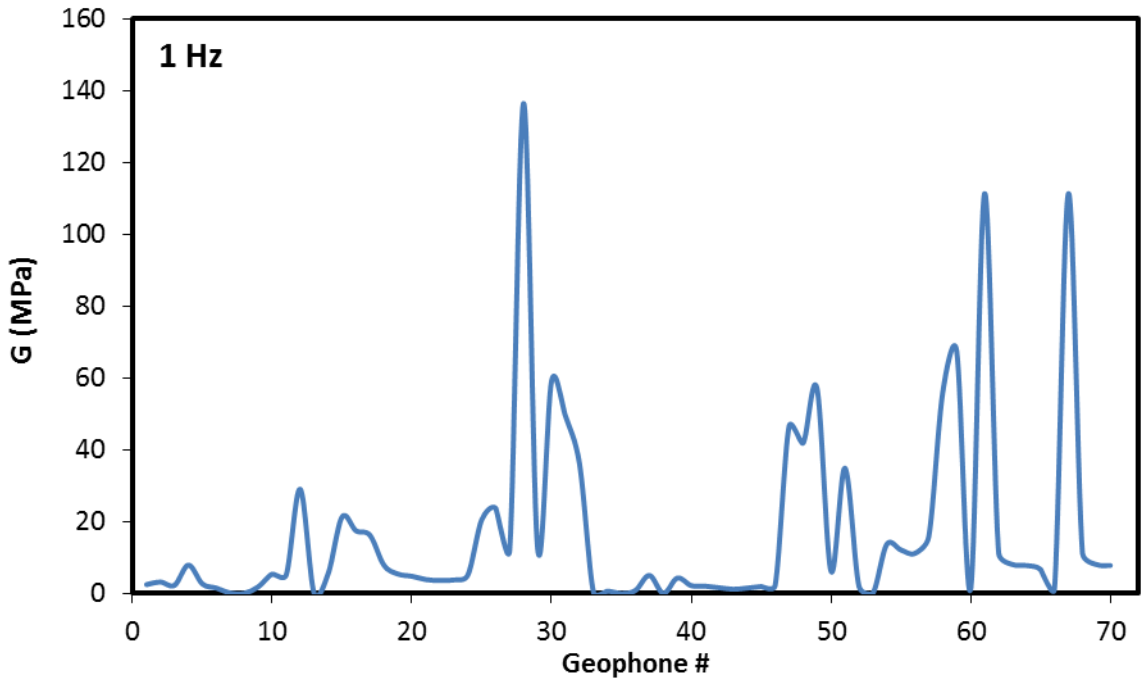

Figure 5.20. Shear modulus based on the position of source at geophone 40

In this case where the source is close to geophone 40, the ground seems to shows a similar behavior compared to the previous case. Some softening is still clear near the beginning of the array. The regions near the geophone 30 and 60 also show signs of high stiffness. The shear modulus in these parts extends to values up to 130 MPa and 100 MPa for geophone 28 and 61, respectively. The next series of data are taken from the time frame at which the truck is over the geophone 50.

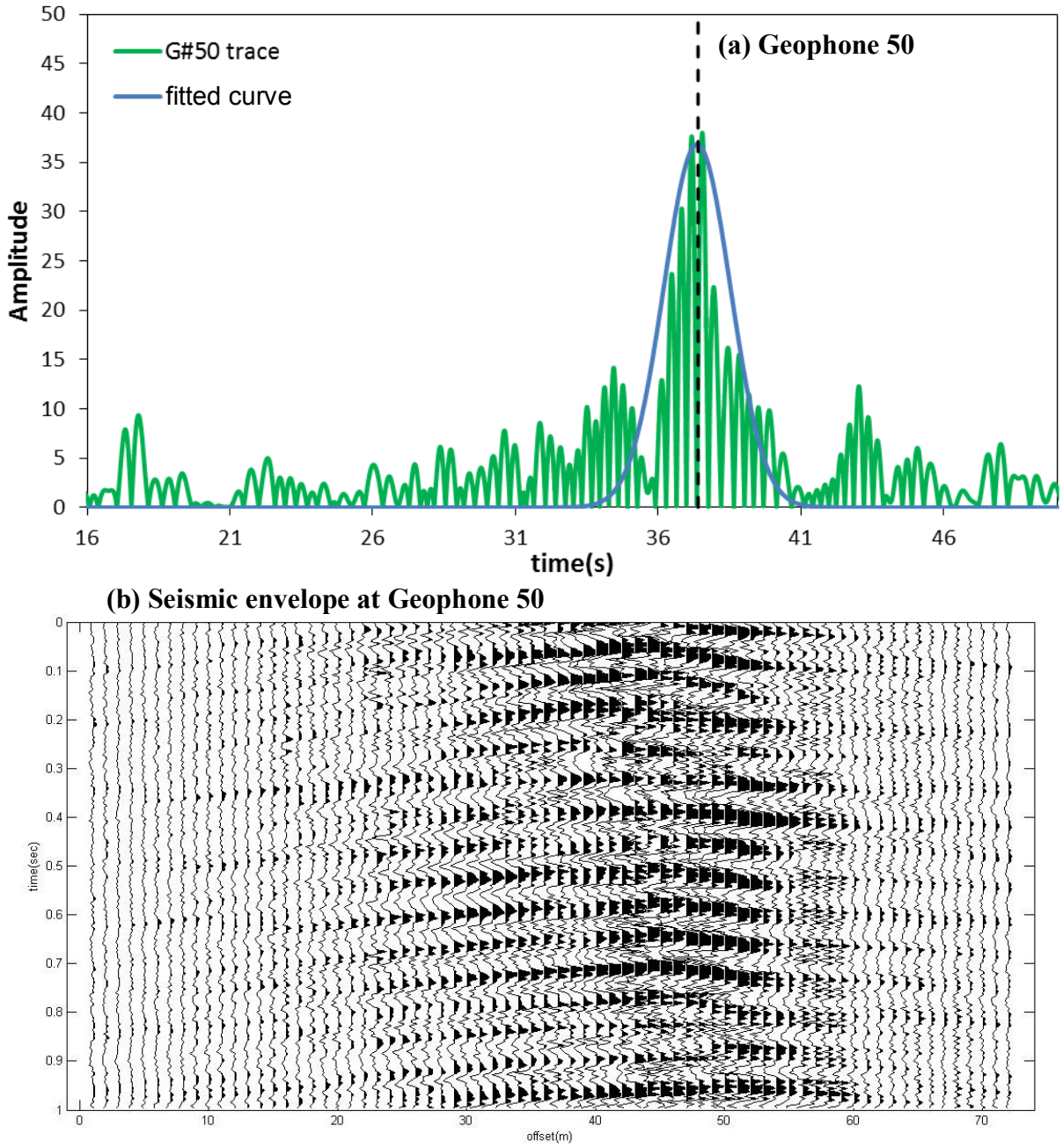

Figure 5.21. (a) Time frame selection and (b) seismic envelope data for the geophone 50 as source

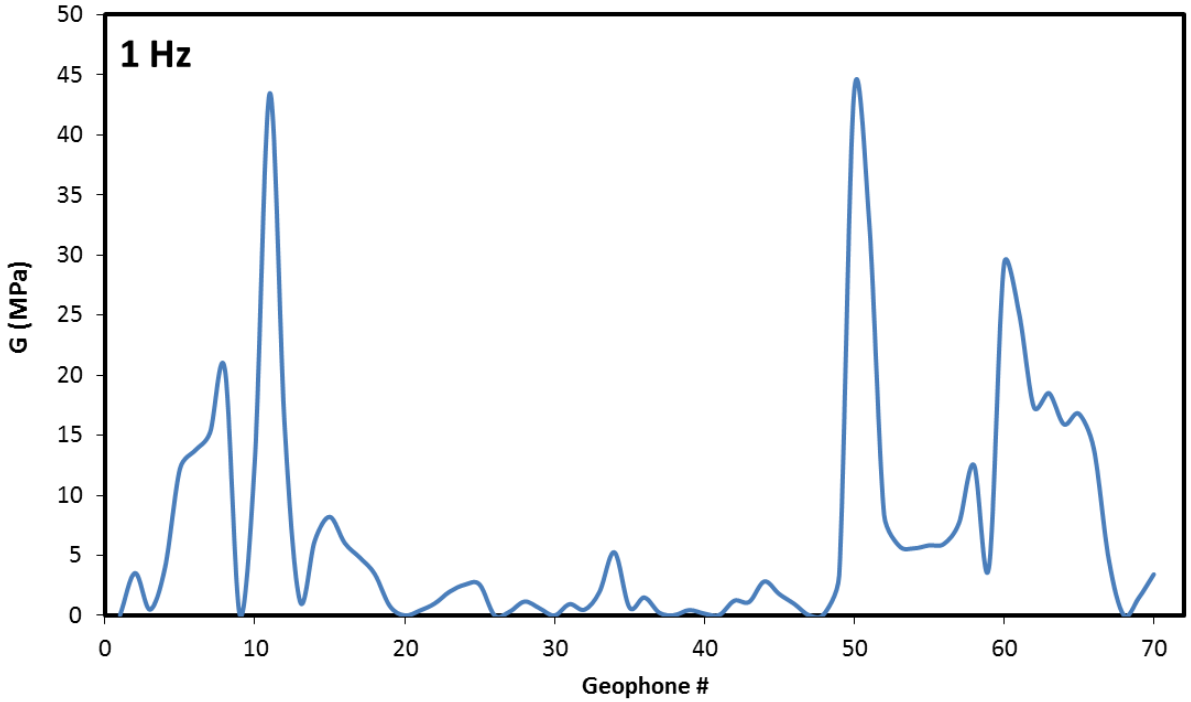

Figure 5.22. Shear modulus based on the position of source at geophone 50

Similar to previous source locations, the middle part of the geophone array indicates softer ground. As opposed to previous cases, the beginning of the array demonstrates some level of high modulus. The next locations of the source are at geophones 60 and 70 which are the last point we examine for our analysis.

(a) Seismic envelope at Geophone 60

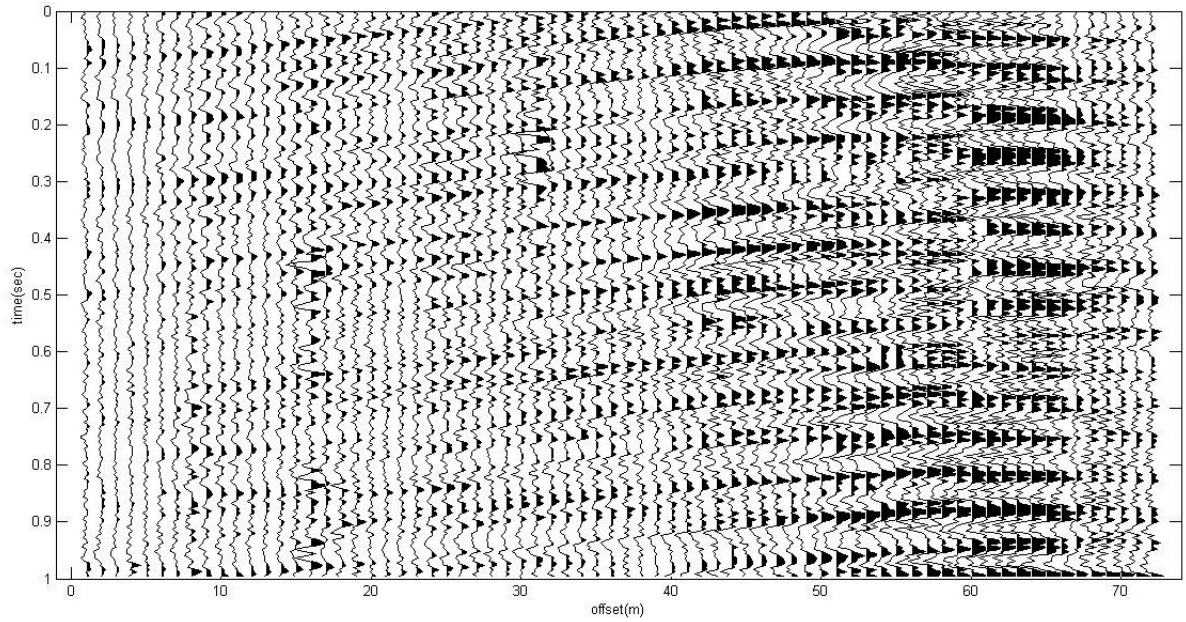

(b) Seismic envelope at Geophone 70

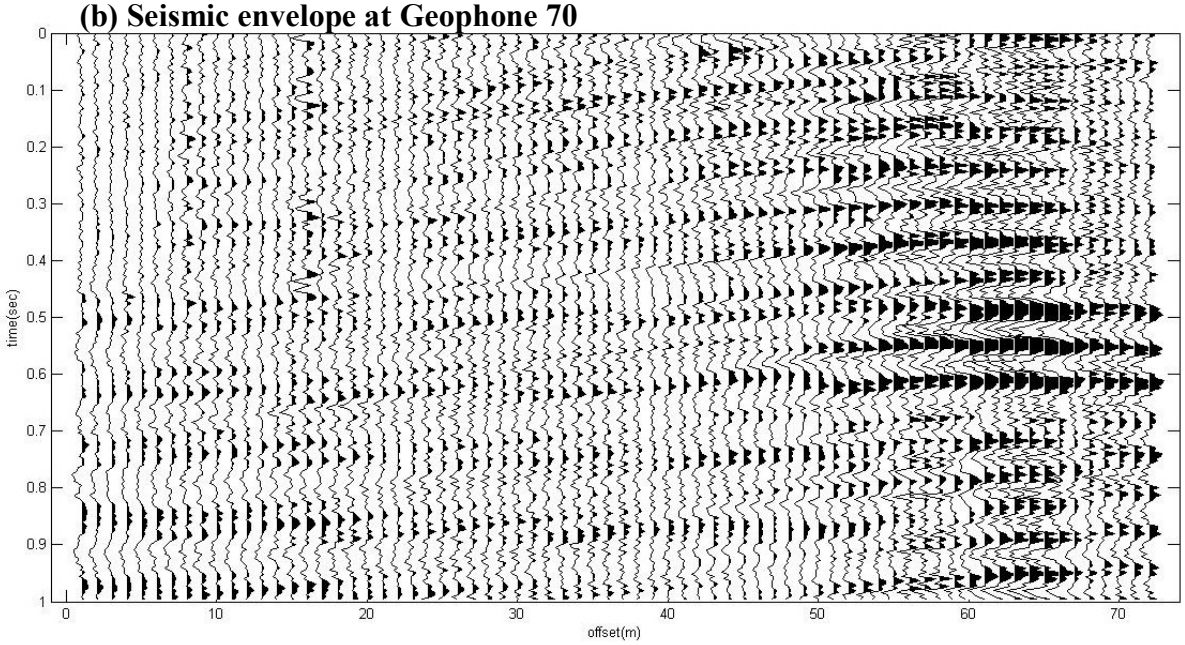

Figure 5.23. Seismic envelope data for the geophone (a) 60 and (b) 70 as sources

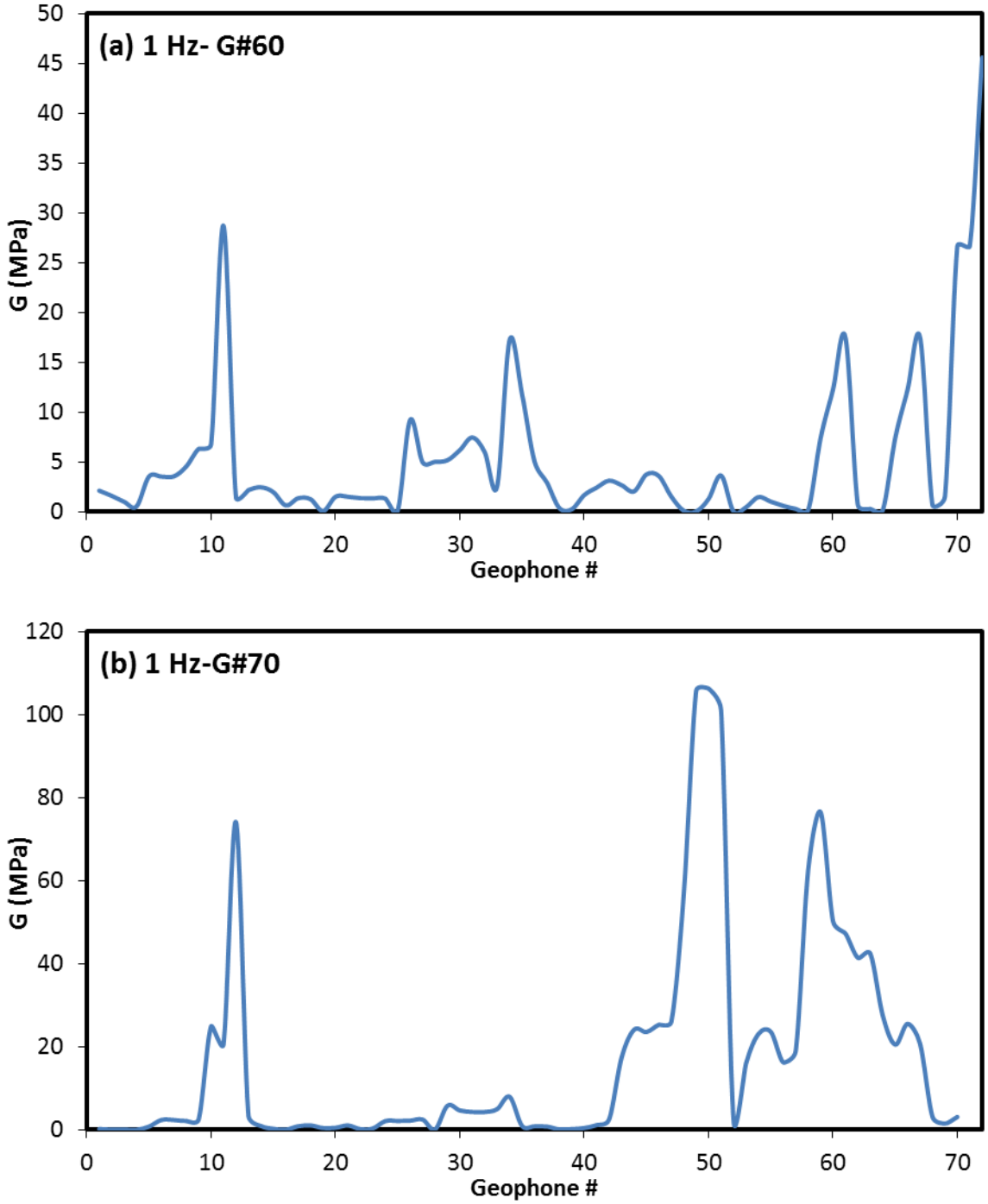

Figure 5.24. Shear modulus based on the position of source at geophone (a) 60 and (b) 70

5.1.2.7. Overall shear modulus and summary

In the previous sections, the shear modulus of the ground was obtained based on the surface wave method of analysis. In order to obtain meaningful results, we split the seismic results for

the array of 72 geophones into stationary data envelopes of 1 s time frame. This is due to the fact that as opposed to any conventional seismic test where the wave source has a fixed position, the source in our case is a moving truck. Hence, the analysis of the whole data range would face some complications due to the interference of waves. However, splitting the data into smaller data envelopes where we can assume that the truck is located near a certain geophone and hence, acts as a fixed source seems to be a reasonable solution. Using a well-known surface wave method we can analyse the individual data envelopes to estimate the shear modulus of the ground. In such an analysis method, having a wave of known frequency is a requirement. Since we have a moving truck which generates a range of frequencies, choosing the frequency to use in the surface wave analysis plays an important role. After using some filtering methods developed and described in the filtering chapter, only a few peak frequencies remained. The remaining frequencies can be divided into two groups of low and high frequencies. The low frequency range corresponds to those below 5 Hz. This is the range that we believe is related to the pure truck tire-ground interactions where the effect of all noises and even the tire rotation are not present. Among six main frequencies in this range, only one was found to result in the most realistic shear modulus. On the other hand, the high frequency range corresponds to the rotation of the tire which generates series peak frequencies in the range of 9-20 Hz. The main peak frequencies studied in this range were 9.76, 12.7 and 16.6 Hz. After examining the shear modulus values in this frequency range for two cases of data envelopes, we concluded that the use of these frequencies overestimates the modulus and most likely results in unreliable values. Hence, for part of our analysis, we only calculated the shear modulus in the low frequency range which seemed to give consistent results. With the purpose of having an even amount of spacing between the positions of the geophone acting as the location of the source, we analysed the data for seven different envelopes. Despite the presence of few inconsistencies, the overall range of calculated shear modulus is between 20-150 MPa. This agrees with the previously reported values for similar analysis of the oil sand [45]. However, drawing conclusion based on the individual results of the envelopes might not be the best representation of the ground modulus over the range of geophone array. A more conclusive method to present the stiffness of the ground along the geophone array could be to take the average of the values obtained in each case. This way, an average of seven data points results in the shear modulus of the ground at each frequency. Figure 5.25 demonstrates the average shear modulus of the oil sand in our study

based on the seven different cases of data envelope analysis. As the graph shows, the general trend in the modulus is that the areas in the middle and beginning of the geophone array have smaller values compared to the regions close to the end and of array as well as near geophone 30.

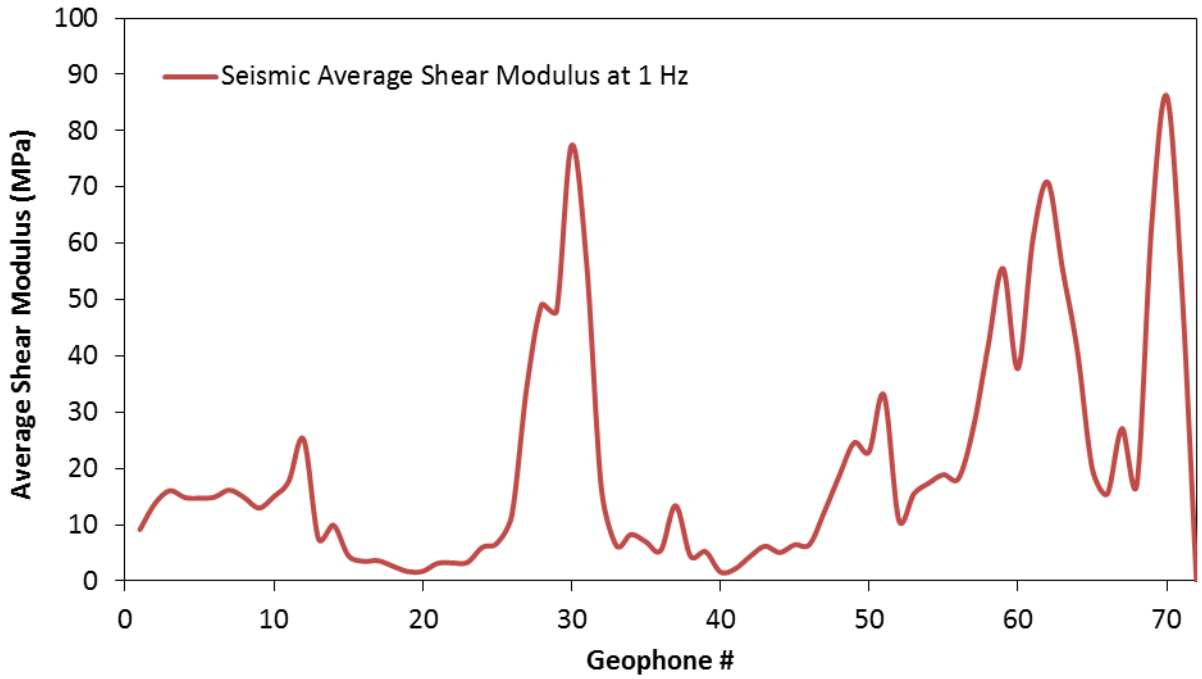

Figure 5.25. Average shear modulus based on different source positions

Overall, the surface wave seems to be a simple though effective route to obtain the shear modulus of the ground from a single seismic run. Besides, the idea of splitting the whole range of seismic analysis into smaller stationary envelopes of seismic data seems to be a useful method to analyze passive seismic traces. This method seems to have eliminated the complication of a moving source and produce reasonable ground properties. To our knowledge, this is the first report on the application of such an idea for analysis of complex passive seismic data analysis where moving vehicles are used as the source. The next step in our analysis is to perform a simple study on the sensitivity of the obtained shear modulus on the pre-assumed properties of the ground.

5.1.2.8. Sensitivity analysis

As seen in the previous sections, the shear moduli of the ground can be obtained using a simple surface wave method. By applying this method on stationary envelopes of seismic data taken from a larger passive seismic analysis, we can predict the modulus of the ground at each geophone. Taking the average of values gained from each set of data provides an overall picture of the variation of the ground stiffness along the geophone array. It is worth to note that the calculation of the shear modulus is based on the equations provided in the previous sections (Eq. 54-60). As can be seen in these equations, two input parameters are required to be pre-determined for these calculations.

The density of the ground is assumed to be known and constant during the analysis. This is not necessarily a correct assumption as the properties of the ground can undergo significant softening/strengthening as the truck passes over the geophone array. Performing a separate study on the variation of the ground density during the course of seismic data acquisition seems to be an essential experiment. However, the seismic data used for this study were not accompanied with such a study. Hence, the value for the ground density has been assumed based on previous studies on similar materials. Fortunately such data exists in the literature for oil sand material. According to Sharifabadi [13] the density of the oil sand varies between 1.7-2.1 Mg/m^3 depending on the bitumen content of the oil sand. These values were obtained from the laboratory experiments and compacted oil sand samples to certain extent. One can imagine that the surface of the oil sand which has been under several loading/unloading cycles due to the motion of the heavy vehicles could be extremely loose. Hence, density values could be somewhat even lower than the lower limit of the above range. Hence, we can make few assumptions of the density of oil sand and explore the influence of the variation in the density on the shear modulus value. Several different values of the oil sand density are selected for our analyses are in the range 1.5-2.1 Mg/m^3. Figure 5.26 demonstrates the variation in the values of the oil sand shear modulus with changing the density. As this graphs shows, seven different density values were input as the ground density in calculation of the shear modulus. As expected, the shear modulus increases with increasing the density when all the other parameters are constant. It is worth mentioning that the Poisson ratio is assumed 0.3 for all these calculations. The solid red and black lines indicate the highest and lowest limits of the shear modulus based on the high and low limits of the density range. Figure 5.26(b) shows a more simple

representation of the effect of changing the density on the shear modulus. The black line represents the average shear modulus value for all the density range. The shaded area shows the standard deviation of this average value. The percentage of the variation for each point on the geophone array is about 12%.

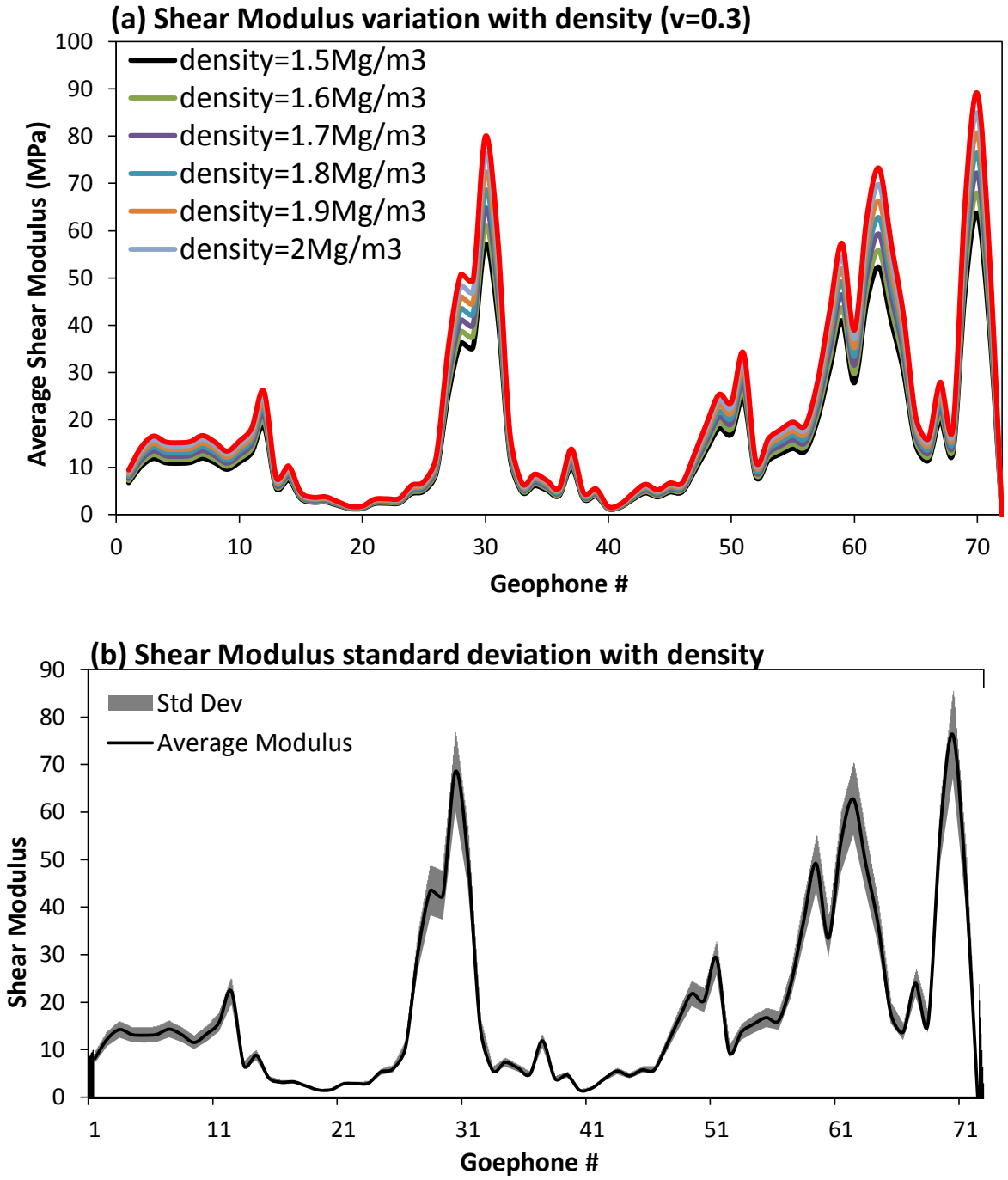

Figure 5.26. (a) Variation of the shear modulus with density, (b) upper and lower limits

The second factor that is assumed for the calculation of shear modulus in surface wave method is the alpha, α factor according to Eq. 60. In fact, this factor is calculated based on the assumption of the Poisson ratio according to Eq. 57. Hence, Poisson ratio is the underlying second factor. A range of Poisson ratios have been reported for Athabasca oil sand materials. According to different reports, a range of 0.25-0.35 was chosen for our sensitivity analysis. Five different Poisson ratios of 0.25, 0.28, 0.3, 0.33 and 0.35 are selected. Solving Eq. 57 results in five different α values of 0.9194, 0.9243, 0.9274, 0.9320 and 0.9350. Figure 5.27 shows the results of variation of Poisson ratio and hence, α on the shear modulus of the oil sand calculated based on the surface wave method. The density of the oil sand is kept at constant value of 1.8 Mg/m^3 which is the average value of the previously mentioned density range.

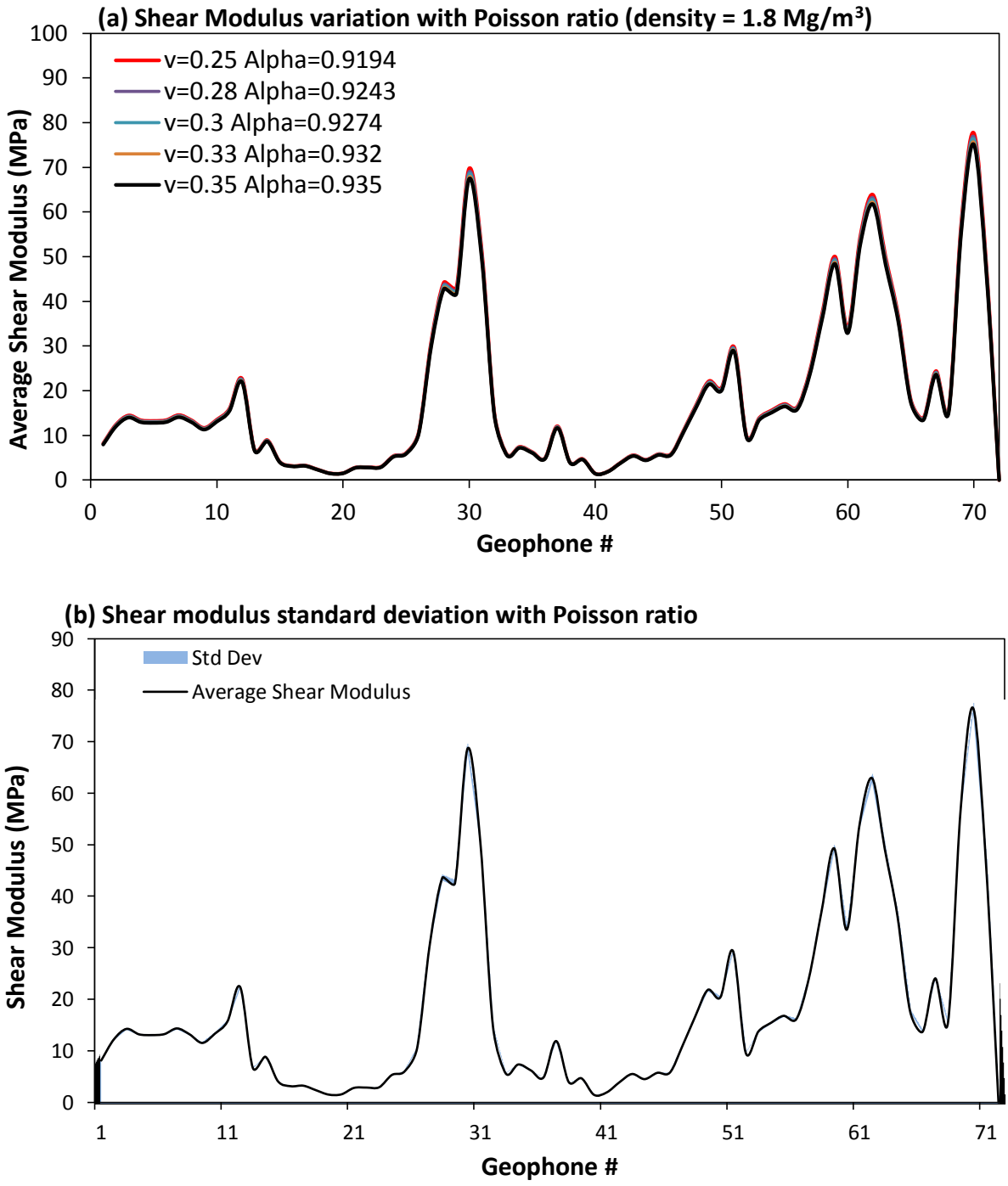

Figure 5.27. (a) Variation of the shear modulus with Poisson ratio, (b) upper and lower limits

As these graphs show, the variation of the Poisson ratio and α has less influence on the shear modulus value compared to the case of density. The upper and lower limit bands of the shear

modulus are not clearly visible in Figure 5.27(b) due to such low sensitivity. This could be due to the fact that the variation of 0.25 to 0.35 for the Poisson ratio results in smaller variation in α in the range of 0.9194 to 0.935 in terms of standard deviation.

A slightly more complicated sensitivity analysis can be performed by combining the density and Poisson ratio ranges. This can be performed by assuming the upper, middle and lower values of each range in combination with each other. For instance, the highest possible shear modulus value based on these two ranges and Eq. 60 is when the density is chosen as the upper limit value (2.1 Mg/m^3) and the lower limit Poisson ration and α (0.25, 0.9194) are chosen. Several combinations of density and α can be assumed in a similar manner. Figure 5.28 shows the combination that can be used for this analysis.

$G=f(\rho,\alpha(\nu))$	ρ	$\alpha(\nu)$
G_{max}	ρ_{max}	α_{min} (ν_{min})
G_{min}	ρ_{min}	α_{max} (ν_{max})

Figure 5.28. Combination of density and alpha for shear modulus calculation

Figure 5.29 demonstrates the variation of the shear modulus in our seismic analysis with different combination outlined in Figure 5.28.

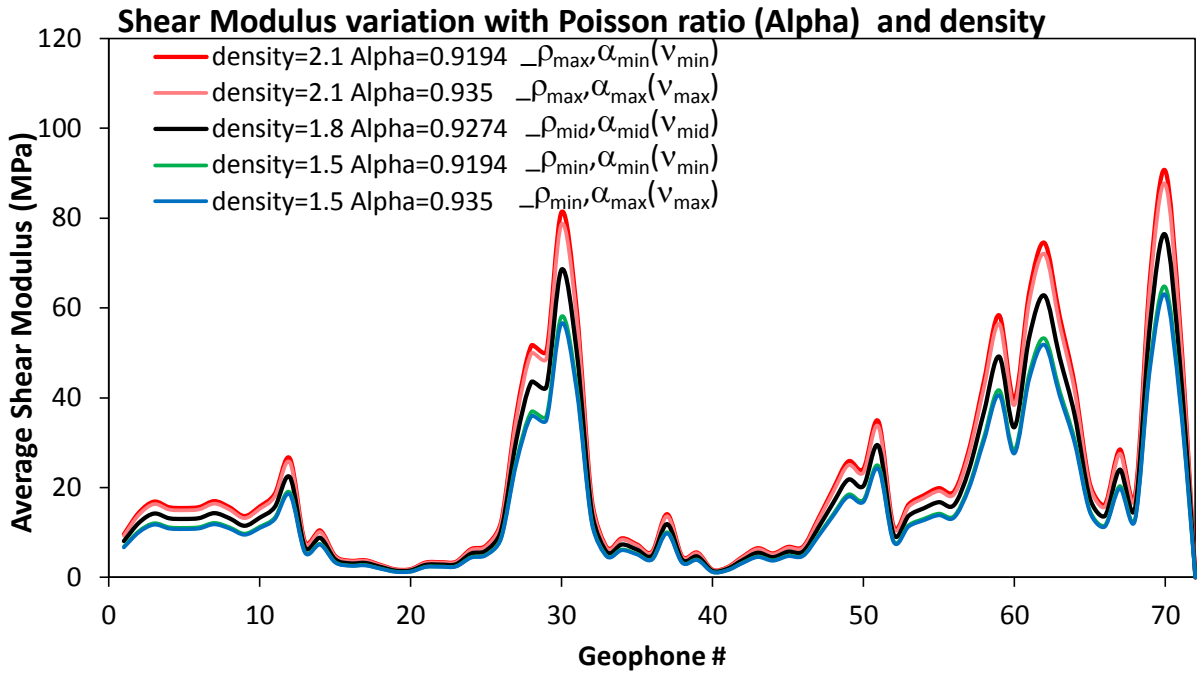

Figure 5.29. Variation of the shear modulus with Poisson ratio and density

The graph shows the strong sensitivity of the shear modulus to the variation of density rather than α. The top two lines with the highest shear modulus belong to the cases in which the maximum density of 2.1 Mg/m^3 is selected. Changing the α value seems to have small effect in the shear modulus values. Even using the highest α value which is inversely proportional to shear modulus does not seem to affect the overall curve as much as the variation of density. The black line represents the values of shear modulus based on the average values of density and α in their corresponding ranges. The two curves at the bottom correspond to the cases where the least value of density, 1.5 Mg/m^3 is chosen. Again, small variation between the two curves is caused by the change in α values.

Overall, the results of our sensitivity analysis suggest that variation of the ground density has strong effect on the calculation of the shear modulus. On the other hand, a fairly large variation of the Poisson ratio results in relatively small variation in α which in turn has small influence on the shear modulus. From these results we can conclude that performing a separate test on the density variation during the course of seismic data acquisition can be strongly beneficial. This could be the subject of future investigations for obtaining the properties of the ground using seismic surface wave method.

Chapter 6

6. Comparison of seismic analysis vs. VIMS

In the previous chapters, we performed different types of analysis on two types of data acquired from the surface of an oil sand field. In one experiment, a series of 72 geophones were placed on straight line at a constant distance from a shovel loading a haul truck. As the truck was traveling along this array, the geophones acquire a large amount of data from underneath the surface of ground. At the same time, the truck onboard data acquisition system known as VIMS also records the forces applied to all struts in the truck as well as many other parameters. While the type of data acquisition is different between the two methods, several conclusions can be drawn based on analysing both data series. The comparison of these conclusions and correlating the two methods might give us insight towards the use of each method instead of the other to predict the properties of ground.

6.1. Oil sand properties from surface wave method

In the previous chapter, the use of surface wave methods to analyse the behavior of Rayleigh waves in the ground was presented. A major challenge in analysing our data compared to any other seismic data is the moving nature of the wave source, i.e. truck. Another challenge is the wide range of frequencies in our data which contains characteristic peaks from various additional sources. Hence, the application of different filtering options is necessary to identify the proper frequency for the surface wave analysis. Once the most applicable frequency is selected, seismic wave methods can be performed using the signals in that frequency. The following paragraphs summarise the results of our seismic wave methods to obtain the properties of ground along the distance of geophone array.

The shear modulus of the ground is an important parameter which provides significant information about the behavior of ground. The surfaces wave method allows for obtaining the shear modulus of the ground around any chosen geophone based on the signals of surrounding geophones. In this method, we are basically tracking the behavior of a certain series of waves selected by their frequency. The velocity of these waves traveling through the surface of the ground can be determined based on their frequency and phase angles variation along the

geophone array. From the velocity of the waves around any given geophone, we can estimate the shear modulus of the ground. The procedure of selecting the proper frequency, number of geophones contributing to the calculation of shear modulus and the average value of shear modulus based on calculations for several geophones are explained in details in previous chapter. In this chapter, two more important parameters that can be obtained from the shear modulus are introduced. The first parameter is the Young's elastic modulus of the ground which can be calculated based on the knowledge on the mechanical properties of elastic bodies using the following equation [36]:

$$E = 2G(1+\nu) = 2\rho(1+\nu)\left(\frac{V_R}{\alpha}\right)^2 \qquad (62)$$

The parameter ν is the Poisson constant and α is a ratio described in the previous chapter. Similar to the values of shear modulus which were obtained based on the average of several analyses from different geophones, the elastic modulus can also be determined using Eq. 62. Figure 6.1 demonstrates the average elastic modulus along the geophone array bases on our passive seismic data. Similar to the case shear modulus, the sensitivity of the elastic modulus to the Poisson ratio is also presented in this plot.

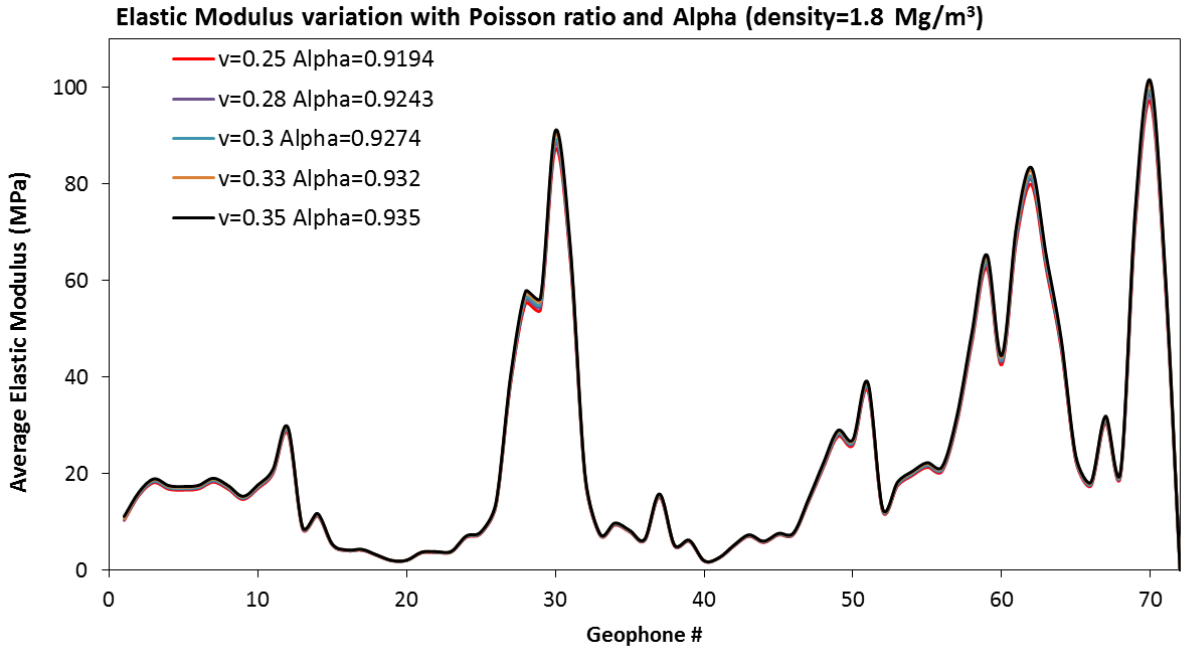

Figure 6.1. Average elastic modulus of the ground based on different Poisson ratios

As can be seen in this plot, the elastic modulus follows the same trend as the shear modulus. The variation of the elastic modulus with Poisson ratio is also shown in this plot. The elastic modulus increases with increasing elastic modulus. However the magnitude of such an increase is suppressed to some extent by the inverse effect of alpha. As seen in previous chapter, the increase in Poisson ratio increases alpha. At the same time shear modulus and hence, elastic modulus is inversely proportional to alpha. However as Figure 6.1 suggests, Poisson ratio has stronger effect on the elastic modulus compared to alpha. Overall, it seems that an elastic modulus obtained by surface wave methods is not strongly sensitive to the choice of Poisson ratio in the range of 0.25-0.35. It is worth noting that the density of the oil sand is assumed constant in Figure 6.1.

The next important parameter that can be obtained from shear modulus is ground stiffness. This is an important parameter which provides key information on the behaviour of the ground which can affect the structure and stability of the equipment traveling over it. It has been shown [12] that there are some correlations between the stability of the truck and shovel in mining and the properties of the ground. Joseph [12] also showed that through monitoring the properties of the ground it is possible to prevent many of the destructive effect of the ground on the mining equipment. According to Joseph [12] the ground stiffness can be obtained from the following formula:

$$k = \frac{EA}{D} = \frac{2G(1+\nu)A}{3\sqrt{A}} = \frac{2G(1+\nu)\sqrt{A}}{3} = \frac{2}{3}\rho(1+\nu)\sqrt{A}\left(\frac{V_R}{\alpha}\right)^2 \qquad (63)$$

Where D is an empirical estimation of the depth of influence and is equal $3\sqrt{A}$ and A is the footprint area. The stiffness is a factor which depends on the footprint area as well as the shear modulus. Footprint area should be measured separately during the test. It is also worth noting that it varies with the motion of the truck and the properties of the oil sand. For instance, the soft ground and high payload tend to increase the footprint area. Thus, it is expected that the different regions along the geophone array have different footprint areas. This highlights the fact that it is necessary to perform separate experiments to investigate the variation of the footprint area at different regions of the array. However, for the case of our analysis we assume a constant footprint area as the measurement of area at the time of seismic data acquisition has not been performed. Figure 6.2 demonstrates the load stiffness of the ground based on the shear modulus

obtained from seismic analysis and using Eq. 63. As expected, the stiffness follows a trend similar to that of shear modulus.

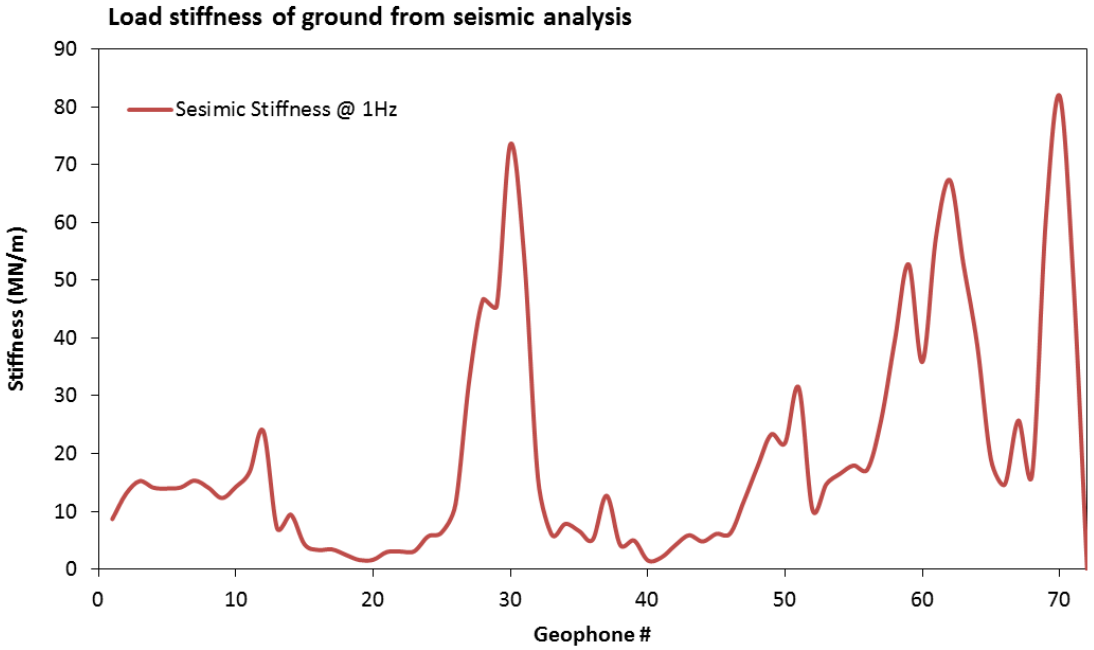

Figure 6.2. Average load stiffness of the ground from seismic analysis

As can be seen in this plot, the stiffness has a unit of MN/m which is why it is called the load stiffness. The stiffness varies within the range of 1.5-75 MN/m. The regions close to geophone 30 as well as geophones 50 and 60 show the highest stiffness values. In the next section, the calculation of load stiffness from the VIMS data is presented. The results of two analyses will be compared at the end of that section.

6.2. Oil sand properties from VIMS data

The most important portion of the VIMS data consists of the strut pressure values from individual sets of tires being in four major categories of left front (LTF), right front (RTF), left rear (LTR) and right rear (RTR). The calculation of force exerted on the ground based on each of these values is the first step towards obtaining ground properties. This can be done using the cross section area of front and rear struts and the measured pressure values. Based on the manufacturer specifications, the front strut has a diameter of 15.75” while the rear strut is 15” in diameter [47]. Figure 6.3(a) and (b) show the strut pressures and load calculated based on the cross section area of struts for all four sets of tires within the time frame of seismic data

acquisition. It should also be noted that the time scale for VIMS data has been corrected for the drift according to the method described in chapter 4.

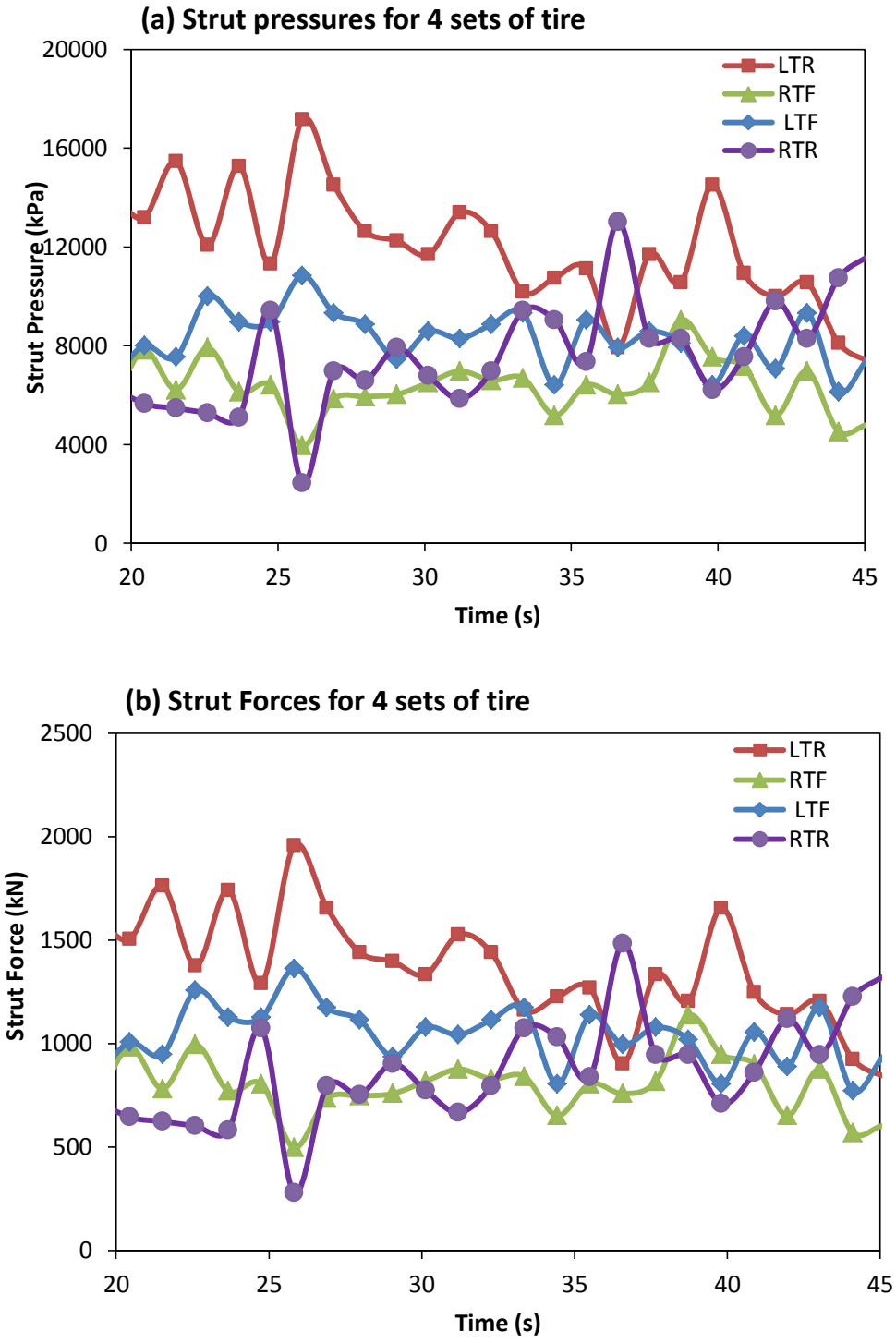

Figure 6.3. Strut (a) pressures and (b) forces for all sets of tires

Now that the forces exerted on the ground from each of four sets of tires are determined, the next step is to investigate the influence of such forces on the ground. The most intuitive and reasonable parameter is the deformation of the ground due to these forces. This can be obtained from the individual seismic traces. As discussed in chapter 4, the area underneath the seismic peak area could give useful information about the ground motion. Also it was also mentioned that fitting a simple Gaussian curve results in the best approximation of the area. Combining the information in chapter 3 considering the output signal of the geophones and the area under the seismic peak region can give us an estimation of the ground deformation. This is based on the assumption that the geophone output is in the form of particle velocity and multiplying that by the time results in the area under the peak with the unit of m/s.s or meter. However, an important step is to assure that the geophone output has the right units. The next section discusses this subject.

6.2.1. Particle velocity and ground deformation

As mentioned in previous chapters, the most common instrument to collect seismic waves is the geophone. As was shown in chapter 3, at frequencies close to and above the resonant frequency, one can expect direct proportionality between the output voltage and ground particle velocity. Once the particle velocity is obtained, we can investigate its correlation with the data acquired by an on-board system.

In order to obtain meaningful voltage output from the geophone array signals, it is necessary to perform appropriate filtering to remove all unwanted signals. It is also essential to know the type and characteristics of the geophone used for the seismic study. The geophone used in our case was a L-4C 1.0 Hz seismometer from Mark Products via Sercel [70]. The specifications of this geophone are listed in Figure 6.4. According to the basic principles provided in chapter 3 for the transfer function of the geophone, the amplitude of signals close to, and above the resonant frequency can be assumed to be proportional to the particle velocity. The factor which correlates the signal amplitude and particle velocity is the sensitivity constant. However, it is worth noting that the sensitivity constant, S_G is a function of the instrument's parameters. In fact, an effective sensitivity constant has been defined in the product literature as the constant to obtain an output velocity. In short, Bowden [71] found a simple formula to obtain the effective sensitivity constant based on the internal coil induction resistance R_c, the shunt resistance R_s and the design

transduction G. Knowing the damping constant as well as other parameters mentioned above, the relationship between the output voltage and original ground velocity at $\omega > \omega_0$ is as follows:

$$\frac{V_{out}}{\dot{X}} = \frac{R_s}{R_s + R_c} G \quad (64)$$

Where V_{out} is the output voltage, and $\dot{X}$ is $\frac{dx}{dt}$ or the velocity. The unit of G is V/m.s^{-1} and hence the velocity can be obtained in m/s. The parameters used in our analysis are indicated in Figure 6.4 by the red dashed box. The coil resistance R_c of 5500 Ω, shunt resistance R_s for damping of 0.7 is 8905 Ω and the transduction G is 7.02 V/in.s^{-1} or 276.37 V/m.s^{-1}.

L-4C 1.0 Hz SEISMOMETER

Type	Moving dual coil, humbuch wound
Frequency	1.0 ± 0.05 Hz measured on 200 pound weight at 0.09 inches/second
Frequency change with tilt	Less than 0.05 Hz at 5° from vertical
Frequency change with excitation	Less than 0.05 Hz from 0 to 0.09 inches/second
Suspended mass	1000 grams
Standard coil resistances	500, 2000, 5500
Leakage to case	100 megohm minimum at 500 V
Transduction power	0.947 √ Rc
Open circuit damping	(bo) = 0.28 critical
Current damping	(bc) = 1.1 Rc / (Rs + Rc)
Coil inductance	Lc = 0.0011 Rc, Lc in henries
Case to coil motion	PP 0.250 inches
Electric analog of capacity	CC = 73,500 / Rc (microfarads)
Electric analog of inductance	Lm = 0.345Rc (henries)
Case height	5⅛ inches - 13 cm
Case diameter	3 inches - 7.6 cm
Total density	3.7 grams/cm³
Total weight	4¾ pounds - 2.15 kilograms
Operating temperature	Range : - 20° to 140°F or -29° to 60°C

COIL RESISTANCE, OHMS	500	2000	5500
Transduction, Volts/in/sec	2.12	4.23	7.02
Coil inductance, henries	0.55	2.20	6.05
Analog capacitance, microfarads	147	36.8	13.4
Analog inductance, henries	173	690	1900
Shunt for 0.70 damping, ohm	810	3238	8905

Figure 6.4. Specifications of the L-4C 1.0 Hz geophone [70]

Furthermore, using the frequency of each data point it is possible to extract the actual displacement of each particle using the conversion $\dot{X} = \omega X$.

6.2.2. Ground deformation and stiffness

Using the parameters mentioned in Eq. 64 we can assure that the output of the geophone signal has units of m/s. Using the most reliable filtering option which is removing all the signals with frequencies above 2Hz, we can obtain the area underneath the peak region in individual seismic traces. The area in this case has the unit of meters which is an estimation of the ground deformation. Figure 6.5 shows the deformation of the ground against time. It is worth noting that the time values corresponding to each deformation point is the middle point of the range used for calculation of the area.

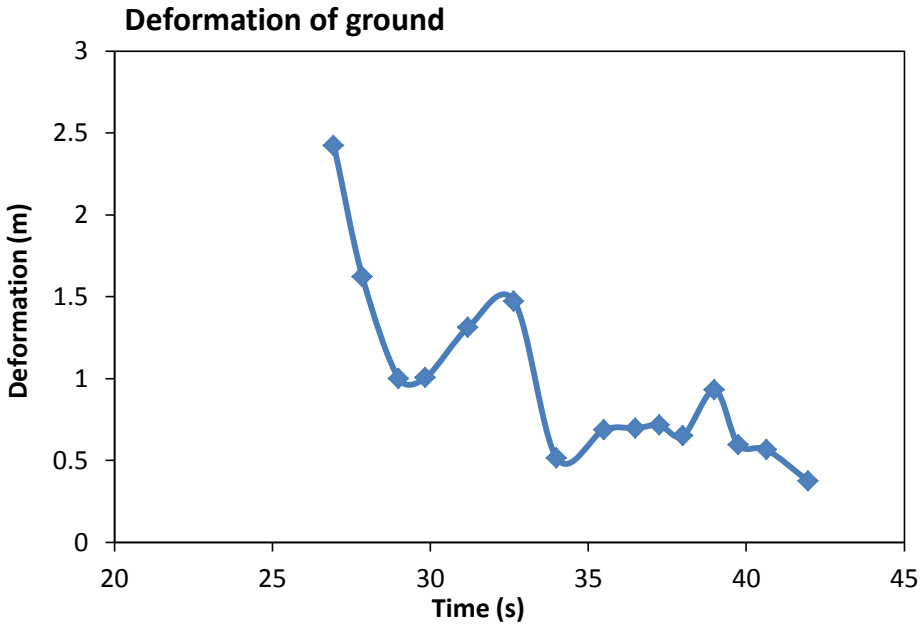

Figure 6.5. Deformation of the ground based on area under the seismic peak

As can be seen in this plot, the deformation values are in the range of 0.5-2.5 meter. One expects that the deformation of the ground to be somewhat less than these values. A deformation 2.5 m underneath the tire does not seem reasonable by the first look. However, a brief explanation for the calculation of the area under the peak could resolve this issue. The area underneath the peak in the seismic trace has been performed for a time range of 7-10 seconds surrounding the center point. The selection of the time interval is based on the width of the entire peak region. Considering the moving nature of the source, i.e. truck it is very difficult to deconvolute the effect of front tires from the rear tires when calculating the area. Hence, the time interval corresponds to the time duration in which both front and rear tires are passing over the

geophone. This might cause an overestimation of the ground deformation. The values of deformation are then used for calculating the ground load stiffness using the strut load over the deformation ratio. To minimize the effect of deformation overestimation, the sum of load from all struts should be used. Figure 6.6 demonstrates the sum of all strut loads overlaid on the deformation plot.

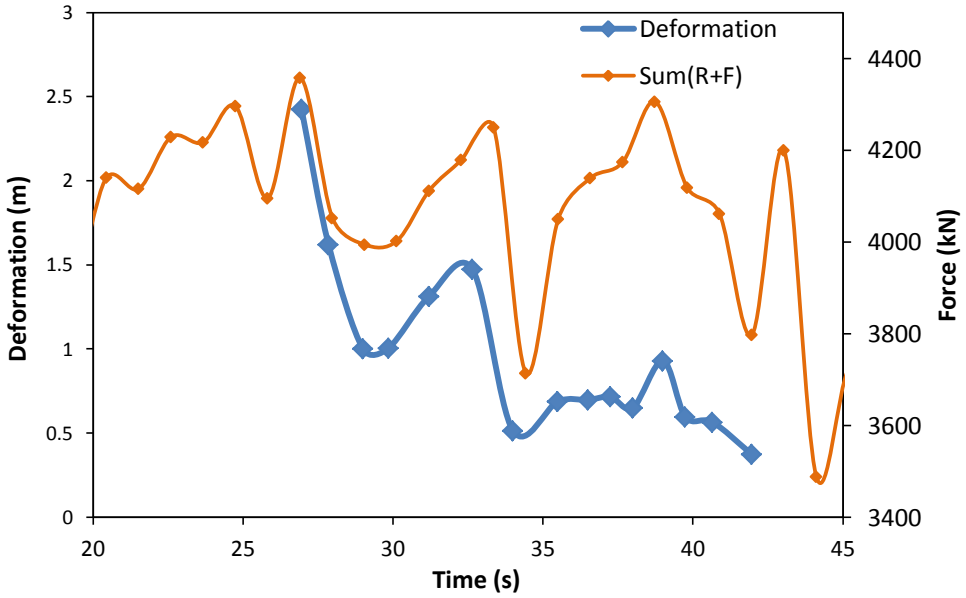

Figure 6.6. Sum of forces overlaid on deformation of ground

As the plot shows, the deformation follows the same trend as the force which is expected. The higher the load that is exerted on the ground, the larger the amount of deformation due to that force will be. The load stiffness now can be determined from the ratio of the force to the deformation. To be able to compare with the values obtained in the seismic analysis, the unit of the load stiffness has been set to MN/m for this case too. Figure 6.7 shows the comparison of the values obtained from the calculation of VIMS data to obtain the load stiffness with those obtained from the seismic analysis.

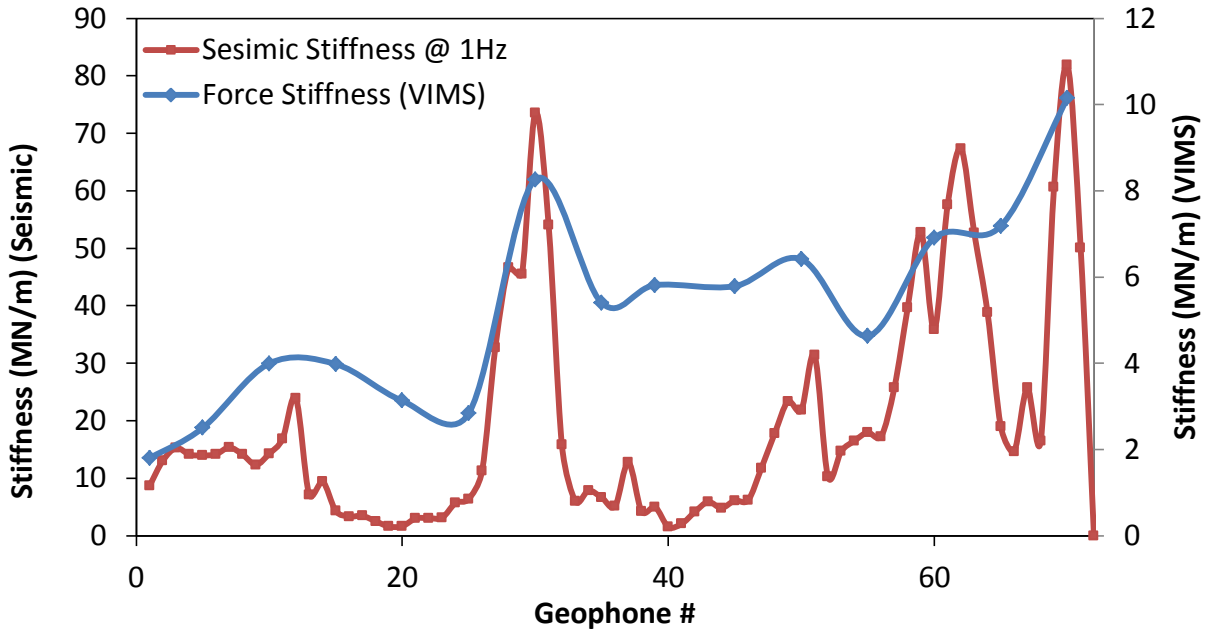

Figure 6.7. Comparison of load stiffness obtained from seismic and VIMS data

The most important feature of this plot is the fact that the trend of stiffness from both methods is very similar. VIMS data suggests that the areas close to geophone 30 as well as 50 and 60 have higher stiffness. The next point is the range of stiffness predicted from VIMS data analysis which differs slightly from that of seismic analysis. The most probable explanation could be the overestimation of the ground stiffness based on the calculations of area under the seismic peak. The values of load stiffness can be compared to some values in the literature. Sharif-Abadi et al. [17] reported that the pressure stiffness of the oil sand after prolonged load cycles plateaus to about 8 kPa/mm. Assuming a footprint area of 1.3 m^2, this value corresponds to the load stiffness of 10.4 MN/m. This is in the lower end of the range obtained from the seismic analysis for the load stiffness. On the other hand, the load stiffness of 10.4 MN/m is at the higher end of stiffness range calculated based on VIMS data. Overall, it seems that the two methods are both capable of predicting the trend of stiffness variation over the length of geophone array. The two methods were also able to provide acceptable numbers for the ground stiffness while seismic predicting higher values compared to VIMS data analysis.

Chapter 7

7. Conclusions

With an ever increasing demand for larger equipment to increase the productivity of mining operations, the concept of equipment-ground interactions has become an important research subject. Apart from the failure of different parts, the use of large mining equipment also has destructive effects on the ground they are travelling. The field of heavy vehicle-ground interaction has hence been divided into two major subjects of ground stability and equipment stability. It is, however, impossible to study the influence of one subject independent of the impact of the other. The use of heavy haul trucks and shovels significantly changes the properties of the ground in such a way that several regions of extremely soft material will be created on the top surface of ground. The presence of these regions in turn causes the sinking of tires of shovel pads much further than that in the case of fresh or untouched ground. This will eventually cause an increase in the fuel consumption due to the rolling resistance increase. Tire damage and shortening of life time are also some important effects of such ground softening. It is hence necessary to study the constant evolution of the ground properties while it is being affected by the moving vehicle passing over it.

Many studies have been dedicated to investigate the variation in properties of ground material under different pressure and temperature conditions. Most of these effort have been made through laboratory scale experiments to mimic the conditions of the real mine filed. The results of such experiments can help predict the behavior of the ground during the mining operating conditions. However, it is still advantageous to perform large scale experiments during the operation of heavy mining equipment. This would help researchers to confirm the results of laboratory scale measurements. It is the subject of this thesis to explore the possibility of extracting the properties of ground from data collected from a real mining operation. Among several methods of performing such experiments, two interesting methods that are the focus of current thesis are seismic analysis as well as on-board data collected from the haul truck.

Seismic methods are categorized into two major groups of active and passive seismic analysis. These methods utilize the concept of propagation of a series of seismic waves within the ground and tracking their behavior as they pass through the ground. The main component of such analysis is the seismic wave which is needed to be produced via a wave source. While the

source is of known energy and configuration in active seismic methods, it could be the moving truck generating seismic signals in the passive seismic methods. We used the latter methods, i.e. passive seismic analysis as we assume a haul truck passing by an array of seismometers known as geophones.

In the second series of data we utilized the data collected by the truck on-board systems known as VIMS which keeps the record of all suspensions as well as some other useful information. Tracking the pressures from all four series of suspension data during the same time of seismic data acquisition allows for obtaining some important information of ground material based on two different methods. The correlation between the two data series contains some challenges which are explained in the following paragraph.

The first challenge towards the analysis of seismic results is to identify the useful signals for the processing and obtaining the ground properties. This was done through exploring the seismic response from the ground in the frequency domain. Based on previous studies, it is known that the signals acquired during the motion of truck contain noises from several sources. These are including the noise signals from the internal working parts of the truck such as engine as well as some external parts such as tires. We also encountered some noise signals with the characteristics of similar arrival times. We relate these noise signals to the presence of a shovel and dozer working at a farther distance from the geophone array. In order to properly analyse the seismic results, it is necessary to remove the effects of all possible noise sources. In Chapter 2, we introduced the use of frequency-domain filtering methods. Among various filtering methods, two most commonly used methods are low-pass and band-pass filtering. A low-pass filter only allows for keeping signals below a certain frequency limit while it removes the signals with frequency higher than this limit. In band-pass filter, the signals within a certain range of frequency are being selected while signals with frequency outside this range are removed.

The results of applying several filtering options using the low-pass and band-pass methods were investigated in Chapter 2. For these investigations, the codes written within the framework of MATLAB software were utilized. Applying different filtering options helped identify and isolate the impact of individual noise source in the original seismic data. Upon application of several options we concluded that the most reliable portion of data which can be used for the seismic analysis belongs to the frequency zone of below 2 Hz. Hence, for the analysis of seismic

waves as well as correlation with the VIMS data, we used the signals with frequency below 2 Hz.

As a key component of seismic analysis, geophones consist of relatively complex structure which operates based on few simple physics principles. To be able to have sensible comparison between the seismic and VIMS data, it is necessary to know the working principles of a geophone. Based on our survey on the literature related to geophone research in Chapter 3, we concluded that it is possible to extract the velocity of ground particles in contact with the body of geophone. Through applying the appropriate parameters of geophone, we were able to obtain an estimation of particles velocity which can further be used to extract the deformation of ground.

The next important challenge for combining the VIMS and seismic results is to correlate the time frames corresponding to each method. It is very important to assure that the properties obtained using seismic analysis can properly be correlated with the data from VIMS. The difference in the resolution of data acquisition between the two methods causes a time drift. The resolution of VIMS data was 1 Hz or 1 data per second while seismic data were acquired with the rate 250 Hz. To identify the extent of such drift and to correct this drift is the subject of Chapter 4. In the first step, the location of truck was estimated based on the center of peak signal from the trace of individual geophones. To perform the correction, the first truck location point was assumed to have negligible drift relative to VIMS data and hence, was taken as a reference point. The next truck locations were then identified and evaluated based on the average truck speed from VIMS data. In the ideal case of zero-drift, the two data series must result in similar truck location. However, this was not the case and based on the difference between the time to travel a similar distance for two methods, a drift correction factor was obtained. Multiplying this factor by the VIMS time data resulted in minimizing the drift between the two time frames. To further confirm the validity of our drift correction, we utilized the concept of area under the seismic peak at its corresponding peak time. By comparing the area values with the load magnitudes from VIMS results we were able to show that the two parameters follow similar trend when the drift correction is applied.

In Chapter 5, the principles behind the use of seismic surface waves to predict the properties of ground including shear modulus and elastic modules as well as load stiffness. Based on the existing knowledge in the literature, a type of surface wave known as Rayleigh wave can be used to obtain the shear modulus. The velocity of Rayleigh waves can be measured based on certain

frequency or wavelength of the incoming seismic waves. Using our knowledge of noise source from Chapter 2 and applying the velocity measurements for different frequency ranges, we conclude that the low frequency range of <2 Hz provides the most reliable range for the shear modulus. Also, to be able to apply the calculations of the surface seismic method, the presence of a fixed source is required. Due to the moving nature of source in our case, we employed a method of dividing the seismic data into subdivisions of 1 second in duration and defined them as stationary envelopes of seismic data. This is the first trial for application of such method and similar works have not been done in the literature. The shear modulus values obtained with this method were in the range of 5-80 MPa. This is good agreement with the reported range of shear modulus for oil sand.

In Chapter 6, the results of seismic analysis and VIMS data processing were compared. To be able to extract meaningful values of the ground modulus based on VIMS data, we used the concept of the deformation under the trucks based the particle velocity obtained from the geophone output. By integrating the area underneath the peak region of seismic traces, we can have an estimate of the ground deformation. Since the deconvolution of seismic peaks due to the impact of rear and front tires was difficult, we estimated the overall deformation of ground caused by both front and rear tires. We then used the sum forces of rear and front struts and the deformation values to predict the load stiffness values. The stiffness values obtained from this method were in the range of 2-10 MN/m. The range of stiffness from seismic analysis was 2-70 MN/m. The reported pressure stiffness of the cycled oil sand materials results in the load stiffness of 10 MN/m. This suggests that the stiffness obtained from the two methods is somewhat in agreement with the reported values from the literature. The lower range for the VIMS results may be due to the overestimation of the ground deformation from the integrating the peak areas. However, both methods showed similar trends in the variation of ground stiffness along the geophone array. This suggests the possibility of application of these methods to any mine field to predict the properties of ground. This could also lead to developing preventive polices based on the variation of ground properties to minimize the damaging effect of ground on equipment.

Chapter 8

8. Future work

This thesis as presented in the previous chapters outlines the use of two important sets of data collected independently and compared to obtain representative values commensurate with the variation of oil sand moduli and stiffness as a moving and variable loading source in the guise of a haul truck passes over the zone of interest. As mentioned in chapter 7, the ground properties obtained from these two different data sources show promising results in terms of predicting a ground stiffness profile. However, there remain inconsistencies in terms of the magnitude of ground stiffness obtained by these 2 methods. Such differences can stem from the fact that the stiffness calculated based on equations of wave motion in solids contain factors such as contact surface area and intrinsic ground properties including density and Poisson's ratio. The deformation of ground due to the truck motion, which imparts a variable loading state, is also an important question which should be considered in these calculations, which requires further investigation. The following paragraphs summarize some ideas that could the subject of future studies.

An important solution to better identify a ground stiffness profile is to improve field testing methods. For instance, to collect data only based on the use of accelerometers to replace the on-board VIMS suspension data source, where such instrumentation would be located at the suspension positions, and recorded at the same data acquisition speed, would potentially eliminate many challenges related to time scale drift between the two data sources, as prospectively carried through to the moduli, stiffness and later running surface deformation estimates.

Confirmation of moduli and stiffness values should be clarified through conventional in-field more conventional geotechnical test data such as that established through plate loading tests and the direct vane shear test, commonly used in the field. Additional density data through Troxler nuclear densometer tests would also be most useful. All such geotechnical data would then provide a good link between the earlier laboratory based geotechnical work of SharifAbadi [13], which was referenced in this thesis.

One additional testing configuration that might eliminate a large degree of the noise filtration required would be to replace the moving truck by a moving seismic vibrator in "snapshot" steps

through the field. In this case, the vibrator would generate waves of known frequency and ground stiffness can be evaluated at each frequency.

To better identify the nature of noises, it may also be helpful to consider placing the truck in the middle of a geophone array and leave it running from low to high idle engine states. In this case, the frequency response of geophones would be a demonstration of engine and pump noise response. In conducting such a test set up, it would be necessary to ensure that the test area which is at far distance from other noise sources, such as dozer or shovel activity as was seen in the data sets used here. Investigating the possibility of using a source with a single wheel instead four sets of wheels could also be the subject of separate research study, but would require a unique test device to be conceived. In that case, the challenges regarding the use of rear and/or front tire pressures might be eliminated.

Improving the methodology of calculating the wave velocity could also be a subject of further study. Such work could be extended to investigate the effect of using various time frames when calculating the ground moduli, stiffness and deformation. Use of the full waveforms to carry out dispersion analyses could provide more detailed information on the shear wave structure of the near surface materials.

As mentioned in chapter 6, an important part of the ground stiffness calculation is to identify the density of ground. Hence, it is suggested to design and perform tests to incorporate the density of ground and use the results as input values for the calculation of ground stiffness. The extent of ground deformation logically has to be a function of ground density.

References

1. Chadwick, J., *Picking the best truck options.* International Mining, 2010(June): p. 10.
2. Knights, P. and A. Boerner, *Statistical correlation of off-highway tire failures with openpit haulage routes.* Mining Engineering, 2001. **53**(8): p. 51-56.
3. Anzabi, R.V., D. Nobes, and M. Lipsett. *Haul truck tire dynamics due to tire condition*. in *Journal of Physics: Conference Series*. 2012. IOP Publishing.
4. Zhou, J., *Investigation into the improvement of tire management practices*, 2007, University of British Columbia.
5. Bolster, M. and T. Joseph. *Tire-Rim Interactions for Ultra Class Trucks in The Mining Industry*. in *The 19th International Mining Congress and Fair of Turkey*. 2005.
6. Bolster, M.J.A., *Tire rim interactions for ultra-class truck performance*, 2007, University of Alberta.
7. Joseph, T. *Large mobile mining equipment operating on soft ground*. in *Proceedings of the 18th International Mining Congress and Exhibition of Turkey–IMCET*. 2003.
8. Whalen, D. and K. Obaia, *Effect of Oil Sand Mining Operations on Haul Truck Dump Body Design.* Operational Challenges in the Canadian Oil Sands, 2003.
9. R.F. Santos and T.G. Joseph. *A rapid dampening suspension for ultra-class haulers*. in *The 19th International Mining Congress and Fair of Turkey*. 2005. Izmir, Turkey.
10. Berezan, J., T. Joseph, and V. del Valle, *Monitoring whole-body vibration effects on ultra-class haulers.* CIM Bulletin, 2004. **97**(1082): p. 1-4.
11. Energy, C.f. *http://www.centreforenergy.com/AboutEnergy/*.
12. Joseph, T.G., *OsEIP: The oil sand equipment interactions program.* CIM Bulletin, 2002. **95**(1064): p. 4.
13. Sharif-Abadi, A., *Cyclic performance of soft ground*, 2006, PhD thesis, University of Alberta.
14. Joseph, T.G., A. Sharif-Abadi, and N. Shi. *A broken material approach to modeling oil sand under dynamic load*. in *Calgary, CAMI Conference*. 2003.
15. Plewes, H.D., *Undrained Strength of Athabasca Oil Sand*. 1987: University of Alberta.
16. Agar, J.D., *Geotechnical behaviour of oil sands at elevated temperatures and pressures*, 2009, University of alberta.
17. Sharif-abadi, A.D. and T.G. Joseph, *An oil sand pseudo-elastic model for determining ground deformation under large mobile mining equipment.* Geotechnical and Geological Engineering, 2010. **28**(4): p. 471-481.
18. Krick, G., *Behaviour of tyres driven in soft ground with side slip.* Journal of Terramechanics, 1973. **9**(4): p. 9-30.
19. Wong, J.-Y., *Behaviour of soil beneath rigid wheels.* Journal of Agricultural Engineering Research, 1967. **12**(4): p. 257-269.
20. Wong, J., *On the study of wheel-soil interaction.* Journal of Terramechanics, 1984. **21**(2): p. 117-131.
21. Wong, J., *Some recent developments in vehicle—terrain interaction studies.* Journal of terramechanics, 1991. **28**(4): p. 269-288.
22. Thompson, R., et al., *Development of real-time mine road maintenance management system using haul truck and road vibration signature analysis.* Transportation Research Record: Journal of the Transportation Research Board, 2003. **1819**(1): p. 305-312.

23. Brothen, C. and T. Lee, *An ounce of prevention: The practical implementation of a wireless tire pressure monitoring system for mine sites.* CIM Magazine, 2008(February).
24. Miege, A.J.P. and A.A. POPOV, *Truck tyre rolling resistance under dynamic vertical load*, 2004, University of Nottingham, School of Mechanical, Materials, Manufacturing Engineering and Management, Nottingham.
25. Moser, R. and J. Lightner, *Using three-dimensional digital imaging correlation techniques to validate tire finite-element model.* Experimental Techniques, 2007. **31**(4): p. 29-36.
26. Kotchon, A., D. Nobes, and M. Lipsett. *Optical strain measurement for fault detection in haul-truck tires*. in *Journal of Physics: Conference Series*. 2012. IOP Publishing.
27. Zhou, J., et al., *Effect of off-the-road tyre rotation practices on tyre life: a case study.* Mining Technology, 2008. **117**(3): p. 101-110.
28. Zhou, J., et al., *Evaluation of the effect of off-the-road tire air pressure setting on tire performance.* International Journal of Mining, Reclamation and Environment, 2008. **22**(3): p. 237-244.
29. Komandi, G., *An evaluation of the concept of rolling resistance.* Journal of terramechanics, 1999. **36**(3): p. 159-166.
30. Anand, A., *Scaled Test Estimation of Rolling Resistance*, 2012, University of Alberta.
31. Cole, D.J., *Fundamental issues in suspension design for heavy road vehicles.* Vehicle System Dynamics, 2001. **35**(4-5): p. 319-360.
32. Cole, D. and D. Cebon, *Truck suspension design to minimize road damage.* Proceedings of the Institution of Mechanical Engineers, Part D: Journal of Automobile Engineering, 1996. **210**(2): p. 95-107.
33. Eslaminasab, N., *Development of a semi-active intelligent suspension system for heavy vehicles*, 2008, University of Waterloo.
34. Poh, K., et al., *Steel membrane floors for bodies of large rear-dump mining trucks.* Finite elements in analysis and design, 1999. **32**(3): p. 141-161.
35. Shearer, P.M., *Introduction to seismology*. 2009: Cambridge University Press.
36. Timoshenko, S. and J. Goodier, *Theory of elasticity, 1951.* New York. **412**.
37. Vallina, A.U., *Principles of seismology*. 1999: Cambridge University Press.
38. Dobrin, M.B. and C.H. Savit, *Introduction to geophysical prospecting*. Vol. 4. 1960: McGraw-Hill New York.
39. Chapman, C., *Fundamentals of seismic wave propagation*. 2004: Cambridge University Press.
40. Rayleigh, L., *On Waves Propagated along the Plane Surface of an Elastic Solid.* Proceedings of the London Mathematical Society, 1885. **s1-17**(1): p. 4-11.
41. Luna, R. and H. Jadi. *Determination of dynamic soil properties using geophysical methods*. in *Proceedings of the First International Conference on the Application of Geophysical and NDT Methodologies to Transportation Facilities and Infrastructure—Geophysics*. 2000.
42. Tokimatsu, K., et al., *Vs determination from steady state Rayleigh wave method.* Soils and Foundations, 1991. **31**(2): p. 153-163.
43. Nowinski, J., *On the nonlocal aspects of the propagation of Love waves.* International Journal of Engineering Science, 1984. **22**(4): p. 383-392.
44. Love, A.E.H., *Some Problems of Geodynamics: Being an Essay to which the Adams Prize in the University of Cambridge was Adjudged in 1911*. 1967: CUP Archive.

45. Sharifabadi, A., T. Joseph, and D. Schmitt, *Active and Passive Seismic as an Indicator of Large Equipment Interactions with the Oil Sand.* Geotechnical and Geological Engineering, 2010. **28**(6): p. 727-743.
46. Group, S.A.a.I. *SeismicLab*. Available from: http://seismic-lab.physics.ualberta.ca/.
47. Caterpillar. *Off-highway mining trucks*. Available from: http://www.cat.com/en_US/products/new/equipment/off-highway-trucks/mining-trucks.html.
48. Joseph, T.G. and M. Welz. *Mechanical action and geophysical reaction: equipment—oil sand interactions*. in *Calgary, CIM Conference*. 2003.
49. MathWorks. *Signal Processing Toolbox*. Available from: http://www.mathworks.com/.
50. Cambois, G., *Instrumentation or how many sows' ears does it take to make a silk purse?* The Leading Edge, 2002. **21**(9): p. 816-818.
51. Havskov, J. and G. Alguacil, *Instrumentation in earthquake seismology*. Vol. 22. 2010: Springer.
52. Barzilai, A., *Improving a Geophone to Produce an Affordable Broadband Seisometer.* Mechanical Engineering, Stanford University January, 2000. **25**.
53. Bêath, M., *Introduction to seismology*. 1979: Birkhauser.
54. Bernstein, J., *An overview of MEMS inertial sensing technology.* 2003.
55. Hons, M.S. *Seismic sensing: Comparison of geophones and accelerometers using laboratory and field data*. in *Masters Abstracts International*. 2008.
56. Brincker, R., et al. *Improving the classical geophone sensor element by digital correction*. in *Proc. of the International Modal Analysis Conference*. 2005.
57. Asten, M.W., *Theory and practice of geophone calibration in situ using a modified step method.* Geoscience Electronics, IEEE Transactions on, 1977. **15**(4): p. 208-214.
58. Lines, L. and T. Ulrych, *The Old and the New in Seismic Deconvolution and Wavelet ESTIMATION*.* Geophysical Prospecting, 1977. **25**(3): p. 512-540.
59. Wielandt, E., *Seismic sensors and their calibration.* New Manual of Seismological Observatory Practices, 2002: p. 1-46.
60. Caterpillar. *CAT Vital Information Management System - VIMS*. Available from: https://www.cashmanequipment.com/VIMS.htm.
61. Hope, V. and C. Clayton, *The use of surface waves in the determination of ground stiffness profiles.* Proceedings of the ICE-Geotechnical Engineering, 1996. **119**(2): p. 84-95.
62. Gazetas, G., *Vibrational characteristics of soil deposits with variable wave velocity.* International journal for numerical and analytical methods in geomechanics, 1982. **6**(1): p. 1-20.
63. Matthews, M.C., V.S. Hope, and C.R.I. Clayton. *The use of surface waves in the determination of ground stiffness profiles*. in *Proceeding of the institution of civil engineering*. 1996.
64. Matthews, M., C. Clayton, and Y. Own, *The use of field geophysical techniques to determine geotechnical stiffness parameters.* Proceedings of the ICE-Geotechnical Engineering, 2000. **143**(1): p. 31-42.
65. Stokoe, K.H. and S. Nazarian. *Use of Rayleigh waves in liquefaction studies*. in *Measurement and use of shear wave velocity for evaluating dynamic soil properties*. 1985. ASCE.

66. Haegeman, W. and W. Van Impe, *Characterization of disposal sites from surface wave measurements.* Journal of Environmental and Engineering Geophysics, 1999. **4**(1): p. 27-33.
67. Ganji, V., N. Gucunski, and S. Nazarian, *Automated inversion procedure for spectral analysis of surface waves.* Journal of geotechnical and geoenvironmental engineering, 1998. **124**(8): p. 757-770.
68. Moxhay, A., R. Tinsley, and J. Sutton, *Monitoring of soil stiffness during ground improvement using seismic surface waves.* Ground engineering, 2001. **34**(1): p. 34-38.
69. Abbiss, C., *Shear wave measurements of the elasticity of the ground.* Geotechnique, 1981. **31**(1): p. 91-104.
70. Sercel. *Mark Products*. Available from: http://www.sercel.com/products/seismometers.aspx.
71. Bowden, G.B., *Calibration of geophone microseismic sensors*, 2003.

1. Chadwick, J., *Picking the best truck options.* International Mining, 2010(June): p. 10.
2. Knights, P. and A. Boerner, *Statistical correlation of off-highway tire failures with openpit haulage routes.* Mining Engineering, 2001. **53**(8): p. 51-56.
3. Anzabi, R.V., D. Nobes, and M. Lipsett. *Haul truck tire dynamics due to tire condition*. in *Journal of Physics: Conference Series*. 2012. IOP Publishing.
4. Zhou, J., *Investigation into the improvement of tire management practices*, 2007, University of British Columbia.
5. Bolster, M. and T. Joseph. *Tire-Rim Interactions for Ultra Class Trucks in The Mining Industry*. in *The 19th International Mining Congress and Fair of Turkey*. 2005.
6. Bolster, M.J.A., *Tire rim interactions for ultra-class truck performance*, 2007, University of Alberta.
7. Joseph, T. *Large mobile mining equipment operating on soft ground*. in *Proceedings of the 18th International Mining Congress and Exhibition of Turkey–IMCET*. 2003.
8. Whalen, D. and K. Obaia, *Effect of Oil Sand Mining Operations on Haul Truck Dump Body Design.* Operational Challenges in the Canadian Oil Sands, 2003.
9. R.F. Santos and T.G. Joseph. *A rapid dampening suspension for ultra-class haulers*. in *The 19th International Mining Congress and Fair of Turkey*. 2005. Izmir, Turkey.
10. Berezan, J., T. Joseph, and V. del Valle, *Monitoring whole-body vibration effects on ultra-class haulers.* CIM Bulletin, 2004. **97**(1082): p. 1-4.
11. Energy, C.f. *http://www.centreforenergy.com/AboutEnergy/*.
12. Joseph, T.G., *OsEIP: The oil sand equipment interactions program.* CIM Bulletin, 2002. **95**(1064): p. 4.
13. Sharif-Abadi, A., *Cyclic performance of soft ground*, 2006, PhD thesis, University of Alberta.
14. Joseph, T.G., A. Sharif-Abadi, and N. Shi. *A broken material approach to modeling oil sand under dynamic load*. in *Calgary, CAMI Conference*. 2003.
15. Plewes, H.D., *Undrained Strength of Athabasca Oil Sand*. 1987: University of Alberta.
16. Agar, J.D., *Geotechnical behaviour of oil sands at elevated temperatures and pressures*, 2009, University of alberta.
17. Sharif-abadi, A.D. and T.G. Joseph, *An oil sand pseudo-elastic model for determining ground deformation under large mobile mining equipment.* Geotechnical and Geological Engineering, 2010. **28**(4): p. 471-481.

18. Krick, G., *Behaviour of tyres driven in soft ground with side slip.* Journal of Terramechanics, 1973. **9**(4): p. 9-30.
19. Wong, J.-Y., *Behaviour of soil beneath rigid wheels.* Journal of Agricultural Engineering Research, 1967. **12**(4): p. 257-269.
20. Wong, J., *On the study of wheel-soil interaction.* Journal of Terramechanics, 1984. **21**(2): p. 117-131.
21. Wong, J., *Some recent developments in vehicle—terrain interaction studies.* Journal of terramechanics, 1991. **28**(4): p. 269-288.
22. Thompson, R., et al., *Development of real-time mine road maintenance management system using haul truck and road vibration signature analysis.* Transportation Research Record: Journal of the Transportation Research Board, 2003. **1819**(1): p. 305-312.
23. Brothen, C. and T. Lee, *An ounce of prevention: The practical implementation of a wireless tire pressure monitoring system for mine sites.* CIM Magazine, 2008(February).
24. Miege, A.J.P. and A.A. POPOV, *Truck tyre rolling resistance under dynamic vertical load*, 2004, University of Nottingham, School of Mechanical, Materials, Manufacturing Engineering and Management, Nottingham.
25. Moser, R. and J. Lightner, *Using three-dimensional digital imaging correlation techniques to validate tire finite-element model.* Experimental Techniques, 2007. **31**(4): p. 29-36.
26. Kotchon, A., D. Nobes, and M. Lipsett. *Optical strain measurement for fault detection in haul-truck tires*. in *Journal of Physics: Conference Series*. 2012. IOP Publishing.
27. Zhou, J., et al., *Effect of off-the-road tyre rotation practices on tyre life: a case study.* Mining Technology, 2008. **117**(3): p. 101-110.
28. Zhou, J., et al., *Evaluation of the effect of off-the-road tire air pressure setting on tire performance.* International Journal of Mining, Reclamation and Environment, 2008. **22**(3): p. 237-244.
29. Komandi, G., *An evaluation of the concept of rolling resistance.* Journal of terramechanics, 1999. **36**(3): p. 159-166.
30. Anand, A., *Scaled Test Estimation of Rolling Resistance*, 2012, University of Alberta.
31. Cole, D.J., *Fundamental issues in suspension design for heavy road vehicles.* Vehicle System Dynamics, 2001. **35**(4-5): p. 319-360.
32. Cole, D. and D. Cebon, *Truck suspension design to minimize road damage.* Proceedings of the Institution of Mechanical Engineers, Part D: Journal of Automobile Engineering, 1996. **210**(2): p. 95-107.
33. Eslaminasab, N., *Development of a semi-active intelligent suspension system for heavy vehicles*, 2008, University of Waterloo.
34. Poh, K., et al., *Steel membrane floors for bodies of large rear-dump mining trucks.* Finite elements in analysis and design, 1999. **32**(3): p. 141-161.
35. Shearer, P.M., *Introduction to seismology*. 2009: Cambridge University Press.
36. Timoshenko, S. and J. Goodier, *Theory of elasticity, 1951.* New York. **412**.
37. Vallina, A.U., *Principles of seismology*. 1999: Cambridge University Press.
38. Dobrin, M.B. and C.H. Savit, *Introduction to geophysical prospecting*. Vol. 4. 1960: McGraw-Hill New York.
39. Chapman, C., *Fundamentals of seismic wave propagation*. 2004: Cambridge University Press.

40. Rayleigh, L., *On Waves Propagated along the Plane Surface of an Elastic Solid.* Proceedings of the London Mathematical Society, 1885. **s1-17**(1): p. 4-11.
41. Luna, R. and H. Jadi. *Determination of dynamic soil properties using geophysical methods*. in *Proceedings of the First International Conference on the Application of Geophysical and NDT Methodologies to Transportation Facilities and Infrastructure—Geophysics*. 2000.
42. Tokimatsu, K., et al., *Vs determination from steady state Rayleigh wave method.* Soils and Foundations, 1991. **31**(2): p. 153-163.
43. Nowinski, J., *On the nonlocal aspects of the propagation of Love waves.* International Journal of Engineering Science, 1984. **22**(4): p. 383-392.
44. Love, A.E.H., *Some Problems of Geodynamics: Being an Essay to which the Adams Prize in the University of Cambridge was Adjudged in 1911*. 1967: CUP Archive.
45. Sharifabadi, A., T. Joseph, and D. Schmitt, *Active and Passive Seismic as an Indicator of Large Equipment Interactions with the Oil Sand.* Geotechnical and Geological Engineering, 2010. **28**(6): p. 727-743.
46. Group, S.A.a.I. *SeismicLab*. Available from: http://seismic-lab.physics.ualberta.ca/.
47. Caterpillar. *Off-highway mining trucks*. Available from: http://www.cat.com/en_US/products/new/equipment/off-highway-trucks/mining-trucks.html.
48. Joseph, T.G. and M. Welz. *Mechanical action and geophysical reaction: equipment—oil sand interactions*. in *Calgary, CIM Conference*. 2003.
49. MathWorks. *Signal Processing Toolbox*. Available from: http://www.mathworks.com/.
50. Cambois, G., *Instrumentation or how many sows' ears does it take to make a silk purse?* The Leading Edge, 2002. **21**(9): p. 816-818.
51. Havskov, J. and G. Alguacil, *Instrumentation in earthquake seismology*. Vol. 22. 2010: Springer.
52. Barzilai, A., *Improving a Geophone to Produce an Affordable Broadband Seisometer.* Mechanical Engineering, Stanford University January, 2000. **25**.
53. Bêath, M., *Introduction to seismology*. 1979: Birkhauser.
54. Bernstein, J., *An overview of MEMS inertial sensing technology.* 2003.
55. Hons, M.S. *Seismic sensing: Comparison of geophones and accelerometers using laboratory and field data*. in *Masters Abstracts International*. 2008.
56. Brincker, R., et al. *Improving the classical geophone sensor element by digital correction*. in *Proc. of the International Modal Analysis Conference*. 2005.
57. Asten, M.W., *Theory and practice of geophone calibration in situ using a modified step method.* Geoscience Electronics, IEEE Transactions on, 1977. **15**(4): p. 208-214.
58. Lines, L. and T. Ulrych, *The Old and the New in Seismic Deconvolution and Wavelet ESTIMATION*.* Geophysical Prospecting, 1977. **25**(3): p. 512-540.
59. Wielandt, E., *Seismic sensors and their calibration.* New Manual of Seismological Observatory Practices, 2002: p. 1-46.
60. Caterpillar. *CAT Vital Information Management System - VIMS*. Available from: https://www.cashmanequipment.com/VIMS.htm.
61. Hope, V. and C. Clayton, *The use of surface waves in the determination of ground stiffness profiles.* Proceedings of the ICE-Geotechnical Engineering, 1996. **119**(2): p. 84-95.

62. Gazetas, G., *Vibrational characteristics of soil deposits with variable wave velocity.* International journal for numerical and analytical methods in geomechanics, 1982. **6**(1): p. 1-20.
63. Matthews, M.C., V.S. Hope, and C.R.I. Clayton. *The use of surface waves in the determination of ground stiffness profiles*. in *Proceeding of the institution of civil engineering*. 1996.
64. Matthews, M., C. Clayton, and Y. Own, *The use of field geophysical techniques to determine geotechnical stiffness parameters.* Proceedings of the ICE-Geotechnical Engineering, 2000. **143**(1): p. 31-42.
65. Stokoe, K.H. and S. Nazarian. *Use of Rayleigh waves in liquefaction studies*. in *Measurement and use of shear wave velocity for evaluating dynamic soil properties*. 1985. ASCE.
66. Haegeman, W. and W. Van Impe, *Characterization of disposal sites from surface wave measurements.* Journal of Environmental and Engineering Geophysics, 1999. **4**(1): p. 27-33.
67. Ganji, V., N. Gucunski, and S. Nazarian, *Automated inversion procedure for spectral analysis of surface waves.* Journal of geotechnical and geoenvironmental engineering, 1998. **124**(8): p. 757-770.
68. Moxhay, A., R. Tinsley, and J. Sutton, *Monitoring of soil stiffness during ground improvement using seismic surface waves.* Ground engineering, 2001. **34**(1): p. 34-38.
69. Abbiss, C., *Shear wave measurements of the elasticity of the ground.* Geotechnique, 1981. **31**(1): p. 91-104.
70. Sercel. *Mark Products*. Available from: http://www.sercel.com/products/seismometers.aspx.
71. Bowden, G.B., *Calibration of geophone microseismic sensors*, 2003.